

Copyright
by
Allen Lee Raines
2007

The Dissertation Committee for Allen Lee Raines
certifies that this is the approved version of the following dissertation:

**Nano-Scale Large Area Gap Control for High
Throughput Electrically Induced Micro-Patterning**

Committee:

S. V. Sreenivasan, Supervisor

C. Grant Willson

Joseph Beaman

Raul Longoria

Li Shi

**Nano-Scale Large Area Gap Control for High
Throughput Electrically Induced Micro-Patterning**

by

Allen Lee Raines, B.S., M.S.

DISSERTATION

Presented to the Faculty of the Graduate School of

The University of Texas at Austin

in Partial Fulfillment

of the Requirements

for the Degree of

DOCTOR OF PHILOSOPHY

THE UNIVERSITY OF TEXAS AT AUSTIN

December 2007

Acknowledgments

I would like to thank those who have helped me complete this dissertation. My advisor, Dr. S.V. Sreenivasan, has been an immense help in this project, both in project definition, focus, technical issues, and with help in navigating the bureaucracy of the university. Dr. C. Grant Willson and the members of his research group have been a great help with the chemical aspects of the project. I would like to thank Michael Dickey in particular for his help and collaboration on all aspects of this thesis. The staff of the Microelectronics Research Center, particularly James Hitzfelder and William Fordyce, moved the proverbial mountains to install the air tables and other tools necessary for this project. Dr. Jin Choi of Molecular Imprints was very helpful with design advice and with access to tools at Molecular Imprints. Many thanks go to PCB Piezotronics, Inc. for the long term loan of three force sensors.

I would like to thank the Mechanical Engineering Department for financial support through teaching assistantships. Thanks also go to the College of Engineering Thrust Fellowship program for financial support. Also, thanks go to DARPA for financial support through DARPA Advanced Lithography Grant No. N66001-01-1-8964.

Nano-Scale Large Area Gap Control for High Throughput Electrically Induced Micro-Patterning

Publication No. _____

Allen Lee Raines, Ph.D.

The University of Texas at Austin, 2007

Supervisor: S. V. Sreenivasan

Micro- and nano-scale patterning is essential to the fabrication of various kinds of devices including electronic circuits, optical devices, optoelectronic devices, thin film heads for magnetic storage, displays, etc. There are several current and emerging applications that specifically require regular arrays of repeating patterns such as gratings, posts, and holes. At the nano-scale, for replication using lithography techniques such as optical lithography and imprint lithography, the cost of making the master can be a significant portion of the fabrication cost, particularly if small batches of customized parts are required.

High resolution patterning using electric fields allows the creation of micro- and nano-scale structures using low resolution masters. Most of the literature to date has focused on using high glass transition temperature polymers that need to be heated to induce the patterning process. While this

allows the ability to use a wide variety of materials, it leads to poor throughput as it can take several minutes to complete the patterning of one device region. The patterning speed can be increased by using photocurable, low viscosity monomers instead of high glass transition temperature polymers. Process control requires a tool that can control the parallelism of the gap between a conductive wafer and template to the nanometer level over large areas. The tool must have high resolution orientation and position control and high apparent stiffness to prevent the electric field from pulling the template and wafer together.

In this research, high stiffness mechanism designs were investigated first. Such designs proved impractical, with travel, stiffness, and maximum side load requirements difficult or extremely expensive to meet. Therefore, a novel precision machine concept was explored. A parallel mechanism that is simultaneously actuated by piezo actuators and by voice coils was studied. Feedforward compensation of the applied electric force using voice coils was used to reduce the need for a stiff mechanism. The result was the Hybrid Active Gap Tool (HAGT), a 3-RPS parallel mechanism which has the ability to significantly enhance the quality of electrically induced patterning.

Performance of the Hybrid Active Gap Tool was validated using a set of gap control experiments. The new design and control system resulted in very high precision orientation alignment needed for gap control. Without voice coil compensation, the tool has a stiffness of less than $3\text{N}/\mu\text{m}$. With voice coil compensation, the apparent stiffness of the tool varies from a min-

imum of $30\text{N}/\mu\text{m}$ up to nearly infinite stiffness and into negative stiffness if overcompensation is intentionally used. Voice coil compensation allows the tool to meet the stringent performance requirements of the patterning process without the need for a high stiffness mechanism. Gaps as small as 400nm were maintained with the electric field applied and the gap changed by less than 5nm from the nominal 400nm during the process. Smaller gaps can be achieved with improvements in template mesa height calibration and better understanding of piezo actuated mechanism designs.

Table of Contents

Acknowledgments	iv
Abstract	v
List of Tables	xii
List of Figures	xiii
Chapter 1. Pattern Replication Processes	1
1.1 Photolithography	3
1.1.1 Optical Limits	4
1.1.2 Projection and Exposure	8
1.1.3 Extreme Ultraviolet	10
1.1.4 Conclusion	10
1.2 Electron Beam Lithography	11
1.3 Mechanical Pattern Replication Processes	14
1.3.1 Imprint Lithography	15
1.3.2 Lithographically Induced Self Assembly	18
1.3.2.1 LISA model	20
1.3.2.2 Capabilities, Limitations, and Possible Applications	23
Chapter 2. Parallel Manipulators	25
2.1 Parallel Manipulators	25
2.2 Three DOF 3-RPS Mechanism	28
2.2.1 Kinematics of the 3-RPS Mechanism	30
2.3 Conclusion	33
Chapter 3. Motivation and Hypothesis	34
3.1 Hypothesis	35

Chapter 4. Gap Sensing	36
4.1 Sensing Alternatives	37
4.1.1 Ellipsometry	37
4.1.2 Capacitive Sensing	38
4.1.3 Laser Interferometry	39
4.1.4 Reflectance Spectroscopy	40
4.2 Reflectance Spectroscopy	41
4.2.1 Single Film Interference	42
4.2.2 Two Film Interference	46
4.2.3 Summary	52
4.3 Frequency Analysis Methods	53
4.3.1 Frequency Estimation Challenges	53
4.3.2 Fourier Transform Methods	54
4.3.2.1 Resolution	55
4.3.3 Zero Crossing and Peak Detection Methods	59
4.3.3.1 Peak Detection Methods	60
4.3.3.2 Zero Crossing Methods	61
4.3.4 Auto Regressive Moving Average (ARMA) Methods . .	62
4.4 Method Verification, Uncertainty, and Operating Conditions .	65
4.4.1 Method Verification	66
4.4.1.1 Uncertainty	66
4.4.2 Operating conditions	69
4.4.3 Sample Rate	71
4.5 Conclusion	72
Chapter 5. Preliminary Results	73
5.1 Active Gap Tool	73
5.2 Nano-Align 3	77
5.3 Materials and Experimental results	78
5.3.1 Photocurable Acrylates	78
5.3.1.1 Experimental Results	78
5.3.2 New Polymer Formulation	80

5.3.2.1	Thiol-ene Results	80
5.4	Return to the Active Gap Tool	82
5.4.1	Electrical Force	84
5.4.2	Active Gap Tool Stiffness	91
5.5	Conclusion	91
Chapter 6.	Pillar Formation Machine Requirements	93
6.1	Physical Requirements	94
6.1.1	Wafer and Template	94
6.1.2	Gap Sensing	96
6.1.3	UV curing and video feed	96
6.2	Applied Load Derivation	97
6.3	Necessary Stiffness and Travel	100
6.3.1	Necessary Travel	100
6.3.2	Necessary Stiffness	101
6.3.3	Stiffness Alternative	101
Chapter 7.	Pillar Formation Tool Design	103
7.1	Stiff designs	103
7.1.1	Actuators	103
7.1.2	Kinematics and Stiffness	107
7.1.2.1	Template Side Mechanism	107
7.1.2.2	Wafer Side Mechanism	111
7.2	Force Compensation Designs	114
7.2.1	Return to the Active Gap Tool	116
7.2.1.1	Modifications to the Active Gap Tool	117
Chapter 8.	Control System	123
8.1	Motor Control Mode and System Overview	123
8.2	Quasi-Static Control	125
8.2.1	Gap Transform	125
8.2.2	Control Law	130
8.2.2.1	Control Results	131

8.2.3	Mesa Calibration	134
8.3	Voice Coil Compensation	139
8.3.1	Voice Coil Calibration	139
8.3.2	Feedforward Compensation	140
8.3.3	Sensitivity Test	145
8.4	Conclusion	145
Chapter 9.	System Performance Experiments	148
9.1	Experimental Methodology	148
9.2	Compensation Performance Experiments	153
9.2.1	Experiment Design	153
9.2.2	Experimental Results	157
9.2.2.1	Large Gap, High Voltage	157
9.2.2.2	Small Gap, Low Voltage	164
9.3	Conclusions	170
Chapter 10.	Conclusions and Recommendations	172
	Appendices	175
	Appendix A. Results of Gap Control Experiments	176
	Bibliography	207
	Vita	215

List of Tables

1.1	Production photolithography illumination sources and wavelengths	7
4.1	Wavelength range and maximum measurable gap with 512 interpolation samples	70
7.1	Dimensions and stiffnesses of flexures in proposed design . . .	109
A.1	ANOVA for force response of large gap experiment	177
A.2	ANOVA for force response of large gap experiment, cont. . .	178
A.3	ANOVA for force response of large gap experiment, cont. . . .	179
A.4	ANOVA for gap response of large gap experiment	184
A.5	ANOVA for gap response of large gap experiment, cont. . . .	185
A.6	ANOVA for gap response of large gap experiment, cont.	186
A.7	Raw data from large gap experiment	191
A.8	Raw data from large gap experiment, cont.	192
A.9	ANOVA for force response of small gap experiment	193
A.10	ANOVA for force response of small gap experiment, cont. . . .	194
A.11	ANOVA for gap response of small gap experiment	199
A.12	ANOVA for gap response of small gap experiment, cont. . . .	200
A.13	Raw data from small gap experiment	205
A.14	Raw data from small gap experiment, cont.	206

List of Figures

1.1	A generalized photolithography system	5
1.2	Concepts for immersion lithography	9
1.3	Schematic of an electron beam lithography system	12
1.4	Vector scanning and raster scanning	13
1.5	Imprint lithography	16
1.6	LISA schematic	18
1.7	Patterns formed using LISA	19
1.8	Pillars formed with LISA, showing regions of hexagonal order[20]	20
1.9	Parameters used in LISA model	21
2.1	Two stewart platform 6-DOF parallel manipulators.	27
2.2	The 3-RPS parallel manipulator	29
4.1	Reflected rays in one film interference	42
4.2	Reflected rays in two film interference	46
4.3	Fourier transform of simulated two film interference	50
4.4	Fourier transform of simulated two film interference divided by the film reference	51
4.5	Fourier transform of simulated two film interference divided by an unequal film reference	52
4.6	Unpadded Fourier transform of simulated 10 μm air gap . . .	56
4.7	Fourier transform of simulated 10 μm air gap, zero padded 64x	56
4.8	Unpadded Fourier transform of simulated 0.75 μm film and 9.25 μm air gap	57
4.9	Fourier transform of simulated 10 μm air gap, zero padded 64x	58
4.10	Comparison of polystyrene film measurements made with ellip- sometry and with reflectance spectroscopy with ARMA analysis	67
5.1	CAD image of the Active Gap Tool	75
5.2	Photograph of the Active Gap Tool	76

5.3	Flexure ring from the Active Gap Tool	76
5.4	Pillar residue from uncured silicone pillars	79
5.5	Pillars formed on Nano-Align, showing regions of order	81
5.6	Pillars formed on Nano-Align, showing bimodal pattern	82
5.7	Pillars formed on Nano-Align, showing regions of order	83
5.8	Pillars formed on Nano-Align, showing bimodal pattern	83
5.9	Cross section of pillar formed on Nano-Align	84
5.10	Side view of the Nano-Align setup	85
5.11	Top view of Nano-Align setup	86
5.12	Template with wire attached	87
5.13	Side view of template, showing mesa height and edge rounding	88
5.14	Template Face	88
5.15	Electrical force	90
5.16	Active Gap Tool Stiffness	92
6.1	Predicted electrical force	99
6.2	Stiffness required to allow 5% gap movement under maximum electric field	102
7.1	Mechanism leg consisting of piezo actuators and flexures . . .	110
7.2	Template side mechanisms	111
7.3	Air bearing wafer side mechanism	113
7.4	Wafer side mechanism	113
7.5	Pillar Formation Tool with voice coil compensation	116
7.6	New template holder	118
7.7	Modified Active Gap Tool	119
7.8	Hybrid Active Gap Tool, during assembly	120
7.9	Hybrid Active Gap Tool	121
8.1	Screenshot of the motor mode software	124
8.2	Screenshot of the piezo mode software	126
8.3	Template and wafer planes sensor and motor locations	127
8.4	Central gap and temperature drift over several hours.	133

8.5	Illustration of mesa calibration problem, with unflatness exaggerated	136
8.6	Profile of wafer on wafer chuck, measured with Zygo Interferometer	137
8.7	Profile of template chuck, measured with Zygo Interferometer	137
8.8	Profile of template on template chuck, measured with Zygo Interferometer	138
8.9	Voice coil calibration frame	140
8.10	Voice coil calibration results	141
8.11	Force compensation sensitivity test	146
8.12	Control System Flowchart	147
9.1	Experimental data set taken at a gap of 500nm with an applied voltage of 10volts	150
9.2	Experimental data set taken at a gap of 500nm with an applied voltage of 10 volts, including the total force applied to the template	152
9.3	Central gap with drift correction.	154
9.4	Parameter space for gap control experiments	155
9.5	Response surface from the large gap, high voltage experiment for gap change without voice coil compensation	159
9.6	Response surface from the large gap, high voltage experiment for gap change with voice coil compensation	161
9.7	Predicted Gap Change versus measured Gap Change for the large gap, high voltage experiment.	163
9.8	Applied force vs. gap change for the Hybrid Active Gap Tool .	165
9.9	Predicted Gap Change versus measured Gap Change for the small gap, low voltage experiment.	166
9.10	Gap Change for the small gap, low voltage experiment without voice coil compensation	168
9.11	Gap Change for the small gap, low voltage experiment with voice coil compensation	169
9.12	Applied force vs. gap change for the Hybrid Active Gap Tool .	171
A.1	Response surface for measured force without voice coil compensation, large gap experiment	180

A.2	Response surface for measured force with voice coil compensation, large gap experiment	181
A.3	Predicted versus actual values for force response, large gap experiment	182
A.4	Normalized residuals of force response, large gap experiment	183
A.5	Response surface for gap change without voice coil compensation, large gap experiment	187
A.6	Response surface for gap change with voice coil compensation, large gap experiment	188
A.7	Predicted response versus measured values for gap response, large gap experiment	189
A.8	Normalized residuals of gap response, large gap experiment	190
A.9	Response surface for measured force without voice coil compensation, small gap experiment	195
A.10	Response surface for measured force with voice coil compensation, small gap experiment	196
A.11	Predicted versus actual values for force response, small gap experiment	197
A.12	Normalized residuals of force response, small gap experiment	198
A.13	Response surface for gap change without voice coil compensation, small gap experiment	201
A.14	Response surface for gap change with voice coil compensation, small gap experiment	202
A.15	Predicted response versus measured values, gap response, small gap experiment	203
A.16	Normalized residuals of gap response, small gap experiment	204

Chapter 1

Pattern Replication Processes

Many products today are manufactured by forming sub micron sized patterns on a flat substrate. Microelectronics are the most visible, but there are other products that are formed by transferring patterns to a substrate. Photonics, microfluidics, MEMS, and biosensors are a few of the applications that require the formation of accurate submicron patterns. The formation of these patterns falls under the general heading of microlithography. Leading edge microelectronics is using sub-100nm photolithography today. However, these techniques are complicated to implement and expensive. Therefore, they are not used for other applications. If inexpensive sub-200nm lithography can be developed a variety of applications such as photonic crystals for LEDS, quantum dots for lasers, patterned magnetic media, etc. can become viable.

There are several types of systems currently used in microlithography manufacturing. The system in widest use for large scale manufacturing is photolithography. Electron beam lithography is used in mask manufacturing for photolithography and in research and development. Other types of lithography are in development for next generation lithography. These include extreme UV lithography, immersion lithography, imprint lithography, X-ray

lithography, and ion beam lithography [1].

Microelectronics device fabrication has primarily driven the progress in microlithography. A portion of this chapter will focus on developments related to microelectronics to provide a historical context. This will be followed by a discussion of mechanical pattern replication processes, which is the focus of this research.

Microelectronics are made by forming circuits on semiconductor wafers, most commonly silicon wafers. Transistors and capacitors are formed in the silicon and then connected to form circuits by metal interconnects. As circuit elements get smaller and cheaper, more circuit elements can be implemented per chip, which leads to faster computers and other electronics. This trend is described by Moore's Law, which predicts that the number of transistors per chip will double every 18 months [2], [3].

As the circuit elements shrink, the manufacturing processes must change to accommodate manufacture of the smaller elements. A typical processor will consist of a layer of transistors and capacitors connected by several layers of metal interconnects. The different layers are formed one at a time by transferring a pattern to the wafer. The wafer then has material either deposited, etched away, or diffused in with the transferred pattern controlling which areas are affected. The minimum transferred feature size and minimum pattern pitch controls the size of the circuit elements and ultimately the performance of the product.

A lithography system must perform several functions. It must include a pattern master, a medium on the substrate to receive the pattern, some way to transfer the pattern from the master to the substrate, and a method to align the different layers. The system must be clean and have low defect rates. It must have high throughput to lower average production costs. The system must also have good control of device critical dimensions.

1.1 Photolithography

Photolithography is the technology of choice for most high volume semiconductor manufacturing, display fabrication, thin film heads, and microelectromechanical systems. A photolithography process is commonly referred to by the smallest feature it can print, the critical dimension, and the tightest pitch it can resolve, typically described by the pattern half-pitch. Current manufacturing techniques are at the 65 nm half pitch. Shrinking to a smaller critical dimension requires the improvement of machines, processes, and materials.¹ Photolithography is the technology of choice described in the International Technological Roadmap for Semiconductors (ITRS) for the next few process half-pitches[1].

Figure 1.1 shows a schematic of a generalized photolithography system. A photolithography system contains an illumination source, illumination op-

¹The ITRS describes industry consensus about the requirements for each successively smaller process half pitch. Leading edge photolithography is now operating at a wavelength of $\lambda = 193$ nm, and can pattern structures at the 65 nm half pitch.

tics, a photomask, projection optics, a photoresist on the wafer, a stage to move the wafer, and a system to align successive layers. The general process flow is that the light shines through the photomask which contains the circuit pattern. The circuit image is then demagnified, typically 4x, and projected onto the photoresist. The light reacts with the photoresist, transferring the pattern from the mask onto the wafer. Only a small portion of the wafer is exposed at once. The wafer is then moved to the next circuit position and exposed. After the wafer is completely exposed, the photoresist is developed and the wafer is then ready for further processing.

Photolithography is a simple concept, but the high resolutions required by today's devices are close to the minimum size dictated by hard physical limits such as the diffraction limit. Successful high resolution lithography requires creative solutions to decrease the seemingly fixed physical limits.

1.1.1 Optical Limits

The smallest features that can be printed by an optical system are controlled by physical laws. Images are formed by diffraction and interference. The incident light diffracts off of the object, producing a pattern of diffraction maxima and minima. The diffraction pattern then passes through the lens system. The image is then reformed at the image plane by interference of the different diffraction maxima and minima. If there is only one maximum, there is no interference and therefore no image. The need for multiple diffraction maxima determines the resolution limit for an imaging system [4][5].

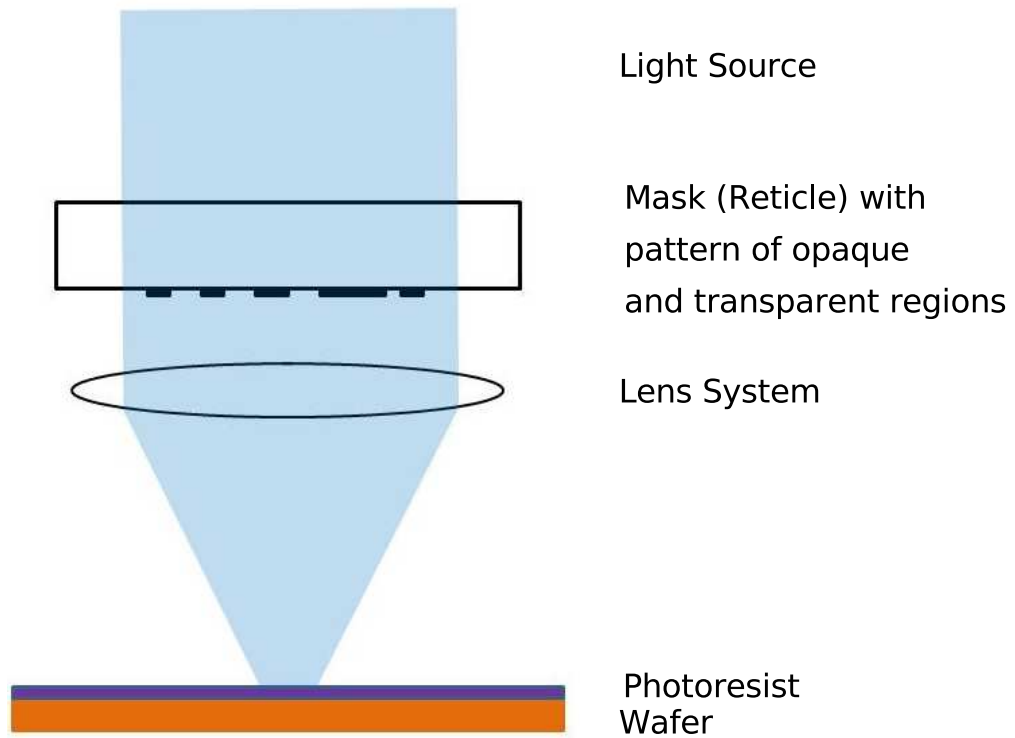


Figure 1.1: A generalized photolithography system

As feature sizes shrink, the incident light diffracts at higher and higher angles. At some angle, light will no longer pass through the lens. The maximum angle θ at which light will pass through the lens determines the lens half aperture $\sin \theta$. The resolution limit of the imaging system is reached when the two first order diffraction maxima barely pass through the lens. The image is formed by the zeroth and \pm first order diffraction maxima. In the photolithography literature, this is referred to as the three beam case even though the maxima are not, strictly speaking, beams. The factors that determine when the resolution limit W is reached are the wavelength of the incident light λ , the ambient index of refraction n , the half aperture $\sin \theta$, and a factor related to photomask design and processing conditions k_1 . These parameters are found in the Rayleigh equation, found in equation 1.1. The product $n \sin \theta$ is commonly called the numerical aperture of the lens system.

$$W = k_1 \frac{\lambda}{n \sin \theta} \quad (1.1)$$

The Rayleigh equation shows how to increase the resolution of an optical system. The wavelength λ can be decreased, the numerical aperture $n \sin \theta$ can be increased, or the process factor k_1 can be decreased. Each of these approaches has been traditionally employed to increase the imaging resolution of photolithography. Wavelengths have shrunk to 193nm and lens systems have been developed with numerical apertures exceeding 0.9. New mask designs and refined processes are decreasing k_1 .

Illumination Source	Wavelength
Mercury Vapor Lamp G-line	436nm
Mercury vapor lamp I-line	365nm
KrF excimer laser	248 nm
ArF excimer laser	193nm

Table 1.1: Production photolithography illumination sources and wavelengths

Another way to increase resolution is to use a two beam process. If the image is formed with only two beams, the angle between adjacent beams can be double what is possible in the three beam case. This adds a factor of $1/2$ to the Rayleigh equation and doubles the resolution possible. Two approaches to creating the two beam case are off axis illumination and phase shift masks. In off axis illumination, the incident light comes in at an angle, rotating the diffraction pattern so that one of the first order beams falls outside the lens and the resolution limit is determined by the zeroth order beam and the remaining first order beam. With phase shift masks, certain parts of the mask either have a different thickness or have a layer of phase shifting material added. [5][6] The extra material creates interference which eliminates the zeroth order beam and rotates the remaining beams to half the angle they would otherwise have formed. The resolution limit is then determined by the two first order beams.

The Rayleigh equation describes the theoretical resolution limit. Achieving an actual resolution close to the theoretical limit requires ideal conditions. The light source needs to be uniform and supply a single wavelength. The light sources currently in use are listed in table 1.1.

The KrF and ArF lasers are referred to as Deep Ultraviolet (DUV). The ArF laser is currently used in the most critical layers of cutting edge circuits. KrF, I-line, and G-line are used on the less critical layers and on lower resolution products.

The light from the illumination source then passes through the illumination optics. The illumination optics system takes the light supplied by the source and homogenizes it. An illumination pattern can be added to aid the pattern exposure. Then the light passes through the photomask.

As discussed earlier, the photomask contains the circuit pattern. The mask may contain phase shift elements in the image pattern. The circuit pattern may also contain optical correction elements to achieve the desired shape. Images with elements near the optical limit seldom reproduce the shape exactly. Corners are rounded off and lines are either too long, too short, or of the wrong thickness. The pattern on the mask is therefore manipulated so the image produced is the image desired. Examples of optical correction elements are line end anchors, changing the thickness of corners, and adding sub resolution assist features.[7][8][7][9]

1.1.2 Projection and Exposure

Once the light passes through the mask, it must be demagnified and projected on the wafer. The lens system must have high numerical aperture, low aberration, and transmit the exposure wavelength. The wafer must be moved precisely to produce a clear image and control layer to layer alignment.

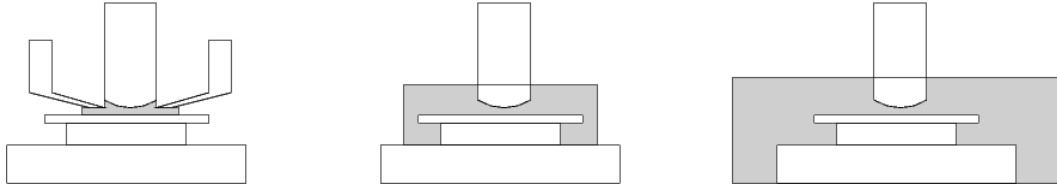


Figure 1.2: Concepts for immersion lithography. From the left, the concepts are the shower, bathtub, and swimming pool. The shower is currently the concept of choice

The light exposes the photoresist on the wafer, leaving the desired circuit pattern on the surface.

One resolution enhancement technique currently being developed is an old idea borrowed from optical microscopy. When a fluid with high index of refraction fills the gap between the object and the lens, the numerical aperture of the lens is increased[4][10]. This leads to increased resolution. This technique, referred to as immersion lithography, can either be used to increase resolution by increasing the angle of rays that reach the wafer surface or increase depth of focus by limiting the angle of rays that pass through the lens. Immersion increases resolution by allowing transmission of light that would have otherwise been totally internally reflected. Immersion lithography is believed to be the leading technology of choice for the 45nm process half pitch.

One question that needs to be answered in immersion lithography is how to supply the fluid. The three options are to supply the fluid to the area as it is needed and recover it from the area it is no longer needed, immerse the

wafer in fluid, and immerse the whole stage in fluid. These three concepts are referred to as the shower, the bathtub, and the swimming pool. The shower is currently the concept of choice. The swimming pool is considered infeasible because of the problem of controlling stage motion in the fluid. The main issue with the bathtub is unstable motion of the immersion fluid. The issue with the shower head is ensuring complete filling of the imaging area. Lithography tool manufacturers have made progress in developing the shower head concept and are planning to have it ready for production of the 45 nm half pitch. Beyond the 45nm half-pitch, there is considerable debate about how immersion can be used. One proposal is to use double patterning for the 32nm half-pitch. However, this will require alignment accuracies of about 2-3 nm between two patterned regions, which is considered a major challenge.

1.1.3 Extreme Ultraviolet

Extreme UV is one of the candidate technologies for use at the 30 nm node and beyond [1]. Extreme UV uses a 13nm light source and all reflective optics. A lot of challenges need to be met in all of the subsystems before Extreme UV is a viable solution.

1.1.4 Conclusion

Photolithography is the workhorse of the semiconductor industry today. Physical limits on resolution are being removed as the physics of the process are better understood. New light sources, resolution enhancement technologies,

optical techniques such as immersion lithography, and a lot of engineering ingenuity will press photolithography to the 45 nm process half pitch, and possibly to the 30 nm half pitch. Costs are also rising with resolution. Scanners can cost \$30 million and mask sets for one product can cost \$4 million. These costs are justified in large volume production, but might not be feasible for smaller production runs. Despite the rising costs, photolithography looks to be the lithography of choice for volume production for some years to come.

1.2 Electron Beam Lithography

Electron beam lithography is one of the highest resolution lithography solutions and is also correspondingly one of the slowest. E-beam is used for writing photomasks and making prototypes. Work is ongoing to make e-beam more suitable for volume production.

Electron beam lithography works by projecting a beam of electrons onto the substrate. The beam forming and projecting mechanism is much like that found in a scanning electron microscope. In fact, many early e-beam tools were converted microscopes. A schematic of an electron beam tool is shown in figure 1.3. In an e-beam tool, the substrate to be patterned is coated with an e-beam resist that will react when hit by the beam to form the image. The beam is turned on and off to make exposed and unexposed areas. The image is written serially, one spot at a time, instead of all at once. This gives e-beam lithography the flexibility of writing any desired pattern. This form of lithography is called direct write electron beam because the image is written

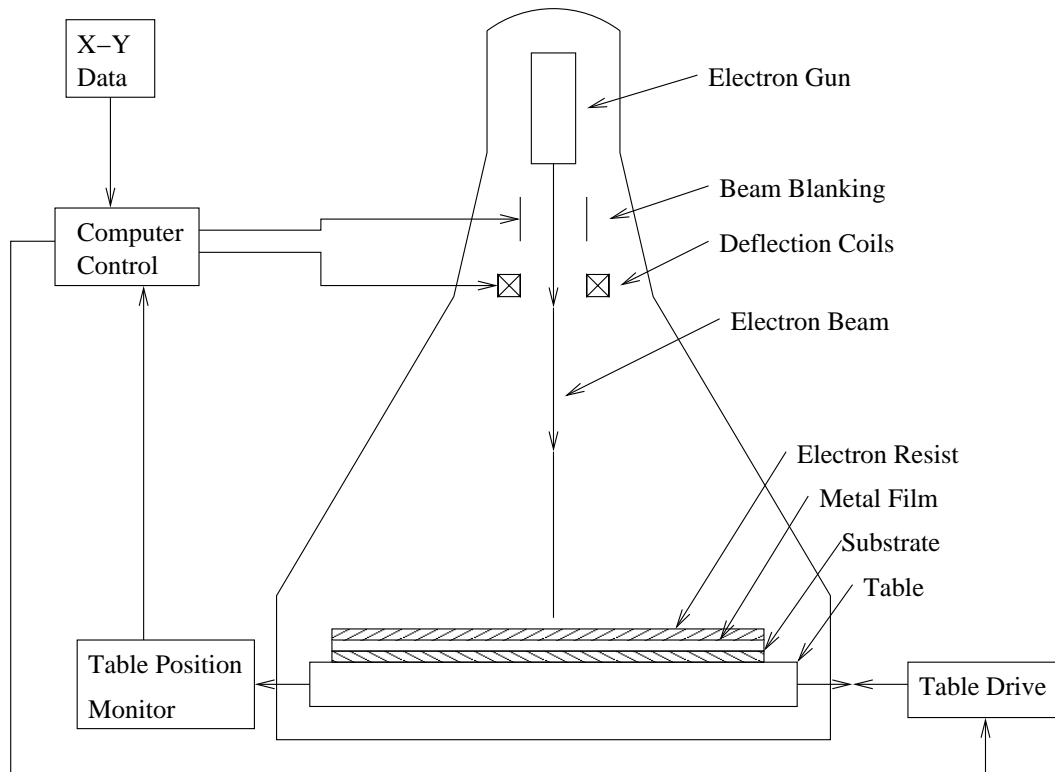


Figure 1.3: Schematic of an electron beam lithography system

directly from a data file. Writing directly from a data file makes direct write e-beam suitable for photomasks, prototypes, and for research and development projects.

There are several beam shapes in current use. The highest resolution beam is the Gaussian beam. A Gaussian beam can have a diameter of 5 nm. This high resolution makes writing a complete image very slow. Therefore, a type of beam called variable shaped beam is commonly used. The variable shaped beam is a square beam that can be sized as the designer desires. The

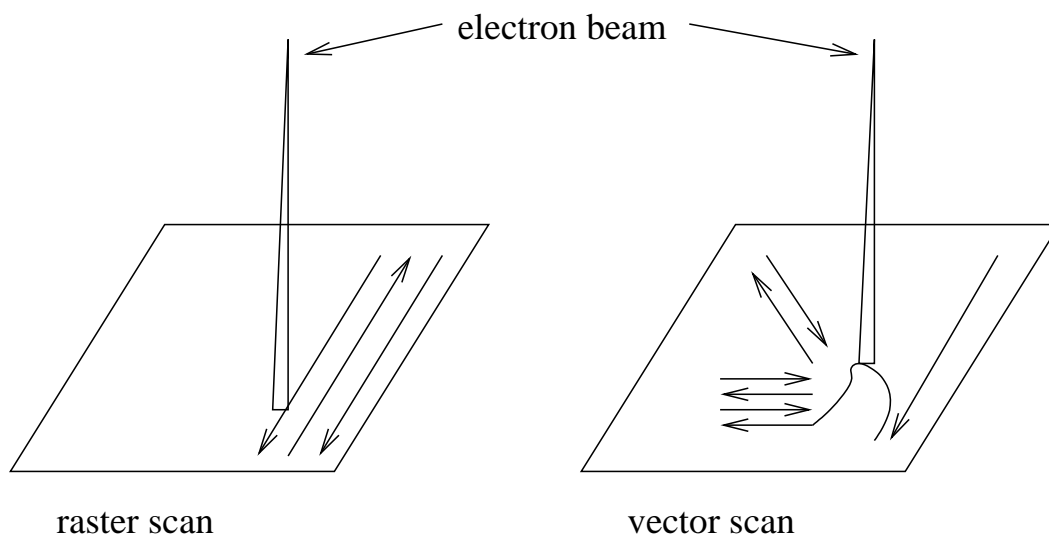


Figure 1.4: Vector scanning and raster scanning

larger beam size allows quicker image writes, but resolution suffers.

There are two methods of scanning the electron beam over the surface. One technique is the raster scan, where the beam is scanned back and forth and the image is formed by turning the beam on and off. The other method is called vector scanning where the beam is freely moved just over where the image is wanted. The two scanning methods are shown in figure 1.4.

There is work being done to speed up electron beam lithography. Several methods are using different types of stencil masks of common shapes to project an image [11] [12] [13] and expose a pattern instead of a square or a dot. Several proposals for extending photolithography involve using photolithography for the larger features in a layer and using electron beam for the critical areas[14].

Electron beam lithography is a slow, but accurate process. Electron beam lithography is necessary for the manufacture of photomasks and templates for other types of lithography. Its direct write capability and high resolution ensure that electron beam will be around for a long time.

1.3 Mechanical Pattern Replication Processes

Beam based lithography methods are limited by the wavelength of light or diameter of the particle beam. There are several alternatives to beam based lithography. Instead of using an imaging process, these methods use a mechanical pattern master to directly replicate the desired pattern. Direct replication processes do not require the complex optics or optical corrections of photolithography, but they do require 1x master pattern templates. It would seem that a 4x photomask would be easier to fabricate than a 1x mask because the features are four times larger, but the proximity corrections and subresolution assist features are approaching the same size as features on a 1x template. A 4x photomask then has the same size features as a 1x template, but has 16 times the area. This may lead to templates being cheaper than photomasks, especially for short production run products such as ASICs. Imprint lithography and electric field based lithography are examples of mechanical pattern replication processes.

1.3.1 Imprint Lithography

One alternative to photolithography is imprint lithography. Several groups are investigating different methods of imprint lithography. The characteristics that they share are that they use a relief etched template to imprint the circuit pattern in a transfer medium. There are three leading imprint technologies. Their techniques are shown in figure 1.5. In soft lithography [15], a master mask is formed by optical or electron beam lithography. The mask is coated with a polydimethylsiloxane precursor and then cured. The polydimethylsiloxane is then peeled away from the master mask. This soft mask is coated with a thiol solution that is then transferred to the substrate. Soft lithography is not believed to be suited to applications that require precise pattern placement due to the use of a soft template. Nano Imprint Lithography (NIL) is another imprint technique[16]. NIL uses a solid mold with the pattern etched into the surface. The substrate is coated with a resist. The resist is heated above its glass transition temperature and the mold is pressed into the resist. NIL can transfer precise patterns, but alignment of layers is complicated by the high temperatures and pressures.

Another development in imprint lithography is Step and Flash Imprint Lithography (SFIL)[17][18]. SFIL is being developed at The University of Texas at Austin and Molecular Imprints Incorporated². In SFIL, the pattern is etched into a transparent template. A photomask blank is the current

²www.molecularimprints.com

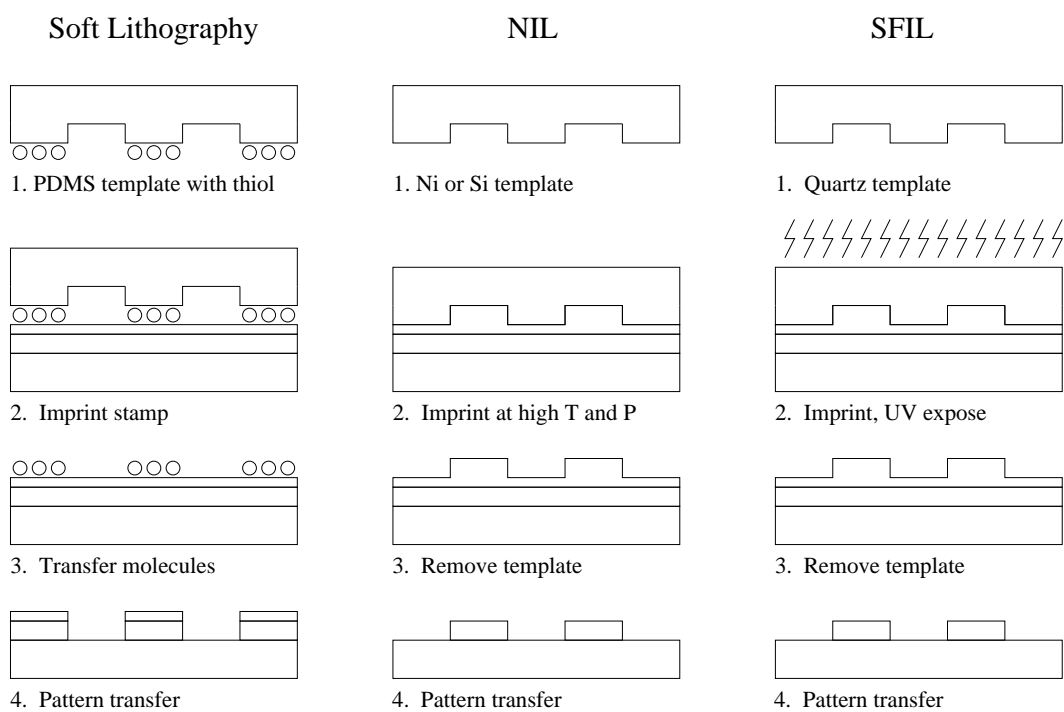


Figure 1.5: Imprint lithography

template material. The active area of the template is currently 26x32mm for a step and repeat system (Imprio 250) and can be greater than 100mm diameter for large area patterning (Imprio 1100). A transfer layer is coated on the substrate. A low viscosity monomer solution is then deposited onto the area to be imprinted. The template is pressed onto the substrate and the monomer solution is exposed with UV light. The monomer solution is designed to react with I-line light from a mercury vapor lamp. The monomer cures and the template is removed. After pattern transfer etches, the substrate is in the same state as it would be after photolithography. The imprint pressure in SFIL is less than 0.25 psi. Precise orientation of the SFIL template and substrate is necessary to form imprints with even residual film thickness. The current SFIL imprint head uses a remote center compliance to passively orient the template and substrate. The imprint film thickness variation is less than 10 nm, 3σ . Alignment is easier in SFIL than in NIL due to the lower pressures and temperatures. Sub- 20nm alignment has been demonstrated in S-FIL, and further improvement is underway to achieve sub- 10nm alignment[19].

Imprint lithography is a high resolution technique that is particularly suited for sub 40nm lithography with low line edge roughness[19]. Imprint lithography has significant potential, not only for CMOS manufacturing but also for demanding applications like bit patterned media for disk drives and photonic crystals for more efficient LEDs.

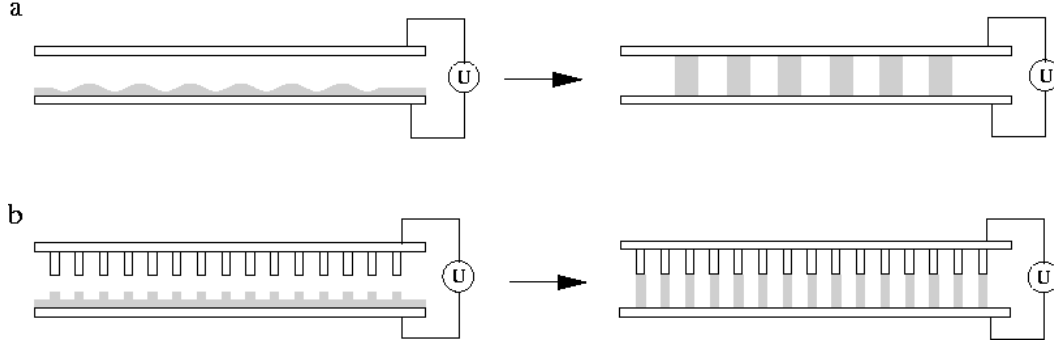


Figure 1.6: LISA schematic. In a, a surface wave grows until pillars form. In b, the film rises to touch the patterned region of the template

1.3.2 Lithographically Induced Self Assembly

In 1999, researchers at Princeton were investigating Nanoimprint Lithography when they noticed an interesting phenomenon on certain ‘bad’ samples [20]. Where a particle prevented the imprint template from touching the imprint polymer, pillars of polymer formed in the air gap between the template and the polymer film. Attempts to replicate the polymer pillars on a larger scale led to the process called Lithographically Induced Self Assembly, or LISA. In LISA, one conductive, flat electrode, typically a piece of silicon wafer, is coated with a polymer film. Another electrode, also typically a piece of silicon wafer, is brought into close proximity to the first electrode, leaving an air gap of from a few hundred nanometers to a few microns. The electrode sandwich is then placed on a hot plate to heat the polymer above its glass transition temperature. An electric field is applied and pillars form between the two electrodes. The setup is shown schematically in figure 1.6. If the top

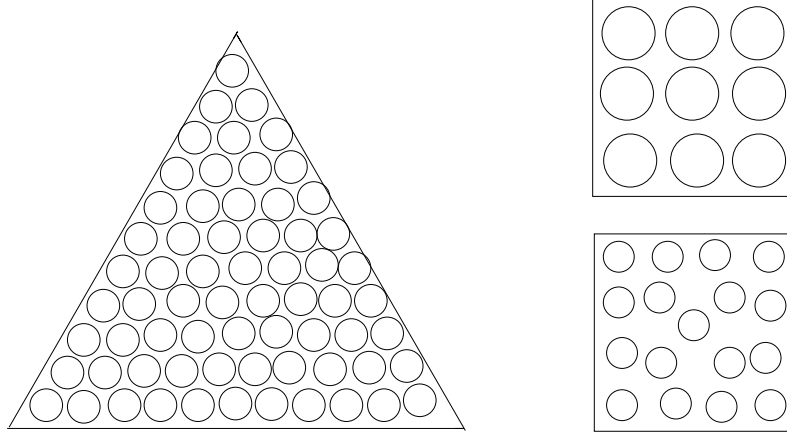


Figure 1.7: Patterns of pillars formed using LISA. On the left, a raised triangle forms a hexagonal close packed pattern. In the right, raised squared form a simple cubic pattern on the top and a face centered cubic pattern on the bottom. Which cubic pattern forms is determined by the process conditions and geometry[20].

electrode is patterned, pillars will form only under the protruding portion of the template.

The template pattern has an effect on the order of pillar formation. If the template is large and uniformly flat, the pillars form with a hexagonal order. If a raised triangle is etched into the template, the pillars again form with hexagonal order. If the raised area is rectangular, pillars form with a cubic or face centered cubic pattern. The resulting patterns can be seen in figure 1.7 [20]. If the template pattern is small and the gap is small, the pattern is replicated instead of forming pillars. 140 nm lines and spaces have been formed with this technique [21].

Pillars also form when two layers of different polymers are applied to

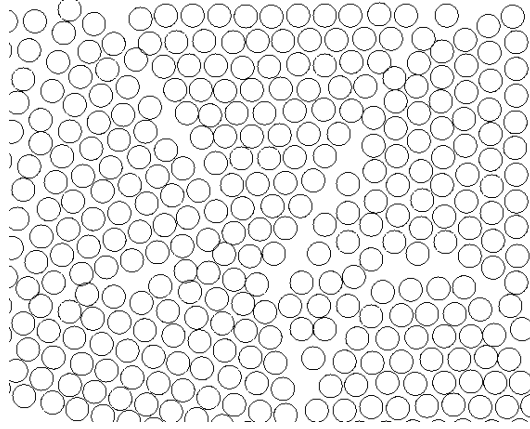


Figure 1.8: Pillars formed with LISA, showing regions of hexagonal order[20]

the substrate and the top electrode is placed so there is no air gap [22]. If the lower layer is thinner, pillars of the bottom polymer will grow from the lower electrode to the upper electrode, leaving holes in the upper layer. The upper layer can then be lifted off, forming a membrane with a pattern of holes. If the upper layer is thinner, pillars of the upper polymer will grow from the upper electrode to the lower electrode, forming holes in the lower layer. The upper layer can then be dissolved away, leaving a pattern of holes on the substrate.

1.3.2.1 LISA model

Pillars form because the electric field destabilizes the film and a surface wave forms in the film. The wave can be described by electro-hydrodynamics. The electric field generates an electrical pressure in the film[23]. The electrical pressure is opposed by surface tension and a disjoining pressure caused by Van der Waals interactions. The pressure at the surface of the film is found

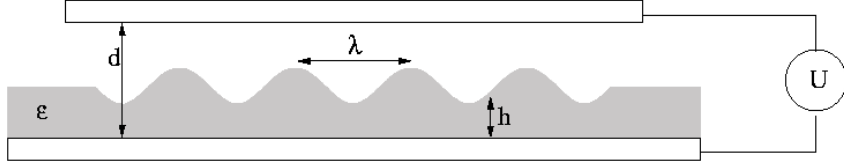


Figure 1.9: Parameters used in the LISA model. The polymer film, shown in gray, has a dielectric constant ϵ . The voltage U destabilizes the film, resulting in surface waves of wavelength λ . The wavelength is determined by the voltage, dielectric constant, electrode spacing d , and film height h .

in equation 1.2.

$$p = p_0 - \gamma \frac{\partial^2 h}{\partial x^2} + p_{el}(h(x)) + p_{dis}(h) \quad (1.2)$$

Here, p_0 is the atmospheric pressure. The second term is the Laplace pressure caused by surface tension of the fluid. In the second term, γ is the surface tension, h is the local film height, and x is the horizontal coordinate. The third term is the electrical pressure caused by the applied voltage U . The fourth term is a dispersion pressure.

The electric field in the polymer is given by

$$E_p = \frac{U}{\epsilon_p d - (\epsilon_p - 1)h(x)} \quad (1.3)$$

where E_p is the electrical field in the film, ϵ_p is the dielectric constant of the film and d is the electrode spacing. The electric field causes an electrical pressure of

$$p_{el} = -\epsilon_0 \epsilon_p (\epsilon_p - 1) E_p^2 \quad (1.4)$$

where p_{el} is the electrical pressure and ϵ_0 is the permittivity constant.

If the electric field is large, only surface tension and electric pressures need to be considered[23]. To get the wave equation, a small sinusoidal perturbation with wave number q and growth rate τ^{-1} is applied to the interface. The perturbation is

$$h(x, t) = h_0 + ue^{iqx+t/\tau} \quad (1.5)$$

Modulating h causes a lateral pressure gradient which leads to a half poissulle flow j in the film with a no slip boundary condition at the substrate and a free condition at the film surface.

$$j = \frac{h^3}{3\eta} \left(-\frac{\partial p}{\partial x} \right) \quad (1.6)$$

Equation 1.6 describes the poissulle flow, where η is the viscosity of the fluid, h is the film height, p is the film pressure, and x is the horizontal position. Mass is, of course, conserved as the film height modulates, so a form of the continuity equation applies to the incompressible fluid[23].

$$\frac{\partial j}{\partial x} + \frac{\partial h}{\partial t} = 0 \quad (1.7)$$

Equations 1.2, 1.6, and 1.7 lead to a differential equation describing the film's response to the applied perturbation[23]. Applying a linear approximation leads to a dispersion relation

$$\frac{1}{\tau} = \frac{h_0^3}{3\eta} \left(\gamma q^4 + \frac{\partial p_{el}}{\partial h} q^2 \right) \quad (1.8)$$

Fluctuations are amplified if τ is > 0 . Since $\frac{\partial p_{el}}{\partial h}$ is < 0 , the critical wavenumber q_c is

$$q_c = \sqrt{-\frac{1}{\gamma} \frac{\partial p_{el}}{\partial h}} \quad (1.9)$$

All modes with $q < q_c$ will be unstable. The fastest growing mode is the mode corresponding to the maximum in equation 1.8. The wavelength of the mode is the reciprocal of the wavenumber, $\lambda = 1/q$. The wavelength of the fastest growing mode is given in equation 1.10.

$$\lambda = 2\pi \sqrt{\frac{\gamma U}{\epsilon_0 \epsilon_p (\epsilon_p - 1)^2}} E_p^{-3/2} \quad (1.10)$$

The spacing of the pillars depends on the air gap thickness, film thickness, film dielectric constant, film surface tension, and applied voltage. This model seems to work well for describing pillars formed with the polymers used in early experiments[23]. This model and other, slightly different, models bound the published experimental data. The main difference is the functional dependence of p_{el} with the polymer dielectric constant ϵ_p [21]. In [24], a linear stability analysis is presented that predicts smaller wavelengths if the film is a leaky dielectric than if the film is a perfect dielectric.

1.3.2.2 Capabilities, Limitations, and Possible Applications

LISA can produce arrays of small pillars and line and space patterns, but some of its characteristics make it unsuitable as a production lithographic process. So far, all of the work has been done using pieces of silicon wafer clipped together on hot plates. The air gap is maintained by spacers. A wedged configuration is usually used to see behavior at many different gap thicknesses. The gap is inferred by measuring the height of the resulting pillars. Because the polymers are highly viscous and must be heated above their glass transition temperature, the pillars take minutes to form.

A useful lithographic process must have several characteristics. To control template costs and allow gap control and overlay of successive layers, the process must be able to be done on whole wafers in a step and repeat fashion. The patterning process needs to have high throughput, with a process time of a few seconds per patterning field. There needs to be low geometric variance across the entire patterned field. There must be good critical dimension control across one printed die, across all dies on a wafer, and across different wafers. Processes using heat have the added difficulty of thermal expansion. Thermal gradients make pattern overlay difficult if not impossible. LISA, as currently practiced, needs to be improved to make it a candidate process for production lithography.

There are applications that do not have the stringent requirements of production integrated circuit manufacturing. Some applications simply need arrays of pillars. Examples of these are LEDs and semiconductor lasers formed with quantum dots, patterned storage media, and certain photonics band gap devices. These devices could be made using electrical lithography if the process is improved to create uniform features across an entire exposure field. Further development of the process could make it suitable for applications with more stringent requirements. This dissertation will develop a tool for the electrical lithography process. The purpose of the tool is to control the parameters in electrical lithography and allow pillar formation over large areas with higher throughput and better uniformity.

Chapter 2

Parallel Manipulators

Pillar formation requires carefully controlled process conditions. The two electrodes must be parallel at a specific gap. The film must be uniform with a specified thickness. When the electric field is applied, the electrodes must remain in position under the attractive electrostatic force. Substrates vary in thickness and therefore the gap between and parallelism of the electrodes will vary from experiment to experiment unless the experimental setup is adjustable. Parallel manipulators offer a way to adjust the gap, electrode parallelism, and other process parameters in a repeatable and reliable manner.

2.1 Parallel Manipulators

Parallel manipulators, also called parallel robots or Stewart platforms are attractive for use in this application. In a parallel manipulator, there is a fixed base and a moving platform[25]. The base and platform are connected by several links. Each link is attached to both the base and the platform. This forms a series of “legs” in parallel instead of the links connected one after the other as in a serial manipulator such as the familiar robot arms. In nano-precision applications, the motion requirements are small and the

mechanisms used are symmetrically designed. Therefore, each of the parallel links are usually identical. Each link has a pin, universal, or spherical joint at each end and will contain an actuator, usually a prismatic motor of some sort. There are also novel designs that place the prismatic actuator before the initial rotational joint, effectively moving the rotational joint placement instead of the length between the moving and base platform [26].

The pose of the moving platform is adjusted by changing the lengths of the legs. In the classic Stewart platform, the moving platform is connected to the base by six links[27]. Each link consists of a universal joint, a prismatic actuator, and a spherical joint. The result is a manipulator with six degrees of freedom and high structural stiffness. The Stewart platform has a high load capacity but a small range of motion when compared to serial manipulators. The classic Stewart platform is used in aircraft simulators, automobile simulators, precision machining, and as a micromotion end effector on the end of a serial robot.

Not all applications require all six degrees of freedom. In some applications, having all six degrees of freedom is actually detrimental. Parallel manipulators can be built to have the desired degrees of freedom by careful choice of the number of legs, leg end joints, and joint placement. Common arrangements result in tip/tilt or tip/tilt/Z degrees of freedom. Careful kinematic design ensures that the manipulator has the desired degrees of freedom while all other degrees of freedom are constrained. In applications where very high precision is required, the joints can be replaced by flexure joints. Flexure



Figure 2.1: Two stewart platform 6-DOF parallel manipulators. Image taken from en.wikipedia.org/stewart_platform[28].

pin and universal joints are easily constructed. Flexure spherical joints are less common. Manipulator strength and stiffness can be enhanced in the unactuated degrees of freedom by adding elements such as flexure rings that have the same degrees of freedom as the manipulator and are stiff in the unactuated directions[29].

When designing the control of a parallel manipulator, the same two questions must be answered as when designing a serial manipulator. The first is, “given my link positions, where is my moving rigid body?” The second is “Given the location of my moving rigid body, what link positions do I need to get there?” These are the forward and inverse kinematic problems, respectively. The forward kinematics for a parallel robot are difficult to solve. For a given set of link lengths, there are many possible orientations, leading to a highly nonlinear geometric problem. The inverse problem is easier to

solve. For a given position and orientation, there is only one possible set of link lengths. Solving either problem requires precise knowledge of the link end point positions and link lengths. Many calibration routines have been developed to determine the necessary parameters for programmed motion [30].

Some applications do not really require knowledge of the moving platform in space, but only knowledge of the moving platform relative to another surface. Pillar array formation is one such application. In these cases, if the manipulator is carefully designed so that the operating position places the manipulator in a linear operating region, full calibration is not necessary. The position between the manipulator and the reference surface can be directly measured and the relationship changed without need for the full nonlinear kinematics. This is the approach taken in this project.

2.2 Three DOF 3-RPS Mechanism

The proposed pillar formation mechanism needs to be able to control the parallelism of the two electrodes and the total gap between them. This requirement is commonly called tip/tilt/Z. A type of parallel manipulator called the 3-RPS manipulator has been a focus of development for tip/tilt/Z applications

A schematic of the 3-RPS mechanism is shown in figure 2.2. The name 3-RPS arises from the link and joint arrangement. Each leg has a Revolute (pin) joint at the fixed platform, an actuated Prismatic joint for leg length adjustment, and a Spherical joint at the moving platform. There are three

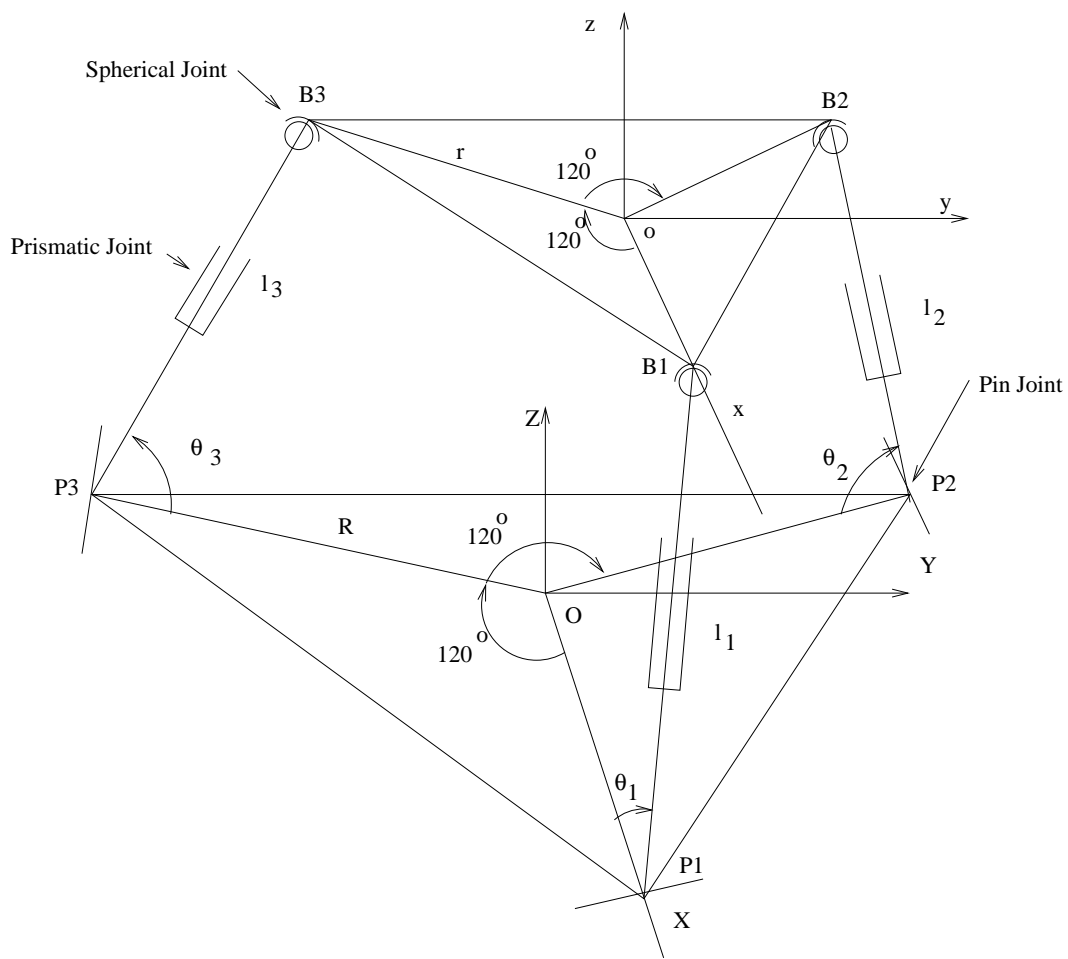


Figure 2.2: The 3-RPS parallel manipulator[31]

identical legs arranged in an equilateral triangle, hence the name 3-RPS. Lee and others [32][33][34][31][35][36] [37][38] have analyzed the kinematics and dynamics of this mechanism. The mechanism has three degrees of freedom with two orientation freedoms and one translation freedom. The freedoms are rotation about the X axis, α , rotation about the Y axis, β , and vertical translation, Z .

2.2.1 Kinematics of the 3-RPS Mechanism

To derive the forward kinematics, we start with the implicit relationship between the link lengths L_i and the subtended angles θ_i [31].

$$L_i^2 + L_j^2 + 3 - 3\rho^2 + L_1 L_j \cos \theta_i \cos \theta_j - 2L_i L_j \sin \theta_i \sin \theta_j - 3L_i \cos \theta_i - 3L_j \cos \theta_j = 0 \quad (2.1)$$

In the above equation, $i = 1, 2, 3$, $j = 1, 2, 3$, $L_i = l_i/R$, and $\rho = r/R$.

If the machine starts with the moving and stationary platforms parallel and moves on the order of micrometers, as it would in a pillar formation tool, linearization about an operating point can give a closed form solution[31]. If the two platforms are parallel, all of the leg lengths L_i are equal. The angles θ_i are therefore also equal. To linearize, set $L_i = L_0$ and $\theta_i = \theta_0$ in equation 2.1. The initial operating angle θ_0 is given by

$$\cos \theta_0 = R(1 - \rho)/L_0 \quad (2.2)$$

Now expand 2.1 in a Taylor series, noticing that

$$\left. \frac{\partial f_i}{\partial \theta_i} \right|_{\theta_0, L_0} = \left. \frac{\partial f_i}{\partial \theta_j} \right|_{\theta_0, L_0} = c_1 \quad (2.3)$$

and

$$\left. \frac{\partial f_i}{\partial L_i} \right|_{\theta_0, L_0} = \left. \frac{\partial f_i}{\partial L_j} \right|_{\theta_0, L_0} = c_2 \quad (2.4)$$

where

$$c_1 = 3L_0 \sin \theta_0 [1 - L_0 \cos \theta_0] \quad (2.5)$$

$$c_2 = -3 \cos \theta_0 [1 - L_0 \cos \theta_0] \quad (2.6)$$

The linearized equation is therefore

$$\Delta \theta_i + \Delta \theta_j = -\frac{c_2}{c_1} (\Delta L_i + \Delta L_j) \quad (2.7)$$

In the above equation, $\Delta \theta_i = \theta_i - \theta_0, \Delta L_i = L_i - L_0$ and the subscripts run from $i = 1, 2, 3, j = 2, 3, 1$. Solving the three constraint equations simultaneously for a given set of link lengths gives an uncoupled set of equations for $\Delta \theta_i$ [31]. The equation is

$$\Delta \theta_i = \frac{\Delta L_i}{L_0 \tan \theta_0} \quad (2.8)$$

This equation shows some interesting and useful properties of the mechanism. A change in link length is directly proportional to the change in subtended angle. The most interesting result is that if $\theta_0 = \pi/2$, a change in link length L_i results in no change of the subtended angle θ_i . The position and orientation

of the center of the moving platform are therefore

$$X_c = Y_c = \gamma = 0 \quad (2.9)$$

$$\Delta Z_c = \frac{1}{3} (\Delta L_1 + \Delta L_2 + \Delta L_3) \quad (2.10)$$

$$\alpha = \frac{1}{\sqrt{3}} (\Delta L_2 - \Delta L_3) \quad (2.11)$$

$$\beta = \Delta L_1 - \Delta Z_c \quad (2.12)$$

and the linearized inverse kinematics are

$$\Delta L_1 = \Delta Z_c + \beta \quad (2.13)$$

$$\Delta L_2 = \Delta Z_c - \frac{1}{2}\beta + \frac{\sqrt{3}}{2}\alpha \quad (2.14)$$

$$\Delta L_3 = \Delta Z_c - \frac{1}{2}\beta - \frac{\sqrt{3}}{2}\alpha \quad (2.15)$$

$$(2.16)$$

There are several things to notice from these equations. First, notice that the change in position and orientation depend only on the change in link length, not the absolute link length. Second, notice that micromotion control of Z , α , and β is possible without any change in X , Y , or γ [31]. A 3-RPS mechanism constructed at the special configuration of $\theta_0 = \pi/2$ would be able to control the parallelism of the moving platform and a fixed base without precise knowledge of the link lengths. If the link extension can be controlled to nanometers, then the position and orientation can be controlled in the nanoscale with out nanoscale knowledge of the link lengths. This greatly simplifies the calibration procedure, as the only measurement necessary is a measurement of the moving platform relative to the desired parallel surface.

One drawback to a mechanism with less than six degrees of freedom, such as the 3-RPS mechanism, is that loads that are not along the desired degrees of freedom must be carried as reactions at the joints. If not carefully accounted for, these reaction loads can lead to unwanted behavior. This weakness can be mitigated by appropriate joint design and by stiffening the mechanism in the weak directions with arrangements such as flexures that allow the desired movement but are stiff against the undesired movements.

2.3 Conclusion

Pillar array formation requires a mechanism that is capable of controlling the parallelism and gap between two surfaces on the micro- and nanometer scale. The 3-RPS manipulator has the required degrees of freedom. When built at the special configuration of $\theta_0 = \pi/2$, nanometer control can be achieved without nanoscale knowledge of the link lengths or joint positions. This makes the 3-RPS mechanism very appealing as a pillar formation platform from the point of view of geometric capability.

Chapter 3

Motivation and Hypothesis

A low cost process to manufacture regular arrays of pillars would have many potential applications. Photonics devices, patterned storage media, LEDs, semiconductor lasers, quantum dots, chemical and biological sensors, and many other applications make use of regular arrays of micron and nanometer size pillars or holes. Electrohydrodynamic patterning offers an intriguing method for forming the desired arrays. The high viscosity polymers most often used in the literature require hours to form pillars and large scale pillar array formation has not been accomplished on a scale larger than $400\mu\text{m}$ [39]. If electrohydrodynamic patterning is to move towards becoming a viable manufacturing process, improvements in process speed and reliability need to be achieved. Using low viscosity, photocurable polymers decreases the time required to form pillars[40]. A tool that can control the gap between the template and substrate is required to improve process uniformity and throughput. In this thesis, a process machine is developed to allow fine control of the air gap between the two electrodes to nanometer scale over large areas. Based on preliminary results[40] it is known that gap control is needed to form regular arrays of micro- and nano- scale pillars and lithographic features using photocurable electrical lithography. A tool that can control the gap between the

electrodes while the electric field is pulling them together will allow investigation of pillar formation over large areas.

3.1 Hypothesis

It is assumed, based on previous work[40], that it is possible to form regular arrays of micro-and nano- scale pillars and lithographic features using photocurable electrical lithography where the geometry of the air gap is carefully controlled. A precision machine system can be built to control the gap in the photocurable electrical lithography process. The machine will be capable of holding a transparent template close and parallel to a silicon wafer, with gaps ranging from less than 500nm to $5\mu m$, with a goal of reaching a minimum gap of 100nm. The gap between the template and wafer will change by less than 5% of the total gap when the pillar formation voltage is applied.

The remainder of this thesis is organized as follows. Measurement of the gap between the wafer and template is a necessary part of any solution, so gap sensing will be discussed first. Then early work with photocurable pillars on previously existing machines will be discussed. Next, the design requirements and design of a new pillar machine will be presented. Performance testing of the machine will be presented, including results of small gap pillar formation. Finally, conclusions and suggestions for further research will be given.

Chapter 4

Gap Sensing

In order to form predictable pillars, the air gap between the two electrodes needs to be controlled for parallelism and absolute thickness. The gap sensing requirements are the same regardless of which mechanism is used, and the gap sensing requirements drive the machine requirements, so gap sensing will be discussed first. Measuring the thickness of thin films is a classical problem and many accurate methods exist[41]. In order to use gap sensing for gap control, the measurement system needs to be fast. The focus of the gap sensing system developed here is fast, accurate film thickness measurement when the other optical constants are known. The gap needs to be measured at at least three spots to allow control of orientation and gap thickness. The gap sensors need to return the gap in real time so it can be used in the control scheme. The design of the machine places some limitations on the gap sensors. Any gap sensor needs to operate at normal or near normal incidence with a footprint small enough to allow three sensors within the area of the template. The gap sensors need to either sense through the template, be built into the template, or be located right at the edge of the template. The top electrode in the photocurable pillar process is a transparent fused silica template, which allows for a number of optical sensing options. A sensing method that can

not be used in the control scheme may still prove useful in characterizing the sensing method used for control as well as determining the optical properties of the film in use. Several options were evaluated when the Active Gap tool was first built and spectral reflectance was chosen as the best option. When the active gap tool was updated for use in the pillar formation process, the problem of gap sensing was revisited and spectral reflectance was again chosen. The data analysis method was improved to allow real time analysis and to accurately detect multiple film thicknesses.

4.1 Sensing Alternatives

There are several options for measuring the thickness of micron sized and smaller air and polymer films. Each alternative has advantages and disadvantages. The sensing options explored for this process include ellipsometry, laser capacitive sensing, interferometry, and spectral reflectance.

4.1.1 Ellipsometry

Ellipsometry is a highly accurate method for measuring the thickness and other properties of thin films[41]. In ellipsometry, a beam of white polarized light is shined at an angle onto the film and substrate. The reflected light is then measured. The polarization direction is rotated and the difference in reflection at different polarization angles is related to the film thickness. The difference in reflectivity of the different polarizations is highest when the incident light is at Brewster's Angle. For a silicon wafer substrate, Brewster's

angle is 70 degrees. This means that in order to use ellipsometry the light must have a clear path from the light source to the substrate to the sensor at 70 degrees from the vertical. The spot size is usually around 10mm long and 3 mm wide. That is much too large a spot size for use in the gap control scheme for pillar formation. The ellipsometer data must also be analyzed after it is taken and not in real time. The incident angle, spot size, instrument size, and post processing requirements make ellipsometry unsuitable for use in the gap control scheme. However, ellipsometry is useful in characterizing other sensing methods and in determining the optical properties of the films used.

4.1.2 Capacitive Sensing

Capacitive sensing senses the gap between two electrodes by measuring the capacitance between the electrodes. Properly calibrated capacitive sensors can measure the gap between the electrodes to within nanometers[42]. To measure the gap using capacitance, the silicon wafer would be one electrode and the sensor would be the other. Due to the geometry of the system, the sensor electrode would have to be built into the template. While this is possible, it complicates template construction. Placing capacitive sensors around the perimeter of the template is another possibility, but calibrating the sensors becomes a major challenge that would need to be repeated each time a template is installed. Another complication with either sensor placement option comes from the polymer film. The film in the gap changes the capacitance due to its dielectric nature. Each film has a different dielectric constant, and

different film thicknesses will affect the capacitance differently. These effects can be calibrated, but they add to the uncertainty. Also, when the pillars start to form, the capacitance change becomes unpredictable. Once the electric field is applied, the capacitance measurement is complicated. This makes capacitance sensing a possibility for initial calibration, but not for use in pillar stretching experiments or for keeping the system level after the electric field is applied. The complicated construction and sensing difficulty during pillar formation are why this sensing method was not chosen.

4.1.3 Laser Interferometry

Laser interferometry is a widely used method for measuring minute changes in length. In laser interferometry, a laser beam is split into two beams. One of the beams follows a fixed path length to a detector. The other beam follows a path to the length being measured and is then returned to the detector. The beams are combined and the difference in path length leads to constructive or destructive interference based on the difference in path length. The interference signal is periodic with changing path length difference, so change in path length is detected precisely, but the absolute length is unknown. If another method can measure the absolute distance, then laser interferometry can be used to measure the subsequent changes. Laser interferometry uses a small footprint on the part being measured, but it requires mirrors, beam splitters, lasers, and detectors which complicate the machine design. The need to have another measurement method to make absolute measurements and the

complicated machine design are why laser interferometry was not chosen for this project.

4.1.4 Reflectance Spectroscopy

Reflectance spectroscopy measures film properties using the interference that occurs in thin films illuminated by white light[41]. The effect can be seen in the thin layer of oil that often floats on top of rain puddles in the road. It can also be seen in the colored fringes between two flat, clean pieces of glass. As the film thickness changes, the interference pattern changes as wavelengths that were interfering constructively begin to interfere destructively and vice versa. The interference spectrum is unique for a given film thickness. If the film has constant thickness, it will appear to have one color made up of the wavelengths that interfere constructively. In the early days of the semiconductor industry, film thicknesses were measured by comparing the film color with the color of samples of known thickness. Film thicknesses could be determined to within a few nanometers using nothing more than the human eye as a comparison tool.

In an instrumentation system, reflectance spectroscopy can be implemented with a fiber optic light source and spectrometer[41]. The only parts that need to be placed in the machine are the fiber optic reflection probes and the lenses for focusing the sensign light. Three reflection probes can be placed in the machine to measure the gap thickness at three different places. There are several commercial products that use reflectance spectroscopy to

measure film thickness and other optical properties. The commercial systems use complex fit models to extract the film thickness and other properties. They provide high accuracy, but require post processing. The gap control scheme for this project needs to measure film thickness but the other optical properties are unimportant, so a simpler fit model can be used. With the system in use today, a sample rate of 5 Hz is possible. Newer spectrometers can sample much faster, with optical sample rates approaching 1 kHz. Faster computers can also decrease the computation time, allowing for a sampling rate of at least 30 Hz. Reflectance spectroscopy for gap sensing can provide the sample rate needed for control, can measure the absolute gap, has a small footprint on the tool, and operates by looking vertically through the template. Since it is the only method that meets all of the requirements, reflectance spectroscopy was chosen to measure the gap in this machine. In the next sections, the interference theory and data analysis methods will be described.

4.2 Reflectance Spectroscopy

Reflectance spectroscopy operates by measuring the intensity of light reflected from a surface over a range of wavelengths. In our system, light reflects from the template surfaces and from the silicon wafer (see Fig. 4.1.) If the template surface is close enough to the wafer, an interference pattern will form. The shape of the interference pattern can be related to the film thickness. The properties of the reflectance pattern are well known [43], so the full derivation with reflectances and absorbances will not be presented here.

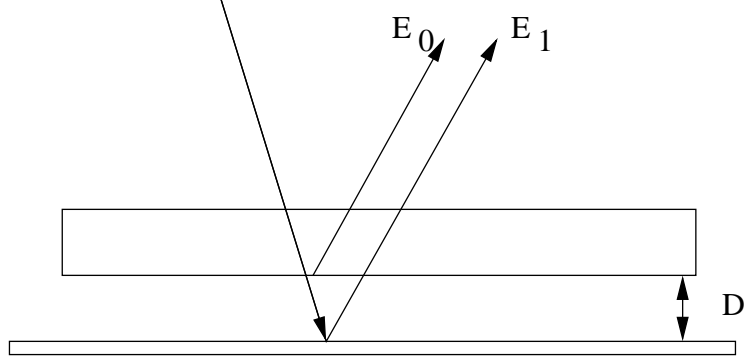


Figure 4.1: Reflected rays in one film interference

We will, however, derive the interference pattern assuming the reflectances are known and there is no absorbance. The goal of this derivation is to find a property of the sampled reflectance spectrum that can be related to the gap. The estimation of this property can then be used to estimate the gap[41].

4.2.1 Single Film Interference

Let us consider the situation in Fig. 4.1. The rays are drawn at an angle for clarity, but they are actually vertical. The fact that the incident and reflected light are perpendicular to the wafer surface simplifies the analysis tremendously since the angle effects of Snell's law can be ignored. The electric field of the incident wave in complex notation is[43]

$$E_0(\lambda) = E_0(\lambda)e^{i(\omega t + kx + \epsilon)} \quad (4.1)$$

This wave reaches the active surface of the template and part of it

reflects back toward the sensor. The rest of the ray travels through the gap and reflects from the wafer surface. When the ray reaches the template surface again, it interferes with the first reflection. The second wave is

$$E_1(\lambda) = E_1(\lambda)e^{i(\omega t + kx + \epsilon + \frac{4\pi nD}{\lambda})} \quad (4.2)$$

The last term is the optical path length traveled by the second wave and not the first. The wave travels through the gap twice, hence the 4π instead of 2π . The two waves add, creating the interference pattern.

$$E(\lambda) = E_0(\lambda)e^{i(\omega t + kx + \epsilon)} + E_1e^{i(\omega t + kx + \epsilon + \frac{4\pi nD}{\lambda})} \quad (4.3)$$

The interference pattern shows up in the intensity of the light, which is the electric field times its complex conjugate.

$$\begin{aligned} I &= E_0(\lambda)^2 e^{i(\omega t + kx + \epsilon) - i(\omega t + kx + \epsilon)} \\ &+ E_1(\lambda)^2 e^{i(\omega t + kx + \epsilon + \frac{4\pi nD}{\lambda}) - i(\omega t + kx + \epsilon + \frac{4\pi nD}{\lambda})} \\ &+ E_0(\lambda)E_1(\lambda)e^{i(\omega t + kx + \epsilon) - i(\omega t + kx + \epsilon + \frac{4\pi nD}{\lambda})} \end{aligned} \quad (4.4)$$

$$I = E_0(\lambda)^2 + E_1(\lambda)^2 + E_0(\lambda)E_1(\lambda)e^{-i\frac{4\pi nD}{\lambda}} \quad (4.5)$$

We are only interested in the real portion of the intensity,

$$I = E_0(\lambda)^2 + E_1(\lambda)^2 + E_0(\lambda)E_1(\lambda)\cos\left(-\frac{4\pi nD}{\lambda}\right) \quad (4.6)$$

Since the cosine is an even function, we can drop the sign in the cos argument. The equation then becomes

$$I = E_0(\lambda)^2 + E_1(\lambda)^2 + E_0(\lambda)E_1(\lambda) \cos\left(\frac{4\pi nD}{\lambda}\right) \quad (4.7)$$

This equation is of the form

$$I = A + B \cos\left(\frac{4\pi nD}{\lambda}\right) \quad (4.8)$$

There are a few things to notice about this equation. First, notice that the interference intensity is periodic in $1/\lambda$, or wavenumber, with a different frequency for each gap thickness[41]. This means that the gap can be determined by estimating the frequency of the interference function. This also shows the first difficulty of the data analysis, that the interference is periodic in wavenumber instead of wavelength. Spectrometers usually sample periodically in wavelength, so interpolation is necessary for any numerical methods that require equally spaced samples.

Next, notice that the signal strength at a given wavelength depends on the incoming signal strength at that wavelength. In order to measure the interference frequency, the signal needs to be normalized by the incoming strength versus wavelength[41]. This is done by taking a reference signal with the template about $200\mu m$ above the wafer. At that height, interference effects are negligible, so the measured reference signal is

$$I \approx E_0(\lambda)^2 + E_1(\lambda)^2 \approx A(\lambda) \quad (4.9)$$

Dividing the interference signal by this reference signal results in

$$GapSig = 1 + \frac{B(\lambda)}{A(\lambda)} \cos\left(\frac{4\pi nD}{\lambda}\right) \quad (4.10)$$

If the reflectance is constant across the wavelengths of interest, $E_0(\lambda)$ and $E_1(\lambda)$ will differ by a constant multiplier. Therefore, $A(\lambda)$ and $B(\lambda)$ will differ by a constant multiplier, making $B(\lambda)/A(\lambda)$ constant across the wavelengths of interest. If we call $B(\lambda)/A(\lambda)$ C , the interference signal becomes

$$GapSig = 1 + C \cos\left(\frac{4\pi nD}{\lambda}\right) \quad (4.11)$$

The frequency of this signal is related to the gap. The intensity of the input light is not completely constant with time, so $B(\lambda)/A(\lambda)$ is not exactly constant. This shows up as noise in the gap signal.

The issue of dispersion deserves some attention. The index of refraction, n , is not, in general, constant for all wavelengths[41]. The index of refraction will in general vary with wavelength. The films used in the pillar process are non-absorbing dielectrics, so the Cauchy model applies. The index of refraction is therefore

$$n(\lambda) = A + \frac{B}{\lambda^2} + \frac{C}{\lambda^4} \quad (4.12)$$

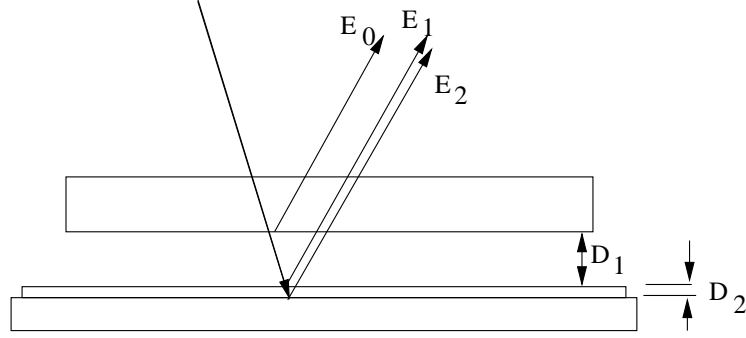


Figure 4.2: Reflected rays in two film interference

This makes the interference function periodic in $n(\lambda)/\lambda$ instead of $1/\lambda$. The dependence of the index of refraction on wavelength will have consequences in the data analysis algorithm.

4.2.2 Two Film Interference

When making pillars, there is a thin film of pillar material on the wafer and an air gap between the film and the template. This arrangement forms a two film interference pattern, as seen in Fig. 4.2. The interference signal from this arrangement is more complex than the single film interference pattern. The signal derivation follows the same steps as in the single film case. There are three reflected waves, E_0, E_1 , and E_2 . The extra optical path traveled by E_1 is $\frac{4\pi n_1 D_1}{\lambda}$ and the extra path traveled by E_2 is $\frac{4\pi n_1 D_1}{\lambda} + \frac{4\pi n_2 D_2}{\lambda}$. Let us call these optical paths δ_1 and $\delta_1 + \delta_2$, respectively. The electrical fields become

$$E_0 = E_0 e^{\omega t + kx} \quad (4.13)$$

$$E_1 = E_1 e^{\omega t + kx + \delta_1} \quad (4.14)$$

$$E_2 = E_2 e^{\omega t + kx + \delta_1 + \delta_2} \quad (4.15)$$

The superposed waves are

$$E = E_0 e^{\omega t + kx} + E_1 e^{\omega t + kx + \delta_1} + E_2 e^{\omega t + kx + \delta_1 + \delta_2} \quad (4.16)$$

To get the intensity, multiply by the complex conjugate

$$\begin{aligned} I &= E_0^2 e^{\omega t + kx - \omega t - kx} + E_1^2 e^{\omega t + kx + \delta_1 - \omega t - kx - \delta_1} \\ &+ E_2^2 e^{\omega t + kx + \delta_1 + \delta_2 - \omega t - kx - \delta_1 - \delta_2} + E_0 E_1 e^{\omega t + kx - \omega t - kx - \delta_1} \\ &+ E_1 E_2 e^{\omega t + kx + \delta_1 - \omega t - kx - \delta_1 - \delta_2} + E_0 E_2 e^{\omega t + kx - \omega t - kx - \delta_1 - \delta_2} \end{aligned} \quad (4.17)$$

Simplifying this equation leads to

$$\begin{aligned} I &= E_0^2 + E_1^2 + E_2^2 + E_0 E_1 e^{-\delta_1} \\ &+ E_1 E_2 e^{-\delta_2} + E_0 E_2 e^{-\delta_1 - \delta_2} \end{aligned} \quad (4.18)$$

Again, we are only interested in the real portion

$$\begin{aligned} I &= E_0^2 + E_1^2 + E_2^2 + E_0 E_1 \cos(-\delta_1) \\ &+ E_1 E_2 \cos(-\delta_2) + E_0 E_2 \cos(-\delta_1 - \delta_2) \end{aligned} \quad (4.19)$$

Substituting for δ_1 and δ_2 leads to

$$\begin{aligned}
I = & E_0^2 + E_1^2 + E_2^2 + E_0 E_1 \cos\left(\frac{4\pi n_1 D_1}{\lambda}\right) \\
& + E_1 E_2 \cos\left(\frac{4\pi n_2 D_2}{\lambda}\right) + E_0 E_2 \cos\left(\frac{4\pi n_1 D_1}{\lambda} + \frac{4\pi n_2 D_2}{\lambda}\right)
\end{aligned} \tag{4.20}$$

There are several things to notice in this equation. As in the single film case, there is a constant intensity term equal to the sum of the intensities of the interfering waves. There are *two* films that generate *three* interference terms. There is one interference term for each film thickness, and another interference term for the *sum* of the two optical path differences. This allows us to determine whether there is a clean film with a clean air gap or if the fluid film has bridged the gap and left spots with no residual film. In the first case, there will be three interferences, and in the second there will be two.

The two film case, like the one film case, needs to have a reference signal recorded and removed. The reference is captured by moving the clean wafer to the same reference position as in the air gap only case. The wafer is then removed and coated with the pillar fluid and replaced. Dividing the interference signal by the reference signal results, after skipping a few steps, in

$$I = A + B \cos\left(\frac{4\pi n_1 D_1}{\lambda}\right) + C \cos\left(\frac{4\pi n_2 D_2}{\lambda}\right) + D \cos\left(\frac{4\pi n_1 D_1}{\lambda} + \frac{4\pi n_2 D_2}{\lambda}\right) \tag{4.21}$$

The frequencies, and hence the thicknesses, can easily be determined using this model. Another thing to notice is that each interference term has a different intensity. One interference term can be so strong compared to the others that it becomes hard to measure the others. Experience with the experimental system has shown that when the air gap is large, ($> 50\mu m$), the film interference is often so strong that the air gap interference is hard to determine. Removing the film interference is desirable to allow determination of the air gap. To do this, another reference signal, this one with a coated wafer at the reference position, is taken. The gap signal is then divided by the film reference. The film reference equation is the same as the one film interference case (equation 4.11). The equations are recast as exponentials for convenience. The film reference is

$$Filmref = A + Be^{\left(\frac{4\pi n D_1}{\lambda}\right)} \quad (4.22)$$

and the gap signal is

$$GapSig = A + Be^{\left(\frac{4\pi n_1 D_1}{\lambda}\right)} + Ce^{\left(\frac{4\pi n_2 D_2}{\lambda}\right)} + De^{\left(\frac{4\pi n_1 D_1}{\lambda} + \frac{4\pi n_2 D_2}{\lambda}\right)} \quad (4.23)$$

Dividing $GapSig$ by $Filmref$ results in

$$I = 1 + \frac{Ce^{\left(\frac{4\pi n_2 D_2}{\lambda}\right)} + De^{\left(\frac{4\pi n_1 D_1}{\lambda} + \frac{4\pi n_2 D_2}{\lambda}\right)}}{A + Be^{\left(\frac{4\pi n D}{\lambda}\right)}} \quad (4.24)$$

The frequency content of this signal is not obvious, and the continuous Fourier transform is difficult, if not impossible, to derive. To see the frequency content of this referenced signal, we need to use the fast Fourier transform. This is

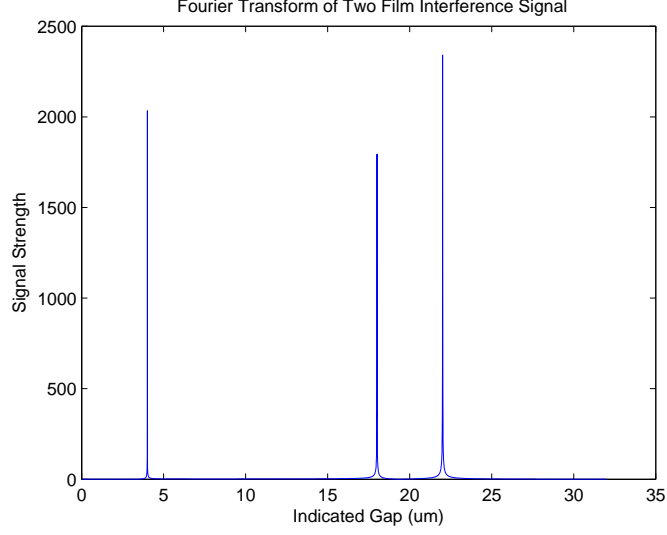


Figure 4.3: Fourier transform of simulated two film interference

accomplished by simulating a noise free two film interference signal and a noise free film reference signal. The two film signal is divided by the reference signal and the fast Fourier transform of the resulting signal is taken. The fast Fourier transform of the interference signal is also taken for comparison. The two film interference signal is shown in figure 4.3.

The three interference frequencies corresponding to the fluid film, air gap, and the film plus the air gap are clearly visible. Dividing the simulated signal by the film reference results in the spectrum shown in figure 4.4. In this case, eight peaks are seen in the spectrum. The strongest are the peaks resulting from the air gap and the air gap plus the film thickness. The other peaks are located at frequencies corresponding to one or more film thicknesses higher or lower than the two main peaks. In practice, the two main peaks are

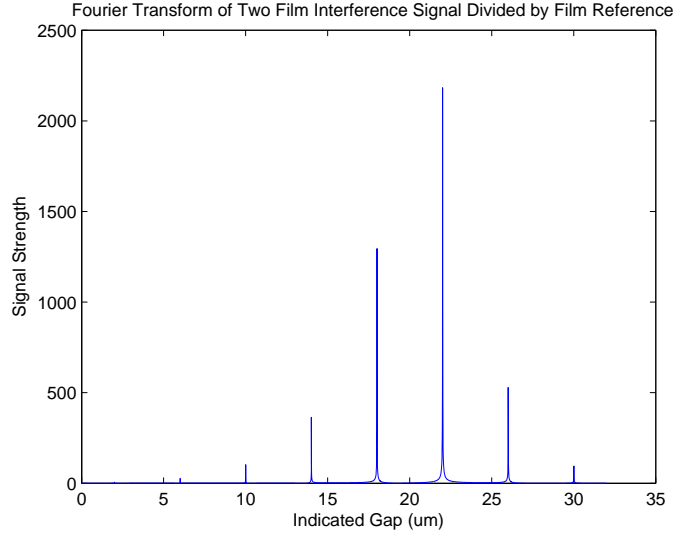


Figure 4.4: Fourier transform of simulated two film interference divided by the film reference

strong and the extraneous peaks disappear in the noise.

One more case involving the film reference is of interest. The intensity of the film interference can change over time. This change in intensity affects the effectiveness of the film reference in removing the film signal. The effect of unequal film reference and film signal strengths can be seen in figure 4.5. The signal resulting from the film thickness is not completely removed. This can complicate estimating the air gap when the gap is large and the interference signal correspondingly small. In practice, this is not a problem if the experiment is run quickly. The background signal tends to drift as time goes on, so experiments that take longer to run tend to have more problems with the effects of bad reference signals.

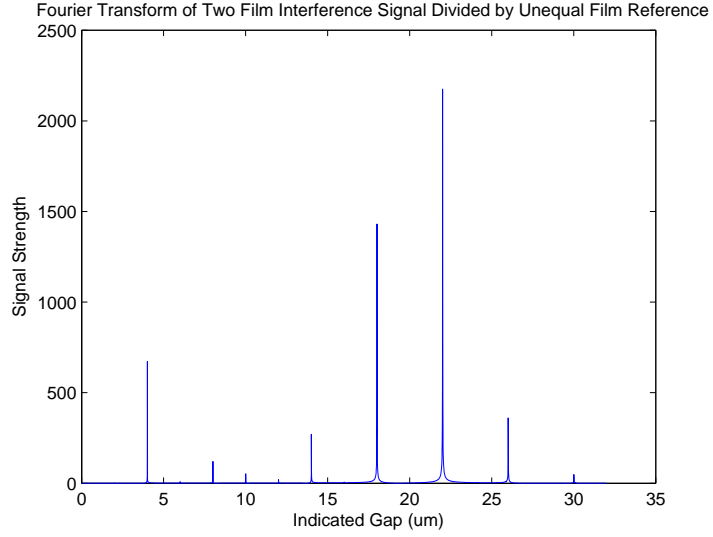


Figure 4.5: Fourier transform of simulated two film interference divided by an unequal film reference

4.2.3 Summary

The reflectance spectroscopy signals resulting from an air gap between the template and the wafer and from a fluid film and air gap between the template and wafer have been derived. The resulting signals can be represented as frequencies in the signal. The film thicknesses can be estimated by estimating the frequencies in the interference spectrum versus wavenumber. Using a film reference to remove the film signal results in a signal with the two signals of interest as well as low amplitude artifacts. The numerical methods that can be used to estimate the frequencies will now be presented.

4.3 Frequency Analysis Methods

Reflectance spectroscopy of the gap between the template and wafer results in a signal that is periodic with $n(\lambda)/\lambda$. Two films result in three frequencies in the signal. An accurate estimate of the frequencies in the spectroscopic signal will result in an accurate estimate of the gap and film thicknesses[41]. There are several challenges to be overcome in determining the frequency content of the signal. Several frequency estimation techniques can be used to determine the gap. The challenges will be presented first, followed by the estimation methods.

4.3.1 Frequency Estimation Challenges

The first challenge in frequency estimation arises because the signal is periodic in wavenumber instead of wavelength. Spectrometers naturally sample periodically in wavelength, so the samples are not equally spaced in wavenumber. Most frequency estimation techniques require evenly spaced samples. The signal must therefore be interpolated onto a regular grid that is periodic in wavenumber. This interpolation has the effect of increasing uncertainty and reducing the number of samples available for analysis. In the experimental system in use, the spectrometer returns 2048 samples. Of these, just over 1000 samples are in the region of interest between 400 and 800 nanometers. The number of interpolation points is limited by the maximum sample spacing. For the system in use here, the maximum number of interpolation points is 512. Most frequency estimation methods achieve lower

uncertainty as 'time' goes on. The 'time' variable in this situation is wavenumber, and the number of data points is fixed by the spectrometer and interpolation parameters. This limitation on the number of data points limits the frequency resolution of certain frequency estimators and limits the minimum uncertainty of others. The uncertainty issues brought about by interpolating onto an evenly spaced grid can be avoided by choosing an estimator that can use the unevenly spaced data directly.

4.3.2 Fourier Transform Methods

One of the most popular algorithms when estimating the frequency content of sampled data is the Discrete Fourier Transform, or DFT[44]. The DFT takes the sampled data array from the time domain and returns an array of transformed data in the frequency domain. The DFT assumes that the data contains one period of a periodic function. The DFT determines the coefficients of the Fourier series that would produce the data. The DFT returns an array of complex numbers that represents the frequency spectrum of the data. A peak in the spectrum indicates presence of the corresponding frequency in the sampled data. The DFT, especially the computationally efficient version known as the Fast Fourier Transform, is widely used for estimating spectra to determine resonances, filter transfer functions, and in many other situations where knowledge of the frequency spectrum in a signal is required. The DFT does have some serious limitations. The DFT has been used with reflective spectroscopy to estimate film thickness[41]. The properties of the DFT and its

capabilities and limitations with regard to gap sensing will now be explored.

4.3.2.1 Resolution

One property of the DFT is a fixed frequency resolution. The resolution is fixed because the DFT assumes the data is one period of a periodic function. The frequency resolution is $1/T$, where T is the total 'time' from the start of sampling to the end of sampling. In reflectance spectroscopy, the 'time' variable is the wavenumber. If the data of interest is from 400 nm to 800 nm, the frequency resolution is [44][41]

$$\Delta f = \frac{1}{\frac{1}{400} - \frac{1}{800}} = \frac{1}{.00125} = 800nm \quad (4.25)$$

A frequency resolution of 800nm is not enough to control orientation to within 5nm. The frequency resolution of the DFT can be increased, but not without cost. To increase the resolution, the sample data is appended with a long series of zeroes [41]. If the data series is zero padded to 64 times its original length, the resolution becomes 12.5nm. This resolution could reasonably be used for control. The frequency resolution can be made arbitrarily small by zero padding, but the benefit comes at a cost. Let's consider an ideal, noise free signal generated by a $10\mu\text{m}$ gap. This signal is sampled and interpolated onto 512 data points. The FFT of the resulting signal is shown in figure 4.6. In all of the following figures, the frequency axis is zoomed in to show the detail in the spectrum. The actual Nyquist frequency is around $100\mu\text{m}$ in this situation. Note how much space on the gap axis there is between the

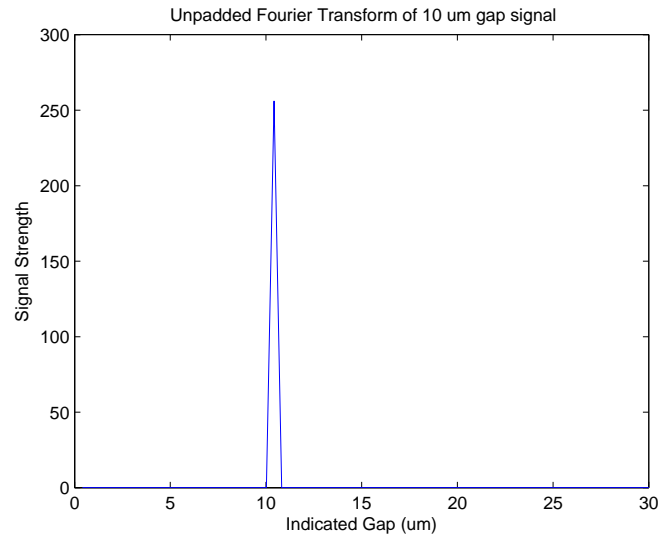


Figure 4.6: Unpadded Fourier transform of simulated 10 μm air gap

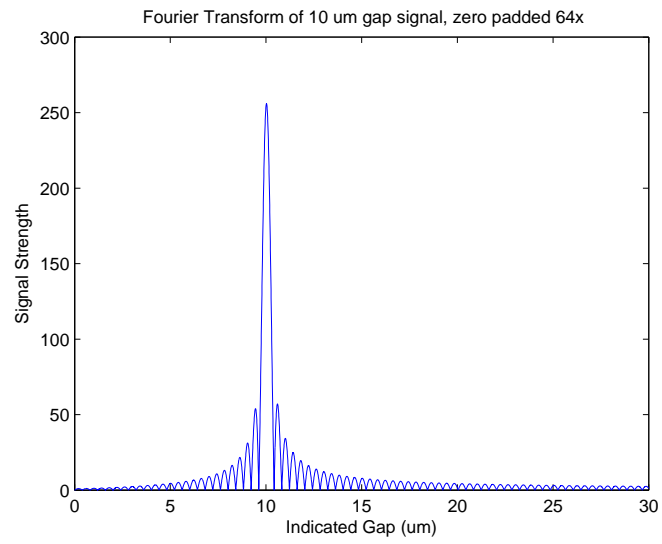


Figure 4.7: Fourier transform of simulated 10 μm air gap, zero padded 64x

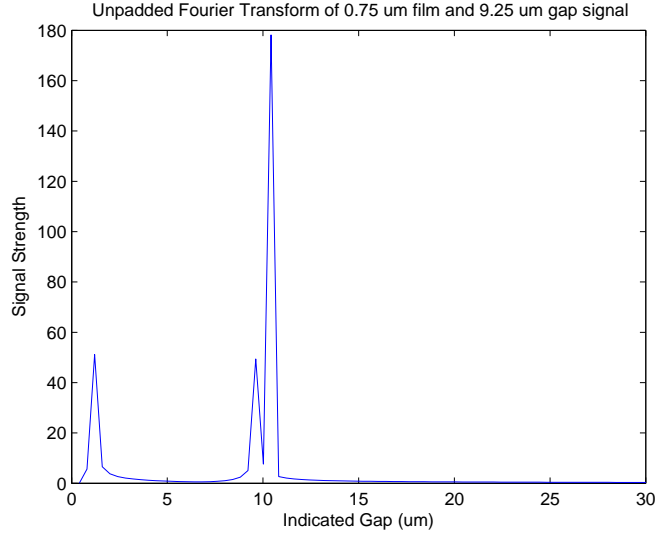


Figure 4.8: Unpadded Fourier transform of simulated $0.75\mu\text{m}$ film and $9.25\mu\text{m}$ air gap

data points. The same signal, zero padded to 64 times its original length, is shown in figure 4.7. The data points are 64 times closer than in the previous example. The actual position of the spectral peak is easier to estimate, but there are artifacts that resemble a sinc function to either side of the true peak. In this case, the frequency of the true peak could be estimated in spite of the artifacts, so there appear to be minimal drawbacks to zero padding. This is not the case in two film interference. Figure 4.8 shows the spectrum that results from a $0.75\mu\text{m}$ film with a $9.25\mu\text{m}$ air gap. The relative amplitudes of the peaks are representative of those seen in the experimental system. As in the one film unpadded case, there is a large uncertainty in the true frequency. Figure 4.9 shows the same films, zero padded 64 times. The true positions

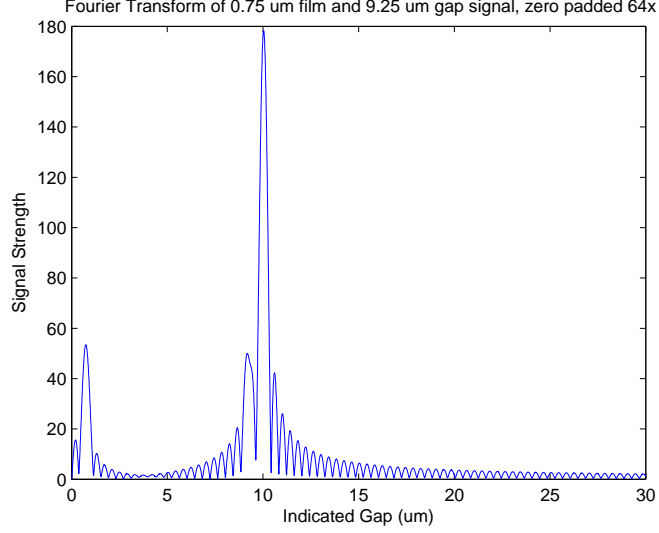


Figure 4.9: Fourier transform of simulated 10 μm air gap, zero padded 64x

of the film and air gap + film can be determined more easily, but notice the third peak. The data from the true peak is blending with the artifact resulting from zero padding. The zero padding artifacts make it impossible to determine whether weaker interference effects are occurring. The weaker components of the signal give clues about what is physically happening, such as whether there is a film and air gap structure or whether there are pillars surrounded by air. Another drawback to the zero padded FFT is the computation requirement. The FFT requires on the order of $n \log n$ operations to calculate the spectra, where n is the number of data points. In the unpadded case, a 512 point FFT is calculated. If the signal is zero padded 64 times, a 32768 point FFT is calculated. Zero padding the signal by 64 times results in over 100 times the computational requirements. In the experimental system, the zero padded

FFT resulted in very slow data rates. In many image processing processes, images are zero padded to the next power of two to take advantage of the computational efficiency of the FFT. They are not zero padded further because of the artifacts generated.

A final word on zero padding concerns the estimate uncertainty. The uncertainty of the unpadded and padded FFT are actually the same. The uncertainty of an estimate is determined by the likelihood function for the situation. The likelihood function is not dependent on things like zero padding, but is determined by the properties of the sampled data. The likelihood function for the spectral data is the same for both cases. The zero padded FFT is better at finding the peak of the likelihood function, but the uncertainty is not decreased. The resolution is increased, but the uncertainty is unaffected.

The unpadded FFT does not have sufficient resolution, and the zero padded FFT requires a lot of computational power and corrupts the spectrum. For these reasons, the FFT is not suitable as a frequency estimator for the real time gap sensing system.

4.3.3 Zero Crossing and Peak Detection Methods

Another class of frequency, and therefore gap, estimation methods is methods derived from determining the location of either sinusoid peaks and valleys or zero crossings. This information can lead to an estimate of the sinusoidal period and therefore the gap.

4.3.3.1 Peak Detection Methods

The peaks in the reflected spectrum are unique for a given film thickness. Accurate determination of the peak locations can lead to a computationally efficient and accurate method of film thickness measurement. The peaks and valleys of the sinusoidal signal occur when the derivative of Eqn 4.11 is 0. Taking the second derivative would separate the peaks from the valleys, but since we know they alternate taking the second derivative is unnecessary. The derivative is

$$\frac{d}{d\lambda} = \sin \frac{4\pi nD}{\lambda} \frac{1}{-\lambda^2} \quad (4.26)$$

The derivative of the above equation is 0 when the argument of the sin is 0. The peaks and valleys are therefore located at

$$\lambda = \frac{4\pi nD}{j} \quad (4.27)$$

where j is the order of the peak. If we have the locations of the peaks and/or the valleys, we can arrive at a determination of the film thickness in one of two ways. We can solve Eqn. 4.27 for D and get an estimate of the gap for each peak detected or we can use the peaks to arrive at an estimate of the period and then get an estimate of the gap. The first method requires that we know the order of each peak. The second method doesn't require knowledge of the order of the peak, but it only returns one frequency estimate instead of many that can be averaged.

When the peak detection algorithm is properly tuned, it returns good thickness estimates. If the Cauchy coefficients of the film material are known, the film thickness estimates agree with the ellipsometer to within one nanometer. However, when the algorithm is not properly tuned, the results are inconsistent. The required tuning is in the peak detection algorithm, not in the conversion of peak information to gap estimates. The peak detection algorithm needs to know the minimum expected height and width of the peaks a priori. If the peak height or width threshold are too low, noise will be detected as actual peaks. If they are set too high, legitimate peaks will be missed. The height and width of the peaks vary greatly over the range of film thicknesses encountered in this project, and no one set of peak detection parameters will work over the entire range. The algorithm needs to be continuously monitored to ensure the detection parameters are updated and the peaks are appropriately detected. The peak detection algorithm is fast and accurate when properly tuned, but the need to monitor it and constantly update the peak detection parameters makes it unsuitable for real time gap control. The peak detection algorithm also cannot estimate two frequencies.

4.3.3.2 Zero Crossing Methods

A close cousin of peak detection is zero crossing detection. Instead of locating the peaks and valleys, the locations where the signal crosses the axis are found[45]. These locations lead directly to an estimate of the period, and in our case, the gap. The zero axis is determined by correcting the signal to

have a zero mean. Once an initial estimate of the period is found, it can be used to start a least squares fit on the signal to further refine the estimate.

Zero crossing methods have many of the same drawbacks as peak detection methods. Noise can give false zero crossings. The signal is also not a uniform sinusoid with constant amplitude. The axis of the sinusoid is not constant, making zero crossing detection difficult. The wavelength range with strong interference changes as the gap changes, further hampering zero crossing detection. Zero crossing detection can give good gap estimates, but the algorithm must be monitored, much like the peak detection methods. Multiple frequencies cannot be detected with the zero crossing methods. Zero crossing methods are therefore not suitable for real time gap sensing for gap and orientation control.

4.3.4 Auto Regressive Moving Average (ARMA) Methods

It is well known that a properly tuned second order filter can annihilate a discrete time sinusoid[46]. Quinn and Fernandez have developed by an estimator using this principle. A description of the algorithm follows.

If a time sequence $y(t)$ satisfies

$$y(t) = A \cos \lambda t + \phi + x(t) \quad (4.28)$$

where $x(t)$ is a noise term, then

$$y(t) - 2 \cos \lambda y(t-1) + y(t-2) = x(t) - 2 \cos \lambda x(t-1) + x(t-2) \quad (4.29)$$

is also satisfied. The sequence $y(t)$ therefore satisfies an ARMA(2,2) equation. Let us restate this equation slightly to make it more useful for estimation. Suppose that

$$y(t) - \beta y(t-1) + y(t-2) = x(t) - \alpha x(t-1) + x(t-2) \quad (4.30)$$

and we impose the constraint that $\beta = \alpha$. If α is known and certain statistical requirements are met, then β can be estimated by Gaussian maximum likelihood. The result is

$$\beta_j = \alpha_j + \frac{\sum_{t=0}^{T-1} y(t)\zeta(t-1)}{\sum_{t=0}^{T-1} \zeta^2(t-1)} \quad (4.31)$$

If the value of α is correct, then α should equal β . If they are not equal, The estimate of β can be used as a new estimate of α and the procedure repeated. The procedure becomes an iterative contraction mapping, with β converging to the true value $\beta = 2 \cos \lambda_0$. In practice, the correction term in Eqn. 4.31 is multiplied by 2 to speed the convergence. The resulting estimator has many desirable properties. It is both statistically and computationally efficient. It achieves the Cramer-Rao lower bound on uncertainty. The estimator converges with inaccurate initial estimates. If the initial estimate is the maximum term of the FFT, the estimator converges after 2 iterations. The algorithm is as follows[46]

1. Obtain an initial estimate of λ from the maximum term of the FFT of the signal data.

2. Put $\alpha_1 = 2 \cos \hat{\lambda}_1$, where $\hat{\lambda}_1$ is the initial estimate of the true value λ_0 .
3. for $j > 1$, put $\zeta(t) = y(t) + \alpha_j \zeta(t-1) - \zeta(t-2)$, $t = 0 \dots, T-1$ where $\zeta(t) = 0, t \leq 0$
4. Put

$$\beta_j = \alpha_j + 2 \frac{\sum_{t=0}^{T-1} y(t) \zeta(t-1)}{\sum_{t=0}^{T-1} \zeta^2(t-1)}$$

5. if $|\beta_j - \alpha_j|$ is small enough, put $\hat{\lambda} = \arccos \beta_j / 2$. Otherwise, let $\alpha_{j+1} = \beta_j$ and go to step 2.

The estimate of λ can be further refined by using it as an input to a least squares regression on the data.

Multiple frequencies can also be estimated with the modified ARMA technique. The procedure for multiple frequency estimation is as follows[46]

1. Estimate frequency with the strongest Fourier coefficient using the modified ARMA technique
2. Remove the estimated frequency by regression on the estimated data
3. Estimate the next strongest frequency using the residual of the previous regression
4. Repeat until all expected frequencies have been estimated
5. If desired, use the estimated frequencies as starting values in a regression on the original data

In order for the final regression to yield the desired results, the number of frequencies must be known accurately. If a regression is attempted with an incorrect number of sinusoids, the final regression may converge to incorrect values.

Several improvements to the basic ARMA method have been developed. A different corrector for β in step 4 leads to faster convergence[47]. The introduction of an uncertainty factor reduces sensitivity to initial estimate error.

Frequency estimation using the ARMA method yields minimum uncertainty estimates, allows for estimation of multiple frequencies, and does not require *a priori* knowledge of the frequency to give correct results. For these reasons, the ARMA method developed by Quinn and Fernandez was chosen for use in the control system for this project.

4.4 Method Verification, Uncertainty, and Operating Conditions

The ARMA frequency estimation gap sensing scheme needs to be verified for precision, bias, and uncertainty. Operating conditions of wavelength range, number of interpolation points, number of samples to average, and any other filtering necessary also need to be determined.

4.4.1 Method Verification

The ARMA method was compared to the ellipsometer to confirm its suitability. The ellipsometer can not measure the gap in a pillar machine, so the comparison was made using films deposited on silicon wafers. Polystyrene films of various thicknesses were spin coated on silicon wafers. A spin coated film should be uniform to within a few nanometers, but it is not perfectly uniform. Therefore, five spots were marked on each wafer. The film thickness was measured at each point with the reflectance sensor and ARMA analysis, then with the ellipsometer, and again with the reflectance sensor. The repeated reflectance measurement was done to determine if thermal expansion or residual solvent evaporation contributed to disagreement between the methods. The results of the comparison are shown in figure 4.10. The root mean square difference between the ellipsometer and the gap sensor is 1.7nm.

4.4.1.1 Uncertainty

The uncertainty of the gap estimator is a difficult question. The traditional method of defining uncertainty[48] does not really apply. Traditionally, all of the error sources are compiled into an error budget and the sensitivity of the measurement to each error is determined. The error sources are then added according to the appropriate statistical procedures. Gap measurement is a fitting problem and the sensitivity of the final measurement to uncertainty in any data point is difficult to determine. The fitting problem in gap sensing is related to the fitting problems of computational metrology. The uncertainty

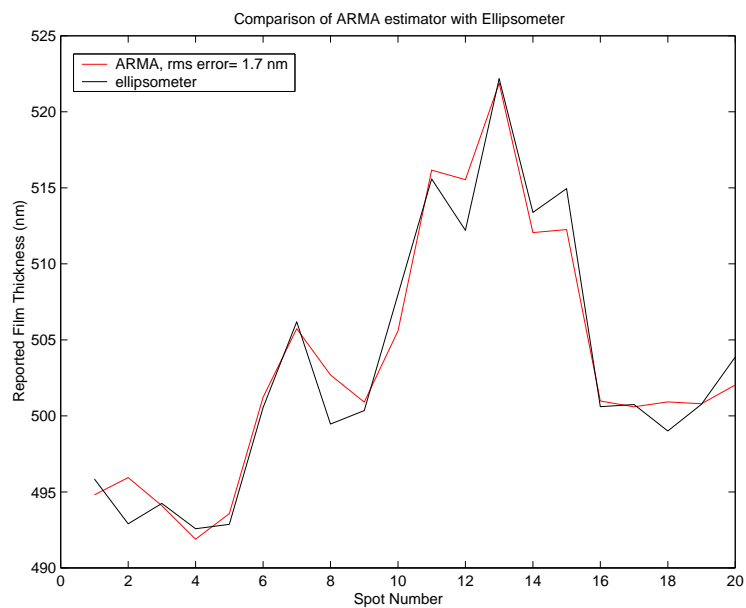


Figure 4.10: Comparison of polystyrene film measurements made with ellipsometry and with reflectance spectroscopy with ARMA analysis

of fitting methods is ill defined at present. It is reasonable to compare the final gap measurement with a known good measurement. Film measurements made with spectral ellipsometry have uncertainties in the range of fractions of angstroms, so ellipsometer measurements can be taken as the "true" film thickness. The uncertainty of the gap sensor can be taken from the comparison made previously. The standard deviation of the error is 1.7nm, so the standard uncertainty is twice that, or $\pm 3.5\text{nm}$.

If the Cauchy coefficients of the film are well known, as they are in the polystyrene comparison, the uncertainty meets the minimum of $\pm 3.5\text{nm}$. As the uncertainty in the Cauchy coefficients increases, so does the uncertainty in the gap measurement. If the Cauchy coefficients are poorly known, the uncertainty increases to $\pm 30\text{nm}$. If the Cauchy coefficients change, as they do when a photocurable material is cured, the change of Cauchy coefficients needs to be modeled or the uncertainty will increase. The coefficients of air are well known, so the uncertainty of air gap measurements is $\pm 3.5\text{nm}$. Comparison of the film measurements shows that the sensor is accurate for thin films, but says nothing about thicker air films. Confirmation of the method's suitability for thicker air films was made with a scanning electron microscope. Pillars were formed on the Active Gap Tool and their height measured on the SEM. The pillar height and measured gap agreed to within about the same uncertainty as thin film measurements, so the 3.5nm uncertainty appears to hold true. Pillar height measurement with the SEM is difficult to compare with the gap sensor as rigorously as the ellipsometer, so the uncertainty determination is

less rigorous. One final word about the gap measurement uncertainty. Since the gap measurement is a frequency fit of spectral data, the uncertainty is absolute and not relative. The uncertainty is $\pm 3.5\text{nm}$, regardless of whether the gap thickness is 500nm or $50\mu\text{m}$.

4.4.2 Operating conditions

There are several operating parameters in the gap sensing algorithm that can be adjusted depending on conditions. The parameters are the wavelength range analyzed, the number of interpolation samples, and the number of spectra to average. These parameters affect the range of gaps that can be sensed and the stability of the measurements.

The wavelength range and number of interpolation samples determine the largest gap that can be sensed. Adjusting the wavelength range can also be used to exclude noisy wavelengths. The maximum sensed gap is determined by the Shannon sampling theorem. The wavelength (we actually use wavenumber in the analysis) range and number of interpolation points determine an effective sampling frequency in nm. Since the "time" axis is wavenumber, the frequency unit is nm. The maximum sensed gap is half of the sampling frequency. For a wavelength range of 500 to 800nm and 512 sampling points, the maximum air gap that can be sensed is $169\mu\text{m}$. The signal aliases if the gap is larger. The maximum sensed gap for several wavelength ranges is shown in table 4.1.

The minimum gap that can be measured is determined by the noise and the wavelength range. Between a quarter to a half period is necessary for

Low Wavelength (nm)	High Wavelength (nm)	Maximum Gap (μm)
400	900	91.6
400	800	101.8
500	900	143.157
500	800	169.7

Table 4.1: Wavelength range and maximum measurable gap with 512 interpolation samples

frequency measurement methods to work reliably. A larger wavelength range captures more of the signal, and therefore allows smaller gaps to be measured. In practice, when approaching the operating position, a higher maximum gap is desirable. When at the operating position, a larger wavelength range allows smaller gaps to be measured. When the gap is large, the wavelength ranges between 400 and 450nm and from 800 to 900 nm are noisy. When the gap decreases below $10\mu\text{m}$, the noise dies down. When the gap is large, the best wavelength range to use is 500nm to 800nm to avoid the noisy region and to be able to track gap to $170\mu\text{m}$. When approaching the operating position, switching to the range from 400nm to 800nm allows sensing gaps down to about 400nm.

Sometimes when measuring the air gap between a wafer with film and the template, using the film reference does not remove the film signal. This often happens if the film is unstable. In these cases, the film signal can interfere with the measurement of the air gap and therefore interfere with machine control. The film signal can be removed by FFT filtering. To filter the film signal, take the FFT that primes the ARMA filter and set the value in the appropriate frequency bins to 0. The film thickness is usually much less than

$1\mu\text{m}$, so usually the first two frequency bins need to be set to 0. Use the maximum value of the filtered spectrum to prime the ARMA filter. Then take the IFFT of the resulting spectrum and feed the result to the filter. The air gap is then measurable. As the machine approaches the operating position, the air gap interference signal gains strength and eventually becomes strong enough to be accurately measured without filtering.

The number of spectra averaged affects the signal processing speed and the effect of noise. If the signal is noisy, averaging 5 spectra will remove the noise, but increase the computational time. The noise is generally low frequency, so averaging becomes important when measuring very small gaps. When the gap is thicker than $1\mu\text{m}$, averaging is unnecessary

4.4.3 Sample Rate

The gap measurement sample rate determines the machine control rate. On the current computer, an 800MHz Pentium III, collecting 3 spectra takes 33ms and analyzing 3 gaps takes 90ms. Once all the system overhead is added, a sample rate of 5Hz is possible. New spectrometers promise sample rates of 1kHz and a new dual processor, dual core 2.4GHz computer can complete the analysis in less than 10ms. Once other system overhead is added, sample rates approaching 100Hz should be possible. Software optimization could increase this rate further.

4.5 Conclusion

Reflectance spectroscopy with ARMA analysis accurately measures film thicknesses from around 500nm to more than $150\mu\text{m}$. The analysis requires no *a priori* knowledge of the gap, only knowledge of the Cauchy coefficients of the film material. The measurement system requires access for a vertical reflection probe above the film to be measured. The computer currently in use can measure film and air gap thickness at a rate of 5 Hz. New spectrometers and computers can increase the sample rate towards 100Hz. Reflectance spectroscopy with ARMA analysis provides gap measurement with minimal hardware requirements and allows for flexibility in the design of the pillar machine.

Chapter 5

Preliminary Results

Early pillar formation experiments were done with the Active Gap Tool, a tool developed for Step and Flash Imprint Lithography research and the Nano-Align 3, a piezoelectrically actuated tip/tilt/Z stage from Mad City Labs, Inc. [49] developed for microscope slide positioning. Experience gained from these tools led to the development of the design requirements for the proposed pillar tool.

5.1 Active Gap Tool

The Active Gap Tool is a 3-RPS parallel manipulator developed for Step and Flash Imprint Lithography. A labeled CAD drawing of the AGT is shown in figure 5.1 and figure 5.2 is a picture of the tool. The manipulator is constructed at the 'special configuration' of $\theta_0 = \pi/2$. The mechanism is constructed such that the fixed base is at the top of the machine with the moving platform hanging underneath. Wafer loading is accomplished using an air solenoid actuated wafer stage. Ordinary pin and spherical joints have issues of backlash and stiction, so flexure joints are used instead. The pin joints are simple semicircular cut flexures. In place of the spherical joints, flexure universal

joints designed for decoupling torques from piezoelectric actuators are used. The compliance of the attachment screws supplies the additional required rotation freedom. One other consequence of constructing the machine at the 'special configuration' of $\theta_0 = \pi/2$ is that the spherical joints can be replaced with universal joints. As the mechanism is actuated from perfectly parallel, the extra freedom of the spherical joint becomes important. The Active Gap Tool is always actuated close to the ideal position, so the compliance of the screw where the universal joint meets the moving platform is enough to allow the flexure u-joints to function as flexure spherical joints in this application. The mechanism is actuated by DC micrometer motors. The motors have an advertised minimum actuation of 100nm. A piezoelectric load cell measures the force applied to each leg.

Stiffness in the $X - Y$ plane is enhanced with a flexure ring, shown in Figure 5.3. The flexure ring is attached to the fixed structure at three points and to the moving platform at the other three points. The result is the same three degrees of freedom as the 3-RPS manipulator with high stiffness in the $X - Y$ plane. The flexure ring also supplies a vertical force. When actuated such that the process position is below the neutral position, the flexure ring preloads the mechanism links and supplies a separation force. Preload on the links is useful if piezoelectric actuators are added to the DC micrometers. Preload increases the piezoelectric actuators ability to pull without tensile failure.

The pillar formation process requires two parallel surfaces to act as

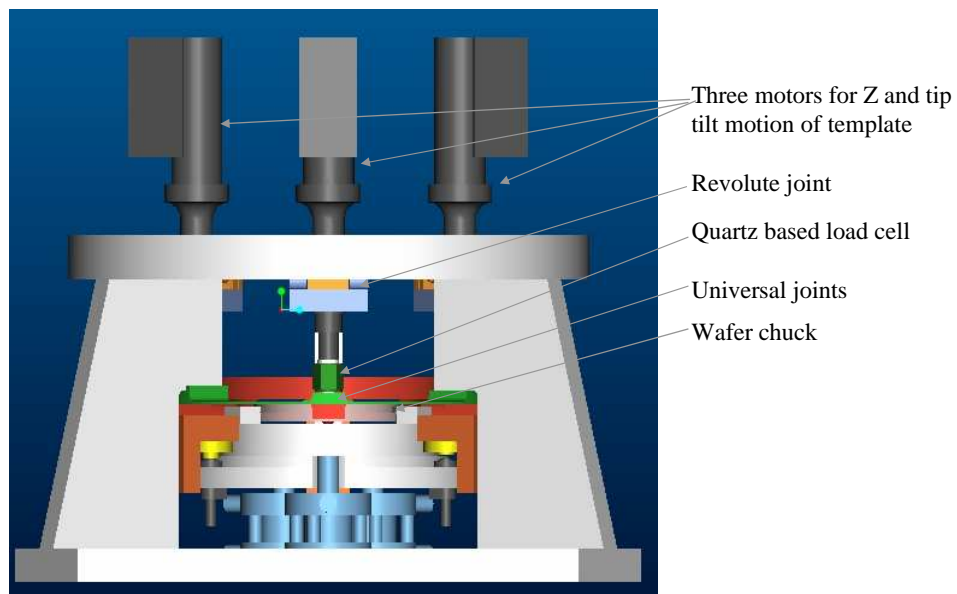


Figure 5.1: CAD image of the Active Gap Tool

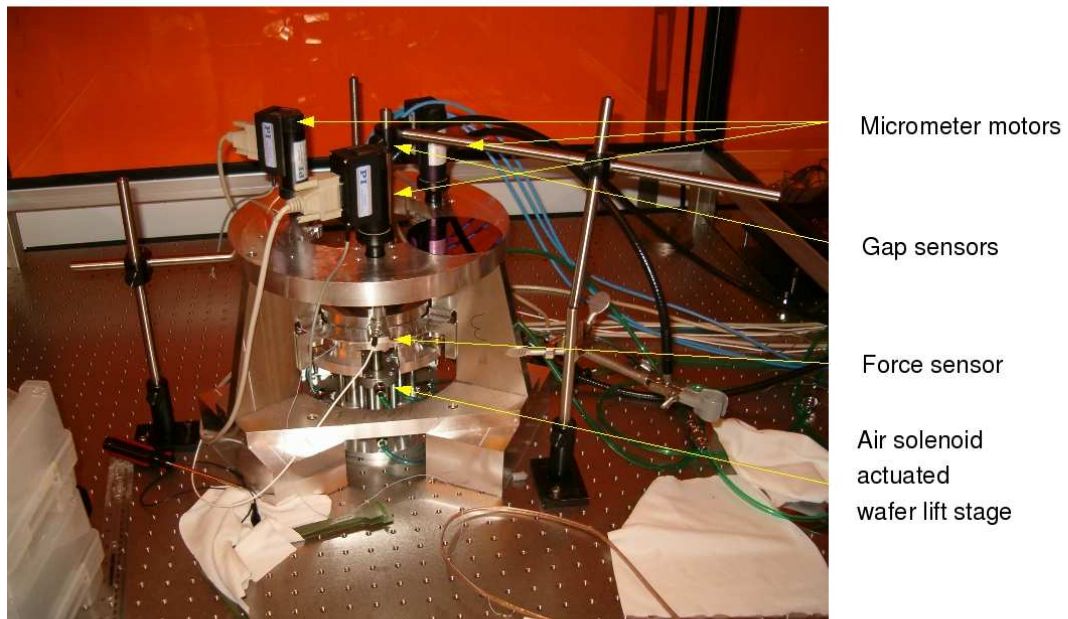


Figure 5.2: Photograph of the Active Gap Tool

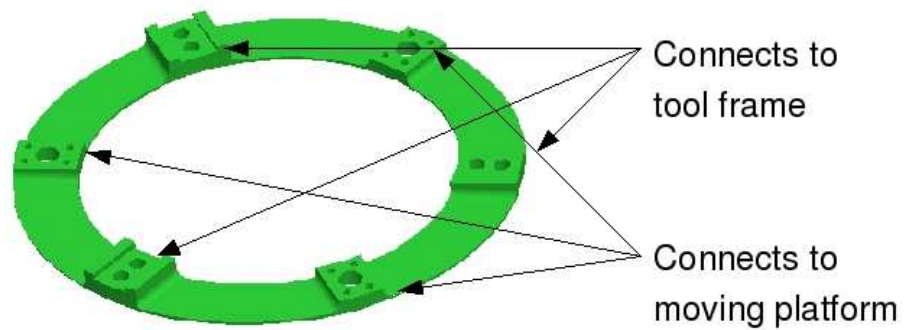


Figure 5.3: Flexure ring from the Active Gap Tool

electrodes. In the Active Gap tool, the bottom electrode, which holds the thin film initially, is a doped silicon wafer. The upper electrode is a template formed from a 1/4 inch thick fused silica mask blank. The template is the same 65mm square format that is used in imprint lithography. The active area used for the process was a 1.1 inch square. The mask blank is coated with a thin layer of indium tin oxide to provide electrical conductivity. The template is transparent and allows for UV illumination and optical gap sensing. The template is held in place by a vacuum chuck on the moving platform.

The Active Gap tool was designed for use in imprint lithography research. Imprint lithography requires keeping two surfaces parallel, so the process requires the same degrees of freedom as pillar formation. However, imprint lithography requires low stiffness so the two surfaces can self align when they contact. Pillar formation requires high stiffness to keep the surfaces apart while the electrostatic force is pulling them together. The Active Gap Tool, though not ideal, was used in the early pillar formation experiments.

5.2 Nano-Align 3

Experiments were also conducted using the Nano-Align 3, a commercially available nanopositioner from Mad City Labs. The Nano-Align has the same kinematics as the active gap tool, but has a much finer resolution and smaller range of motion. It was designed for positioning microscope slides. The experiments conducted on this machines used glass slides coated with a thin layer of chrome and rectangular pieces of silicon wafers. The glass slide

was positioned using the supplied slide holder. The substrate was positioned using a custom slide holder designed at UT that was mounted on a prism positioner. The prism positioner was used to get the two surfaces close to parallel and then the nanopositioner was used to make them more parallel. There were several drawbacks to this setup. The prism holder was not kinematically constrained in relation to the positioner, so repeatability was an issue. We could not get the two surfaces parallel, remove the piece of silicon to apply the thiol-ene solution, and reassemble the stack and hope that they would still be parallel. The nano-align was also more compliant than the Active Gap Tool, with a stiffness of $1 \text{ N}/\mu\text{m}$.

5.3 Materials and Experimental results

5.3.1 Photocurable Acrylates

The early attempts at photocurable electrical lithography used photocurable, acrylate terminated silicones as the pillar material. Pillars were formed on the Active Gap Tool. The results are discussed in the following section.

5.3.1.1 Experimental Results

A solution of low viscosity silicones with acrylate terminal groups and photoinitiators were spun on silicon wafers. The material formulation is not part of this thesis. Materials were obtained from Prof. Willson's chemical engineering group. A quartz template coated with Indium Tin Oxide, a con-

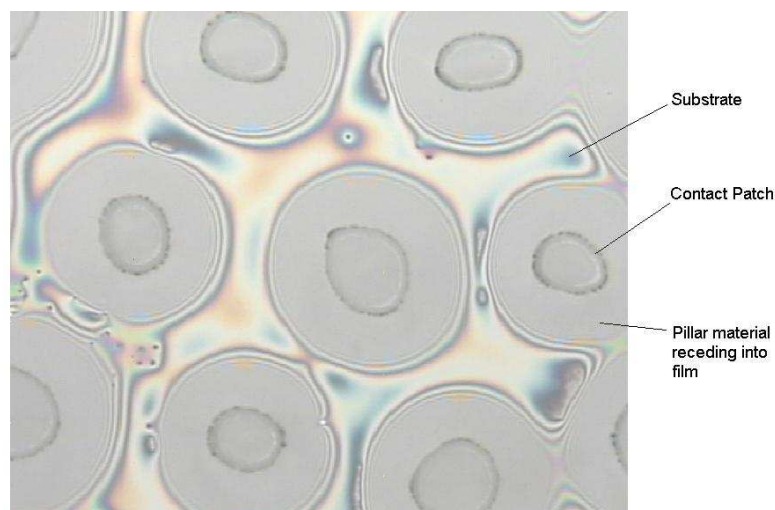


Figure 5.4: Pillar residue from uncured silicone pillars. The contact patches are where the pillars contacted the template electrode. The contact patches are approximately $10\mu\text{m}$ in diameter.

ductive substance that is transparent to ultraviolet light, was brought into orientation alignment with the silicon wafer. A voltage was applied between the template and the wafer. Pillars formed and were exposed to ultraviolet light. Pillars formed, but the acrylate reaction is oxygen inhibited, so the pillars did not cure. They formed, but quickly subsided into the film. The pillar residue is shown in figure 5.4. This demonstrated that pillars could be formed without heat. The choice of film was less than ideal because the acrylate polymerization reaction is inhibited by oxygen and the silicones did not spin into a smooth, thin film. Work has been ongoing to find materials that do not have those disadvantages.

5.3.2 New Polymer Formulation

Dr. Willson's group at the University of Texas has developed a chemical for pillar formation that is an improvement over the silicones first used. The chemical group is called thiol-enes.

The thiol-ene is formed from two monomers, a thiol and an alkene. The thiol is a branched organic compound with thiol ($-SH$) groups at the end of each branch. The alkene is a branched organic compound with each branch ending in a carbon-carbon double bond. The number and composition of the branches affect the physical properties of the cured polymer. The mixture polymerizes with a thiol linking with an alkene which links with a thiol, etc. The mixture currently in use has three thiol or four alkene groups on each monomer molecule, leading to a highly crosslinked polymer. The thiol-ene mixture spins uniformly and the thiol-ene reaction is not inhibited by oxygen. Early experiments showed that the thiol-ene mixture will form pillars.

5.3.2.1 Thiol-ene Results

Experiments were done using glass microscope slides and paper clips to verify that pillars would form using this material. The thiol-ene formulation was then used with the Nano Align 3 to attempt to form pillars over large areas.

Using the Nano-Align proved to be a great challenge. If a corner or an edge of the microscope slide contacted, the slide would bow and the substrate would move, hampering repeatability. If the slide touched the substrate, sur-

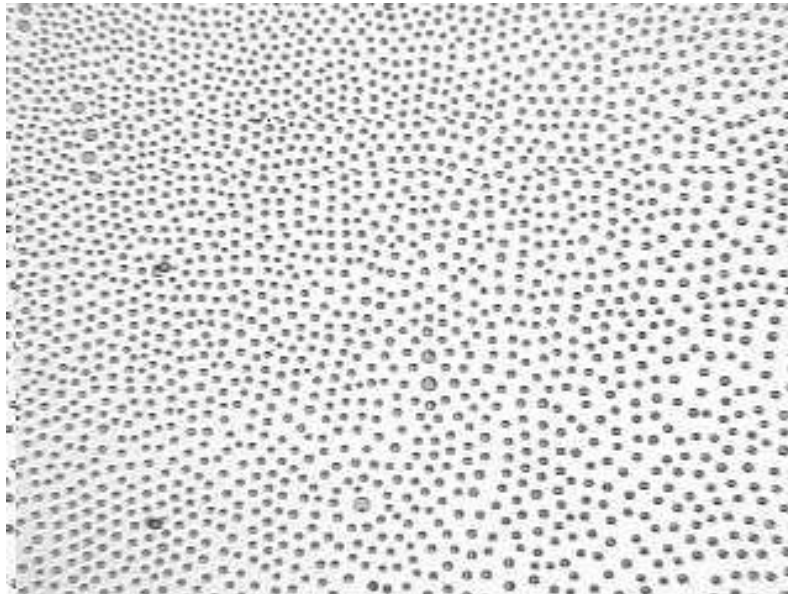


Figure 5.5: Pillars formed on Nano-Align, showing regions of order. The pillars are approximately $10\ \mu\text{m}$ in diameter.

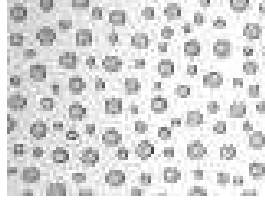


Figure 5.6: Pillars formed on Nano-Align, showing bimodal pattern. The large pillars are about $10\text{ }\mu\text{m}$ diameter and the smaller pillars are $4\text{ }\mu\text{m}$.

face forces would pull the two together, closing the air gap and disturbing the film. Despite these difficulties, a few trials gave good results. Some of the results raise questions about the curing process. Some pillars that were exposed with UV light were not cured while others that were not exposed seemed to cure. The reason for this was unclear. Perhaps the chrome layer was too thick to allow exposure on the sample that did not cure and maybe an electrical current can somehow start the polymerization. One trial did cure and gave interesting results. The initial air gap was five microns, and despite contact in some regions of the active area, large regions of pillars did form. The pillars showed local hexagonal symmetry with uniform size in some regions. In other regions, large pillars of varying sizes were formed. In another region, an apparently bimodal pillar pattern formed. These experiments show that photocurable pillars can be formed over large areas.

5.4 Return to the Active Gap Tool

The Nano-Align proved unsatisfactory, so the Active Gap Tool was used for subsequent tests to determine the requirements for a pillar formation ma-

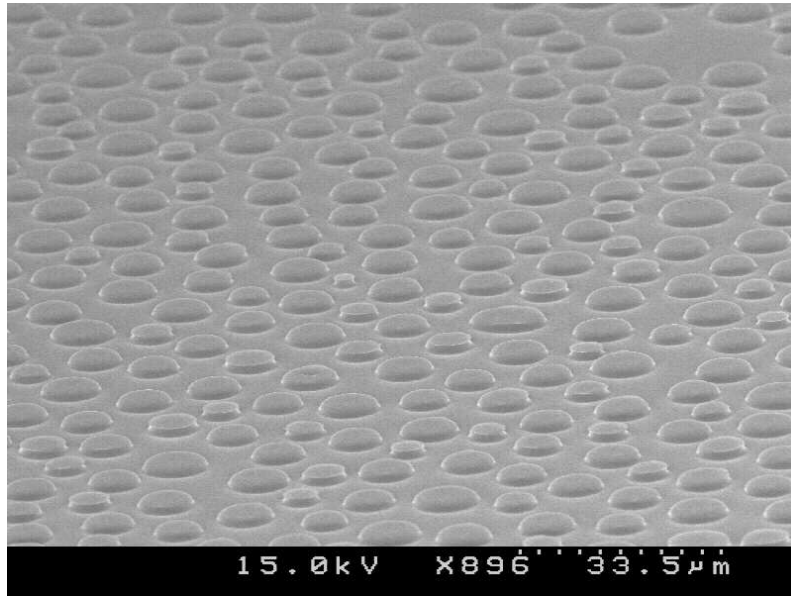


Figure 5.7: Pillars formed on Nano-Align, showing regions of order

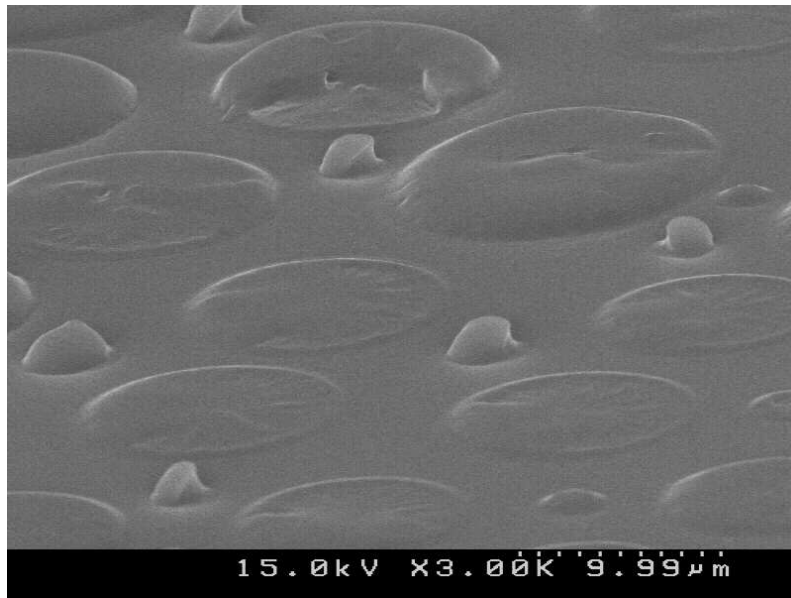


Figure 5.8: Pillars formed on Nano-Align, showing bimodal pattern

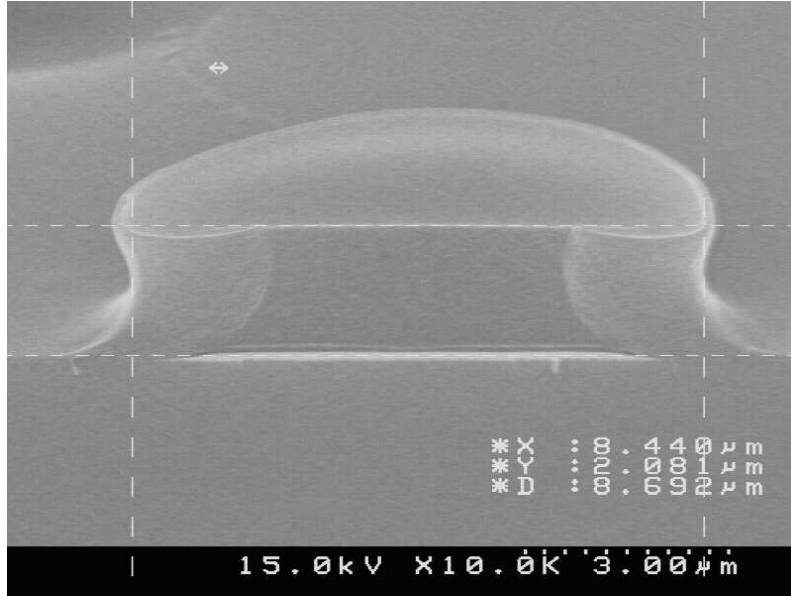


Figure 5.9: Cross section of pillar formed on Nano-Align

chine. Experiments on the Active Gap Tool allowed for investigation of pillar forming materials, understanding of the applied electrical force, and determining the effect of machine stiffness on the process. Research into materials is not covered in this thesis. Understanding of the electrical force and machine stiffness were instrumental in designing the successor to the Active Gap Tool.

5.4.1 Electrical Force

Pillar formation requires two parallel conducting surfaces. The two surfaces form a parallel plate capacitor. Applying a voltage across the plates creates an electric field between the surfaces. This electric field generates a force that tries to pull the two surfaces together. The magnitude of this force

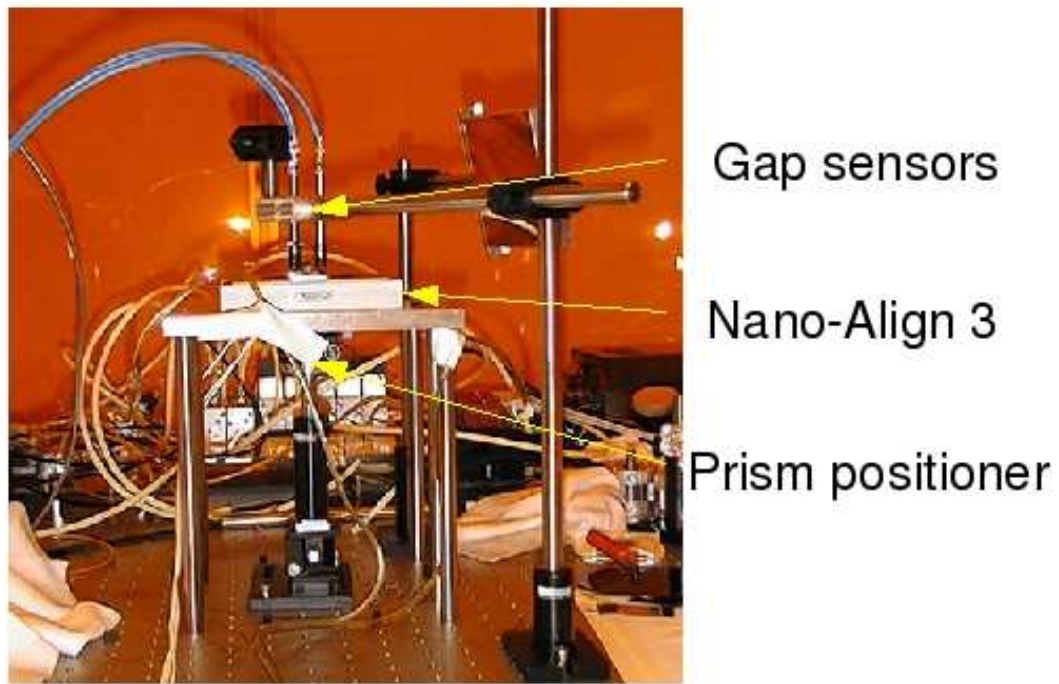


Figure 5.10: Side view of the Nano-Align setup

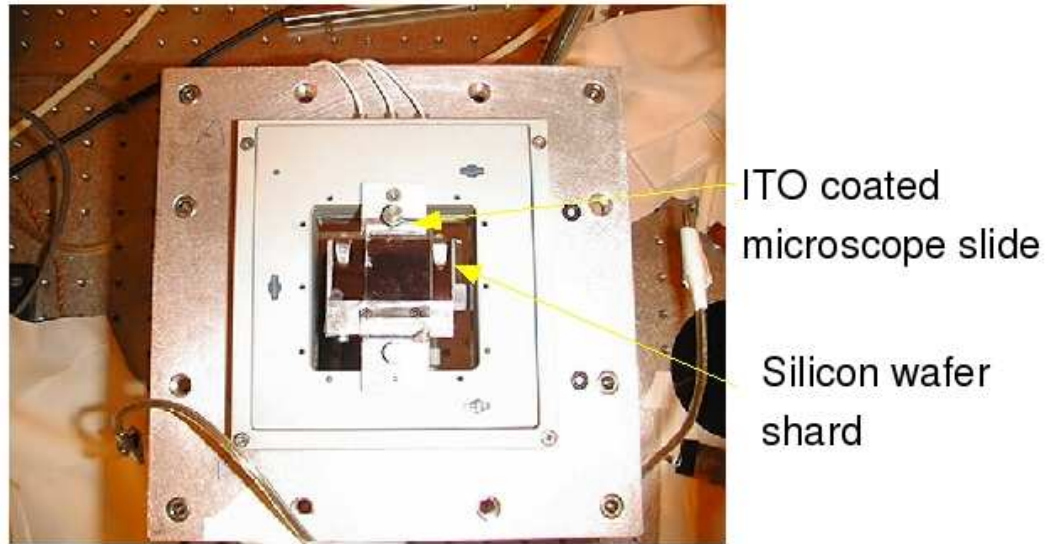


Figure 5.11: Top view of the Nano-Align setup, showing the crossed slides and substrate holder

depends on the geometry of the template and the uniformity of the electric field. A cross section of the template is shown in figure 5.13. The process active area is in the center of the template. The surrounding area is etched with a buffered oxide wet etch to a depth from 5-15 μm . The edge area is called the mesa. The mesa etch has several purposes. If the template had no mesa, the template corner would contact the wafer underneath before the system had a chance to make the surfaces parallel. This results in high contact forces and disturbs the film on the wafer. The mesa etch also lowers the electrical field in the inactive area, lowering the total attractive force. The rounded edge of the template connects the ITO layer on the active surface to the side, where a wire is attached to the template for voltage supply. A template with wire

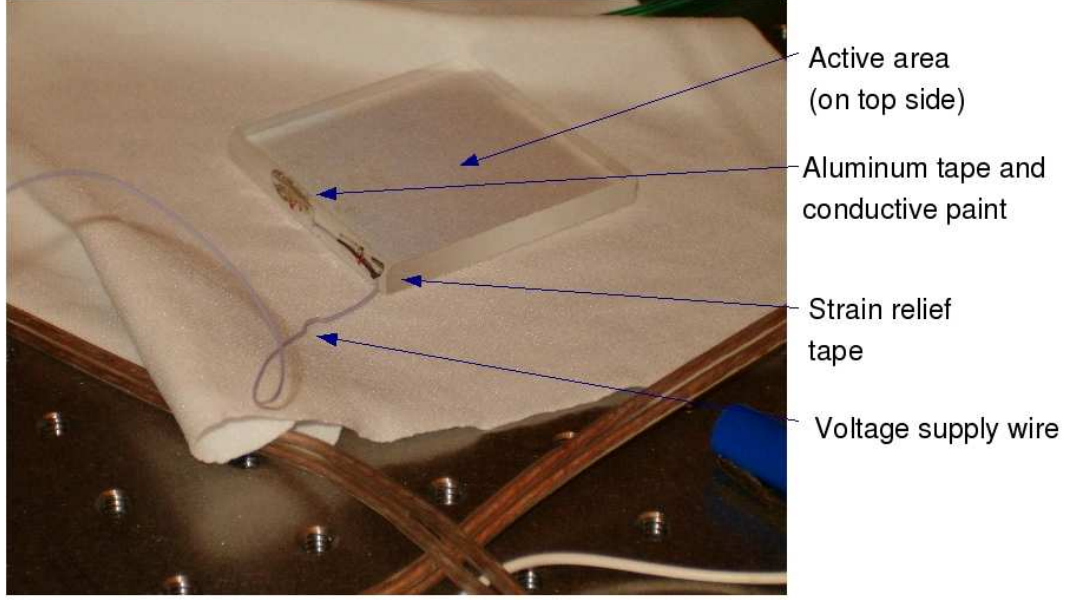


Figure 5.12: Template with wire attached

attached is shown in figure 5.12.

The electrical force between the template and the wafer is an electrostatic force. The ideal electrostatic force between two parallel plates is given by[50]

$$F = \frac{AV^2\epsilon}{2d^2} \quad (5.1)$$

where A is the area of the plates, V is the applied voltage, ϵ is the permittivity of the substance between the plates, and D is the gap between the two plates. Equation 5.1 assumes that the electric field between the two plates is uniform and perpendicular to the two plates. The geometry of the pillar process has a narrow gap at the active area, a wider gap on the mesa, and a region on

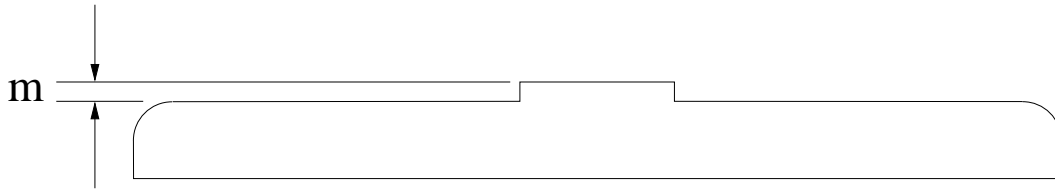


Figure 5.13: Side view of template, showing mesa height and edge rounding

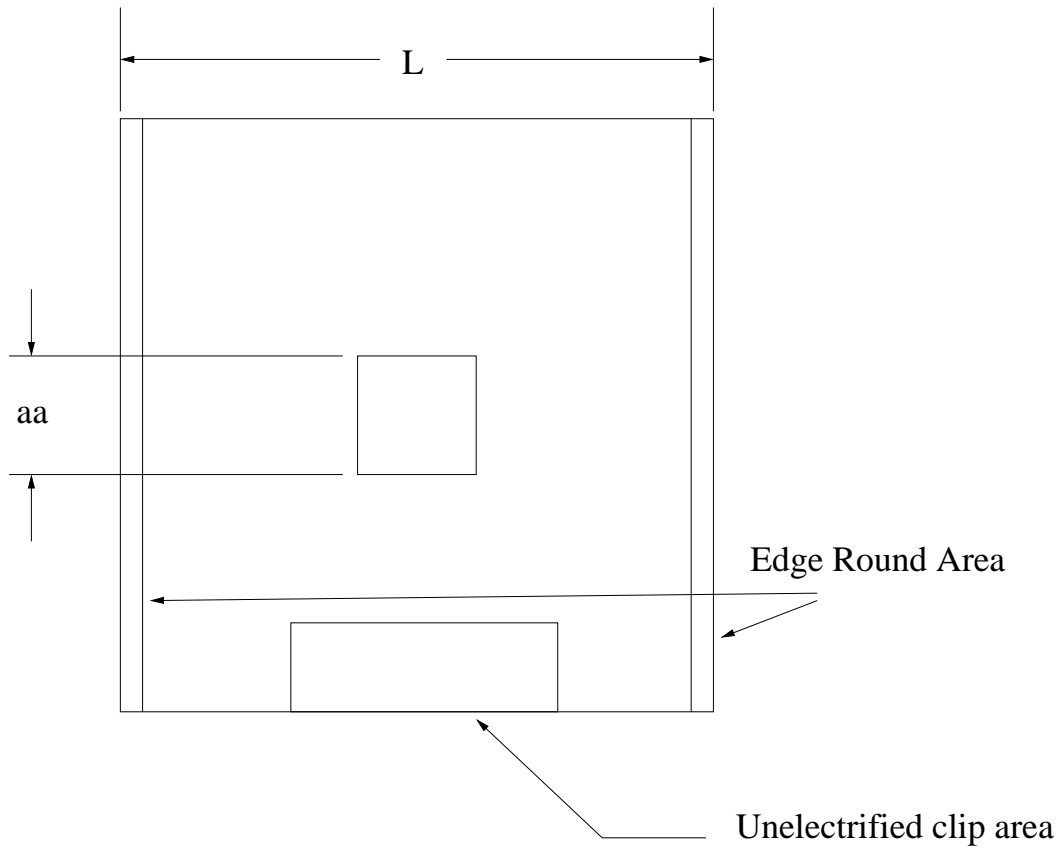


Figure 5.14: Template face, showing dimensions and unelectrified areas

the edge where the gap widens rapidly. When the ITO layer is added to the template, it is held in place by a clip. The clip results in an area that is not conductive. To model the electrostatic force, each of these areas needs to be accounted for. The template is conductive everywhere, so the voltage is the same everywhere. The force from the active area is

$$F = \frac{aa^2V^2\epsilon}{2g^2} \quad (5.2)$$

where g is the gap between the wafer and template and aa is the active area side length. The force arising from the inactive area is

$$F = \frac{(L^2 - aa^2 - A_e) V^2 \epsilon}{2(g + m)^2} \quad (5.3)$$

where L is the overall template side length, A_e is the unelectrified and edge round area, and m is the mesa height. The total force is the sum of the active and inactive area forces

$$F = \frac{aa^2V^2\epsilon}{2g^2} + \frac{(L^2 - aa^2 - A_e) V^2 \epsilon}{2(g + m)^2} \quad (5.4)$$

Experiments were conducted on the Active Gap Tool measuring the electrical force generated at a variety of gaps and voltages. Representative results are shown in Figure 5.15. These experiments showed that the electrostatic model adequately explains the electrical force generated by the voltage between the template and wafer as long as the mesa height and unelectrified area are accurately known.

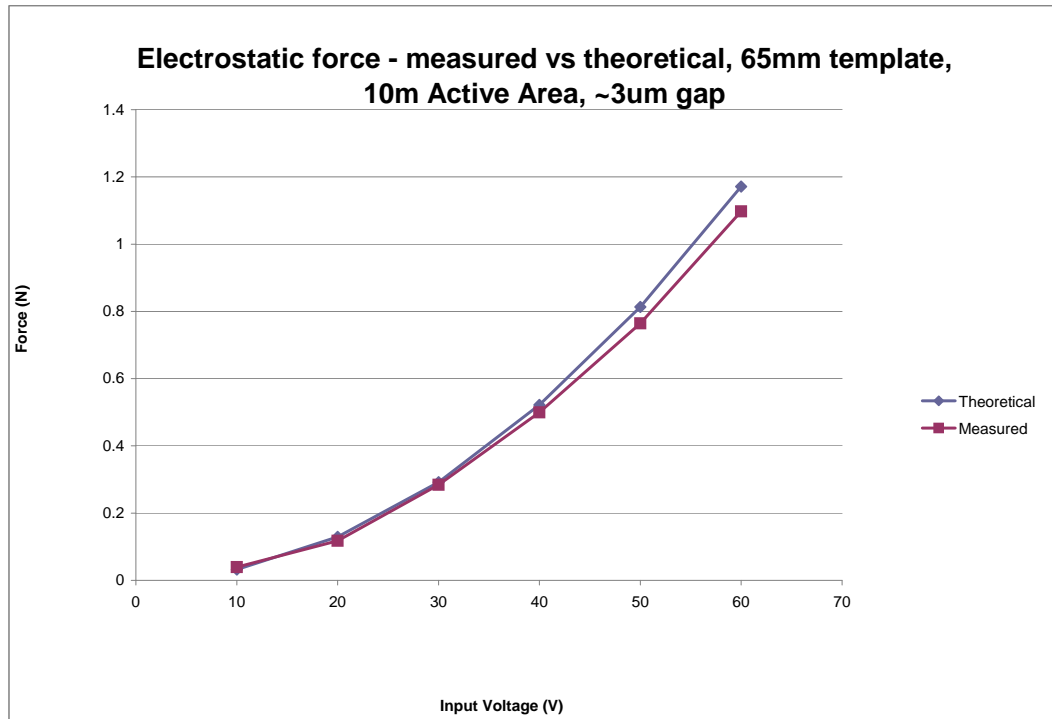


Figure 5.15: Electrical force generated between the wafer and template

5.4.2 Active Gap Tool Stiffness

Tool stiffness has a great impact on overall performance. When the electric field is applied, the template and wafer will move closer together. A stiffer tool will, of course, displace less. Data on the displacement under load were collected as part of the electrical force experiments. A representative force/displacement graph is shown in figure 5.16. The experiments show that the Active Gap Tool has a stiffness of $17 \text{ N}/\mu\text{m}$.

5.5 Conclusion

Early experiments on the Active Gap Tool and the Nano Align 3 showed that pillars can be formed over large areas with low viscosity films and cured with UV light. The mechanism designed for no load positioning proved unsuitable for the task due to its low stiffness. The active gap tool was better, but it was also too compliant to form pillars at small gaps. The results of the early experiments led to the development of a set of requirements for a dedicated pillar machine.

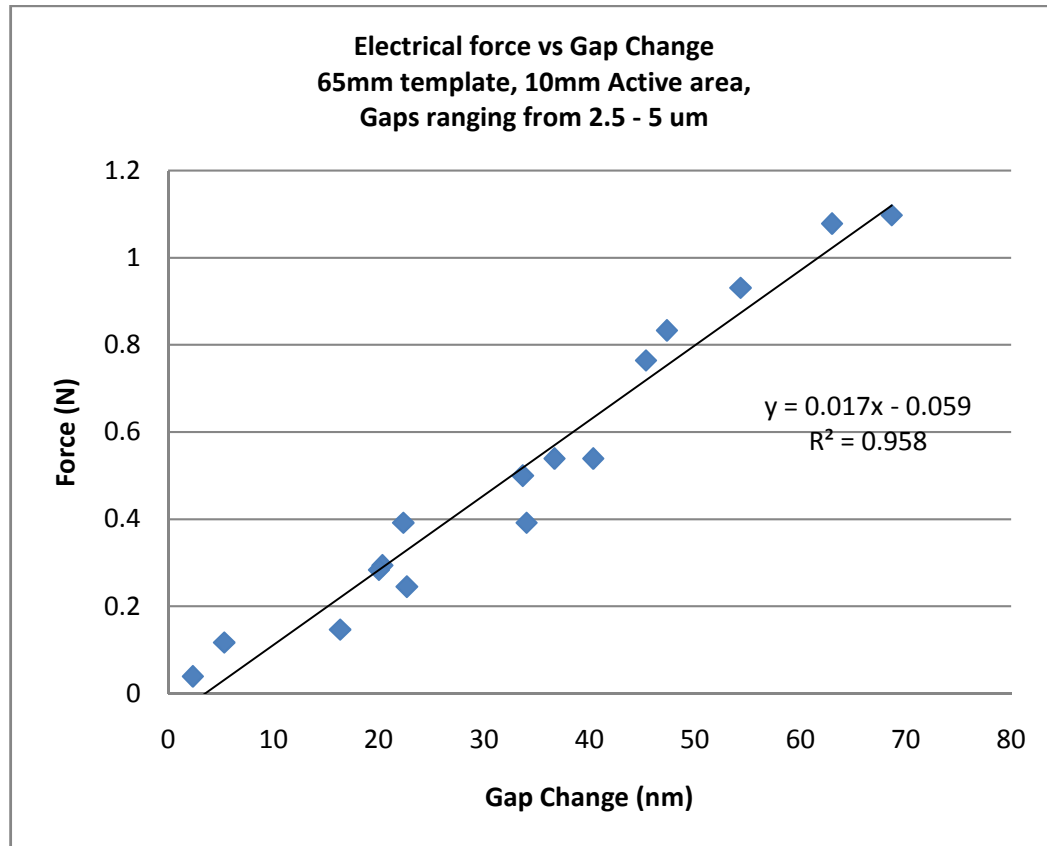


Figure 5.16: Active Gap Tool stiffness as determined by electrical force experiments

Chapter 6

Pillar Formation Machine Requirements

Experience with the Active Gap Tool and the Nano-Align 3 led to development of a set of design requirements for a dedicated pillar making machine. The proposed machine is called the Pillar Formation Tool (PFT). The PFT needs to hold the electrodes of the pillar formation process in the proper position and orientation while the electric field is applied. One of the electrodes is a silicon wafer and the other is a 65mm square template from imprint lithography. The machine must hold the template and wafer $200\mu\text{m}$ apart to capture reference signals for gap sensing and then decrease that gap to the process gaps of from 100nm to $5\mu\text{m}$. The machine must allow for silicon wafer loading and unloading, sense the gap and alignment between the template and wafer, correct the alignment, resist the electrical force between the template and wafer, and allow for UV curing of the formed pillars. The machine must also adjust for different wafer and template thicknesses. Optional features include access for a live video of the forming pillars and the ability to stretch the formed pillars. This chapter will examine each of the requirements in detail.

6.1 Physical Requirements

The first set of design requirements concern the basic physical layout necessary to form pillars. These requirements define the design space necessary for process success.

6.1.1 Wafer and Template

Two electrodes are necessary to form pillars. One electrode needs to be transparent to UV light. The process as instituted here uses a doped silicon wafer as one electrode and a 65mm x 65mm piece of 6025 fused silica mask blank for the other electrode. The mask blank, called the template, is coated with a conductive thin film, typically either a thin layer of chromium or Indium Tin Oxide. The machine must allow for loading and unloading of the wafers and templates without disturbing the monomer film or the cured pillars. The wafer and template must be electrically isolated from the rest of the structure. The wafer and template should be held without bending or otherwise distorting the active area where the pillars are formed.

The best solution for holding the wafer and template is to hold them with vacuum chucks. The design must allow for sufficient vacuum area to hold the wafer and template during the pillar formation process when the electrostatic force is pulling them together and when the template and wafer are separated after pillar formation. The chucks must also provide enough support to minimize wafer or template bowing. An electrostatic chuck is an option for holding the wafer, as long as the electrical isolation issue is addressed.

Accommodation must also be made for template electrification and for keeping the template corners from touching the template while the central active area is still misaligned. To electrify the template, the corner of the template is rounded with a glassware sander and the conductive film covers the active surface, rounded edge, and top half of the template side. A small gage wire with many fine strands is attached to the side of the template with a piece of aluminum tape. A second piece of tape provides strain relief. Electrical connection is improved with a silver bearing conductive paint designed for drawing circuit traces. Corner touching is prevented by etching the area outside the central active area 5 to $10\mu\text{m}$ from the active area. The etch creates a central ‘mesa’ above the surrounding inactive area. A picture of a completed template is shown in Figure 5.12 and a cross section view is shown in Figure 5.13. The mesa etch creates another sensing requirement, namely the mesa etch height. This can be sensed with a fourth sensor over the active area. Mesa height determination will be discussed in detail in the control system chapter.

Wafer loading requires that the template and wafer be separated enough for a wafer to be loaded and unloaded without disturbing the film. In practice, this means that at least .25 in. clearance between the template and wafer. If an automated arm of some sort is used, the necessary clearance may decrease. If the wafer is loaded manually, more clearance may be necessary.

6.1.2 Gap Sensing

Sensing the alignment and separation of the wafer and template is a necessary part of the pillar formation process. Three gap sensors can determine alignment. If the alignment sensors are in the recessed inactive area, then a fourth sensor is necessary for mesa height determination. The sensors used for white light reflective spectroscopy have a .25 in. diameter and the focusing lens housing has a .325 in. diameter. Spacing the sensors equally around a circle surrounding the active area significantly simplifies the orientation transformations. The sensor size and the requirement of access for UV illumination determine where the sensors can be placed. These requirements lead to a sensor location diameter of around 1 in. around the center of the active area. The mesa can be sensed with a fourth sensor over the active area. Mesa height determination will be discussed in detail in the control system chapter.

6.1.3 UV curing and video feed

UV light for photocuring can generally be supplied by either of two ways. The two options are to supply the light from a UV lamp with mirrors directing the light or with a light guide directing the light. Using mirrors to supply the light requires a path free of obstructions from the lamp to the active area. A light guide is a flexible tube filled with either UV transparent fluid or fiber optics. A light guide can supply UV illumination to a specific area without exposing surrounding areas. Use of a light guide requires a path for

guide routing and a mount to hold the light guide tip.

A useful video feed requires enough resolution to see the pillars, which are typically a few microns in diameter. The required resolution typically requires a small working distance and a large diameter microscope tube. The best solution identified so far uses a microscope objective tipped borescope. The borescope is 5mm in diameter and about one foot long. The borescope needs to be close and perpendicular to the backside of the template. The need for a gap sensor, UV feed, and borescope all in the active area is one of the most difficult configuration challenges. In practice, the three components are swapped as necessary.

6.2 Applied Load Derivation

When the template and wafer are oriented for the pillar process and a voltage is applied, an electrical force acts to pull the wafer and template together. As discussed earlier, this force is adequately explained by the electrostatic model. When a fluid film is in the gap, other forces may be present. These forces may include capillary forces, Van Der Waals forces and other small scale fluid forces. The main force is the electrical force and the electrical force is also the most easily predicted.

The electrostatic force is the same force derived in the previous chapter. The total force is given by equation 5.4

$$F = \frac{aa^2V^2\epsilon}{2g^2} + \frac{(L^2 - aa^2 - A_e) V^2\epsilon}{2(g + m)^2} \quad (6.1)$$

Since the electrostatic model adequately explains the measured attractive force, it can be used to predict the load at various operating conditions. The Active Gap Tool uses a 25mm active area, which generates too much force and has too much unsupported area subject to bending under the electrical load. The active area for the PFT was therefore reduced to a 10mm square. The maximum force occurs when the applied voltage creates the maximum possible electric field. In ideal conditions, air between two parallel plates experiences dielectric breakdown at a field strength of $80\text{V}/\mu\text{m}$. The template is flat, but the edge of the mesa has sharp corners which create non ideal conditions. In practice, arcing between the template and wafer starts at a field strength of $40\text{ V}/\mu\text{m}$ and becomes more likely as the field strength increases. The force generated by the template at maximum field changes as the gap changes. The force from the active area is constant because the electric field is constant. The force from the inactive area changes with gap because the field in the inactive area changes with gap. As the gap increases, the ratio of inactive area gap to active area gap decreases. Therefore, if the active area electric field is held constant as the gap is increased, the inactive area electric field increases, and therefore the total force increases. Figure 6.1 shows predicted electric force for both the maximum theoretical and maximum practical field strengths.

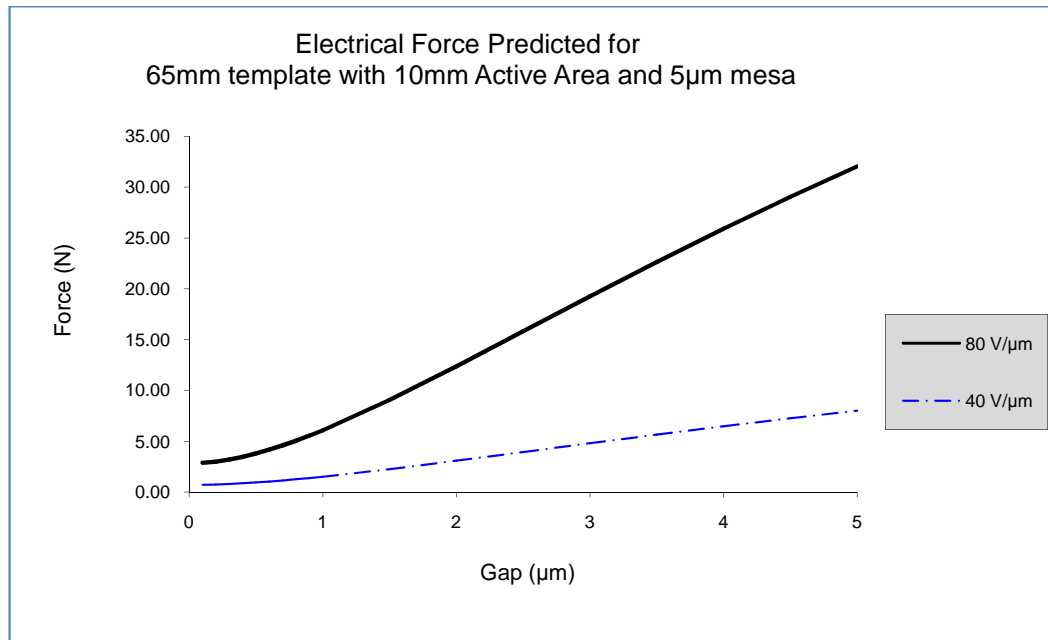


Figure 6.1: Predicted electrical force at maximum theoretical and maximum practical electric fields

6.3 Necessary Stiffness and Travel

The PFT must have enough travel to allow for the expected range of template and wafer variation and have enough stiffness to resist the applied loads.

6.3.1 Necessary Travel

The travel requirement for the PFT is composed of several parts. Different wafers and templates have different thicknesses and thickness variations. The two sides of a wafer will be flat, but not perfectly parallel. This non parallelism results in a wedge that will vary from wafer to wafer. The same is true for templates. The standard tolerance for total thickness variation is $\pm 25 \mu\text{m}$. There are also several nominal wafer thicknesses. Template thickness can vary by up to $100 \mu\text{m}$ from template to template. The other travel requirement comes from the need for a reference signal for the gap sensors. The gap sensors need a gap of $200 \mu\text{m}$ to capture a reference signal. The need to accommodate wafers and templates of different thicknesses and capture a gap reference signal leads to a total travel requirement of $400 \mu\text{m}$. Manual calibration screws can be used to adjust the machine for different wafer and template thicknesses, this reducing the needed active travel range. The $200 \mu\text{m}$ needed to capture a film reference, however, must be controlled by the actuators. Add a little extra to be safe and the required travel is $500 \mu\text{m}$.

6.3.2 Necessary Stiffness

The PFT must resist the applied forces, principally the electrostatic force, without allowing the gap between the template and wafer to change more than a specified amount. If the force is resisted passively, the machine must have a certain minimum stiffness. The minimum stiffness is determined by the allowable displacement and the applied force. An allowable displacement of 5% of the total gap was chosen as a design requirement. The stiffness required for 5% displacement at maximum electric field for different gaps is shown in Table 6.2. For a minimum gap of 100 nm, the required stiffness is 575 N/ μ m. Note that this is the total system stiffness, including both the wafer side of the machine and the template side. Each side must be stiffer than the required 575 N/ μ m for the total stiffness meet the requirement. If the required stiffness is divided evenly between the wafer and template sides of the machine, each side must have a stiffness of 1150 N/ μ m. For comparison, a piece of solid steel 1 in. tall and 0.5 in. in diameter has an axial stiffness of 1030 N/ μ m. Building a machine that has the required tip/tilt/Z degrees of freedom, 500 μ m of travel, and a total stiffness of over 1000 N/ μ m is not a trivial matter.

6.3.3 Stiffness Alternative

An alternative to building an impossibly stiff mechanism is to somehow reduce the needed stiffness. In principle, if the applied force is well understood, a compensation force can be applied. If the compensation force matches the applied force, the resulting displacement will be significantly smaller, and

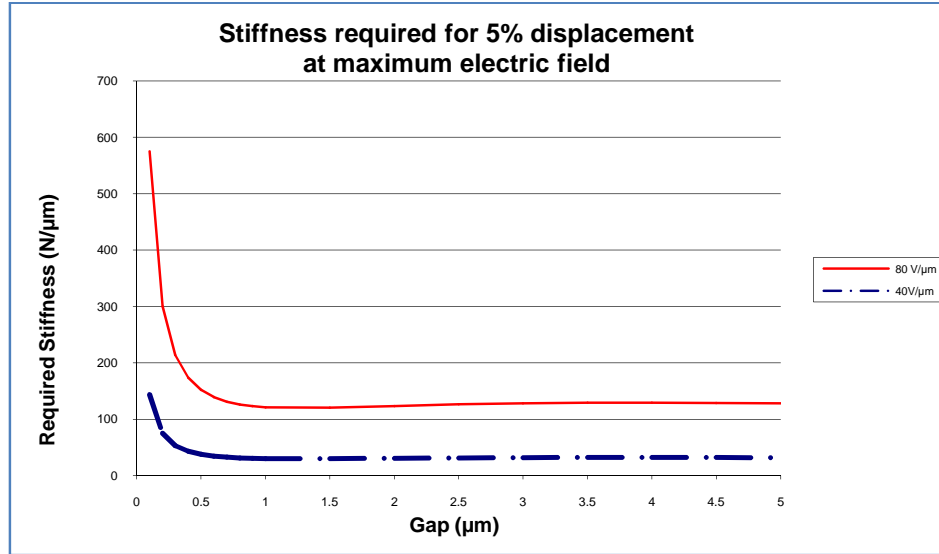


Figure 6.2: Stiffness required to allow 5% gap movement under maximum electric field

therefore the required stiffness will be significantly reduced. If the compensation is perfect, the manipulator stiffness doesn't really matter. Since the compensation will, of course, never be perfect, machine stiffness is still important, but the stiffness requirement is significantly lower.

Chapter 7

Pillar Formation Tool Design

Once the design requirements were defined, the design process began. First, designs with high stiffness were investigated. When high stiffness designs proved impractical, force compensation designs were investigated.

7.1 Stiff designs

A design with sufficiently high stiffness would have advantages over a force compensated design. A stiff machine would resist all forces, whether they were predictable or not. Any applied force would, however result in displacement.

7.1.1 Actuators

The actuators need to be stiff, have sufficient travel, and have enough resolution. How stiff, how much travel, and how much resolution are needed depends on the kinematics chosen. The kinematics most likely to be used are some form of symmetric three legged parallel robot. Therefore, each actuator leg must carry one third of the load and have one third of the total stiffness. The travel requirement for each actuator depends on the mechanical advantage

of the system. The resolution requirement depends likewise on the mechanical advantage. If the system resembles the 3-RPS parallel mechanism, the mechanical advantage will likely be close to or exactly one. The requirements used when evaluating actuators are therefore that the actuator leg must have a total stiffness of around $350 \text{ N}/\mu\text{m}$, travel of at least $200 \mu\text{m}$, and resolution of 1 nm .

There are two commonly used types of actuators with resolution in the nanometer range, voice coils and piezoelectric actuators. A voice coil consists of two parts, a coil and a permanent magnet. A current passed through the coil generates a force between the coil and the magnet. The two parts are not physically connected and the voice coil provides no kinematic constraint, so static stiffness, kinematic constraint, and power off support must be provided by other means. With proper feedback, a voice coil actuated mechanism can be capable of sub nanometer resolution with travel of several millimeters. .

A piezoelectric actuator contains a stack of sheets of a crystal that exhibits the piezoelectric effect. In a piezo electric crystal, an applied strain generates charge buildup on the surface that can be sensed to measure the force. If a charge is applied to a piezoelectric crystal, the crystal will expand, generating motion and force. A piezo actuator can also be capable of sub-nanometer precision with proper feedback. Feedback can be provided by sensors in the actuator itself or on the mechanism. Piezoelectric actuators can kinematically constrain the mechanism they are built in and have inherently high stiffness. However, piezoelectric actuators have small travel, typically a

few tens of microns. The travel can be increased by using a taller stack, but at the expense of losing axial stiffness, lateral stiffness and strength. Piezo actuators are fragile. The crystal cannot sustain tension, making a preloaded stack essential if the actuator must pull as well as push. The crystal is also sensitive to side loads and moments, both axial and perpendicular to the axis. Care must be taken in design to decouple side loads and moments from the actuator. This is typically accomplished by placing a ball tip or a flexural universal joint on one end of the actuator.

A survey of available piezoelectric actuators shows that the stiffest actuators have a stiffness of over $1100 \text{ N}/\mu\text{m}$ but only have available travel of $20 \mu\text{m}$. The stiffest actuators can generate 30kN of force, overkill for the needs of the PFT. The $120 \mu\text{m}$ model of the 30kN series from Polytec PI has a stiffness of $240 \text{ N}/\mu\text{m}$. The longest travel stack actuators have $180\mu\text{m}$ of travel, but only have a stiffness of $35 \text{ N}/\mu\text{m}$ and have an overall length of 184 mm . Flexure guided motion magnifying piezo actuators are available with travels of over 1 mm , but their stiffness is less than $1 \text{ N}/\mu\text{m}$. Piezo actuated crawler motors have travel of several millimeters and a stiffness of around $75 \text{ N}/\mu\text{m}$. Crawler motors have the added complexity of switching from step mode to analog mode. After surveying the available actuators, it became apparent that none of the available actuators have the combination of stiffness and travel necessary to be used as the sole actuator in the PFT.

Since no existing actuator meets all the design requirements, a dual actuator system was investigated. A dual actuator system uses a coarse actuator

to roughly position the template or wafer and a fine actuator to finish positioning the system. The coarse and fine actuators can be in series or arranged such that one moves the template side and the other moves the wafer side of the tool. The coarse actuator should be able to align the system to within the travel range of the fine actuator. There are many motorized micrometer drives that have micrometer resolution or better. They typically have a stiffness of less than one $\text{N}/\mu\text{m}$. A stiff piezo in series with a compliant micrometer drive will, of course, be more compliant than the micrometer. A micrometer drive could be used to move one side of the system, coarsely aligning the system. A lock is then be engaged to prevent further movement, turning the highly compliant mechanism into a highly stiff structure. A stiff, short travel piezo actuated mechanism could then move the other side of the machine to achieve final alignment. The longest travel piezos with enough stiffness do not have enough travel to capture gap reference signals, but they do have enough travel to correct for misalignments and to control the gap and stretch the pillars, if desired. The travel for correcting for different wafers and templates and for collecting gap references will have to be provided by the coarse drive side of the machine.

Based on the actuators available, the new tool will need two tip/tilt/Z mechanisms in parallel. A large travel, low stiffness mechanism will move the wafer side of the system to adjust for different wafer and template thicknesses and other large variations. Once the wafer is positioned inside the actuation envelope of the template side mechanism, a lock will be engaged to hold the

system still and increase the stiffness. The template side of the system will be actuated by highly stiff piezoelectric actuators in a 3-RPS mechanism.

7.1.2 Kinematics and Stiffness

Based on the actuators available, the machine needs two three degree of freedom mechanisms, one for the wafer side and one for the template side. Both mechanisms need to have a total stiffness, measured at the wafer - template interface, of 1000 N/ μm .

7.1.2.1 Template Side Mechanism

The mechanism chosen for the template side is the 3-RPS mechanism. Each leg consists of a pin joint, a piezo actuator, and a universal joint. The joints will be flexure based joints to avoid problems of backlash and stiction. The joints need to meet the competing requirements of high axial stiffness and low angular stiffness. High axial stiffness requires large minimum dimensions while low angular stiffness requires small minimum dimensions. The joint designs chosen were the semicircular cut pin joint and universal joint. The flexure joints are pictured in figure 7.1 The axial and angular stiffnesses are[51]

Universal Joint

$$k_a = \frac{Et^{3/2}}{2r^{1/2}} \quad (7.1)$$

$$k_\theta = \frac{Et^{7/2}}{20r^{1/2}} \quad (7.2)$$

Pin Joint

$$k_a = \frac{Ew}{(\pi(r/t)^{1/2} - 2.57)} \quad (7.3)$$

$$k_\theta = \frac{2Ewt^{5/2}}{9\pi r^{1/2}} \quad (7.4)$$

In the above equations, k_a is the axial stiffness, k_θ is the angular stiffness, r is the cut radius, t is the minimum thickness, E is Young's modulus, and w is the width of the pin joint. In both the universal joint and the pin joint, the angular stiffness depends on the minimum thickness to a much higher power than the axial stiffness. This is because the angular stiffness is a bending effect and the axial stiffness is a linear effect. A material with a high Young's modulus allows a thinner minimum thickness while preserving high axial stiffness. This thinner minimum thickness results in a much lower angular stiffness in spite of the stiffer material.

The total stiffness of the system is the sum of the network of springs. The axial stiffness of each leg is the reciprocal of the sum of the reciprocals of the individual stiffnesses. The stiffness of all three legs taken together is the sum of the individual legs. The legs are in series with the template holder, so the total mechanism axial stiffness is determined by the reciprocal of the sum of the reciprocals of the legs and template holder stiffnesses.

Steel flexures were determined to give the lowest angular stiffness while meeting the axial stiffness requirements. The flexure dimensions and stiffnesses are shown in table 7.1. The stack of flexures and piezo actuator that make up the mechanism leg is shown in figure 7.1. The actuator chosen was the P-247.50

	Universal Joint	Pin Joint
Cut Radius (in)	0.125	0.25
Minimum Thickness (in)	0.375	0.1
Flexure Width (in)	N/A	1
Axial Stiffness (N/um)	1700	2200
Angular Stiffness (N*m/rad)	15500	1500

Table 7.1: Dimensions and stiffnesses of flexures in proposed design

from Physik Instrumente. This actuator has $80\mu\text{m}$ of travel, a static stiffness of $360\text{N}/\mu\text{m}$, and can generate 30kN of pushing force. Now that the stiffnesses are known, the side loads applied to the actuators can be calculated. First, the maximum joint actuation needs to be determined. The maximum actuation of both the universal joints and the pin joints occurs when two legs are at their minimum length and the third leg is at its maximum. The maximum actuation was chosen to be $50\mu\text{m}$ so that $30\mu\text{m}$ of travel is available to move all three actuators in unison once the alignment is corrected. Equation 2.1 was solved given the known link lengths. The result was that, in the maximum actuation position, the short legs are perfectly vertical and the long leg is tilted in $6.07\text{E-}8$ rad. The U-joint at the top of the leg is rotated $2.14\text{E-}4$ rad. Given the stiffnesses of the joints, the torques required can be determined. The torques are

$$M_{ujoint} = k_{\theta_{ujoint}} \times \theta_{ujoint} \quad (7.5)$$

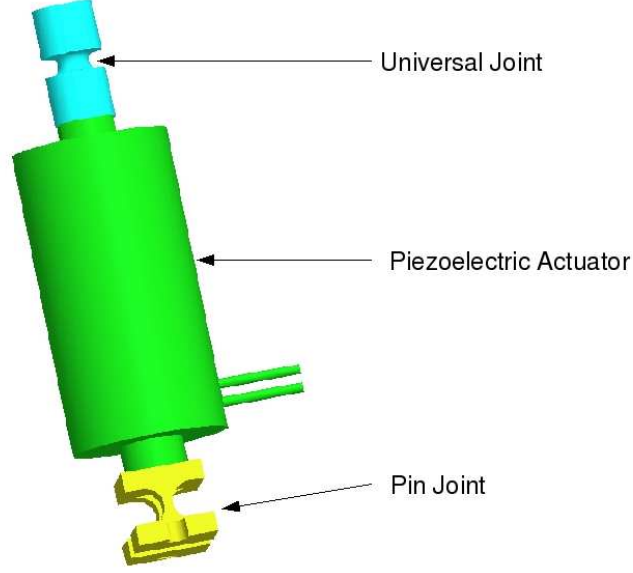


Figure 7.1: Mechanism leg consisting of piezo actuators and flexures

$$M_{pin} = k_{\theta_{pin}} \times \theta_{pin} \quad (7.6)$$

The side load of interest is the load at the tip of the piezo stack. To determine the side load, cut the link at a height h corresponding to the tip of the actuator and add the internal side load L . The side load is

$$L = (M_{pin} - M_{ujoint})/h \quad (7.7)$$

For the joint stiffnesses and the actuators used in this design, the maximum side load is 27N. This load is higher than a piezo actuator can sustain without breaking. The side load can be decreased by decreasing the angular stiffness or by reducing the actuation difference. Reducing the allowable

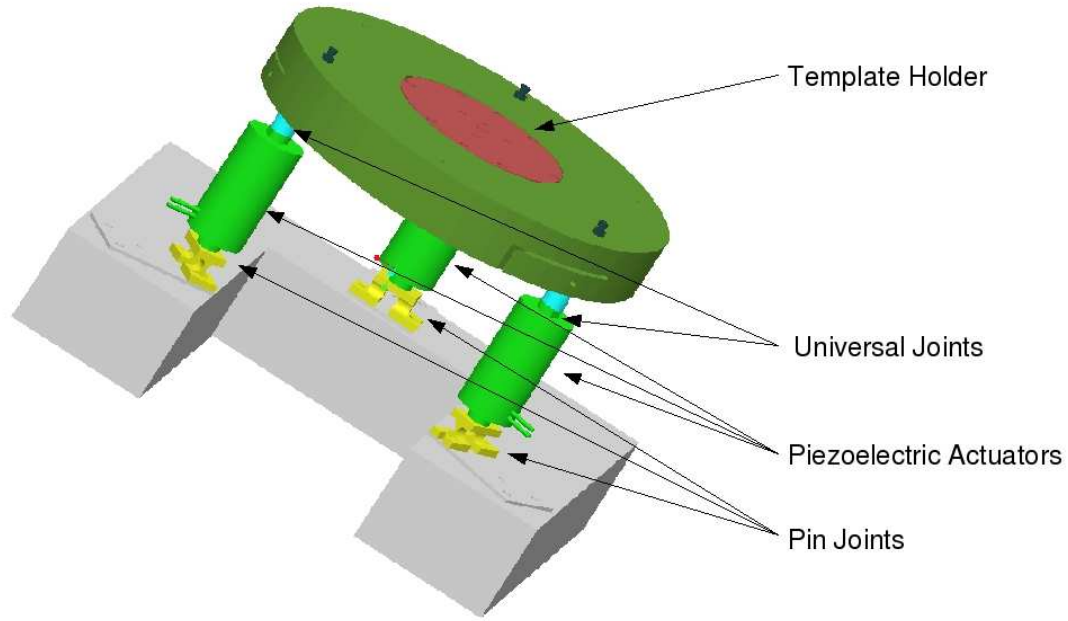


Figure 7.2: Template side mechanisms

actuation difference reduces the amount of travel available to correct misalignment. Reducing the angular stiffness also reduces the axial stiffness, causing the mechanism to exceed the allowable compliance. The template side mechanism can not be made stiff enough without generating large side loads, so an alternative to a highly stiff mechanism is necessary. The alternative will be discussed after the wafer side design is discussed. The template side mechanism is shown in figure 7.2.

7.1.2.2 Wafer Side Mechanism

The wafer side mechanism has to do several things. It must allow for wafer loading and have enough travel to capture gap sensing reference signals

and adjust for different wafer and template thicknesses. It must clamp the wafer mechanism in place once it is inside the operational envelope of the template side mechanism. An air bearing slide was included in the design to allow the wafer chuck carrier to move sideways for wafer loading.

Several designs were investigated for the wafer side mechanism. Three degree of freedom systems with vacuum preloaded air bearings and micrometer actuators were investigated and rejected due to stiffness and complexity issues. One side of the air bearing wafer mechanism is shown in figure 7.3. A one degree of freedom mechanism that can lift the template into position was chosen to try to achieve the necessary stiffness. The wafer chuck carrier is located axially by an air bushing and actuated vertically by voice coils from BEI Kimco. An air solenoid actuated clamp holds the mechanism in place once the proper position is reached. Position feedback for the mechanism is provided by linear encoders on the wafer side mechanism and the gap sensors. The wafer side mechanism is shown in figure 7.4

There are a lot of problems with this design. The stiffness and positional accuracy ultimately depend on the clamp. The clamp must be stiff enough to resist the applied loads, strong enough not to slide under load, and accurate enough to engage without moving the wafer chuck. The wafer side mechanism is not constrained to the template side mechanism. This gives extra positioning freedom but sacrifices positioning accuracy. Designing a system with sufficient stiffness and travel proved to be a very difficult problem. A force compensation scheme that can decrease the necessary stiffness was investigated next.

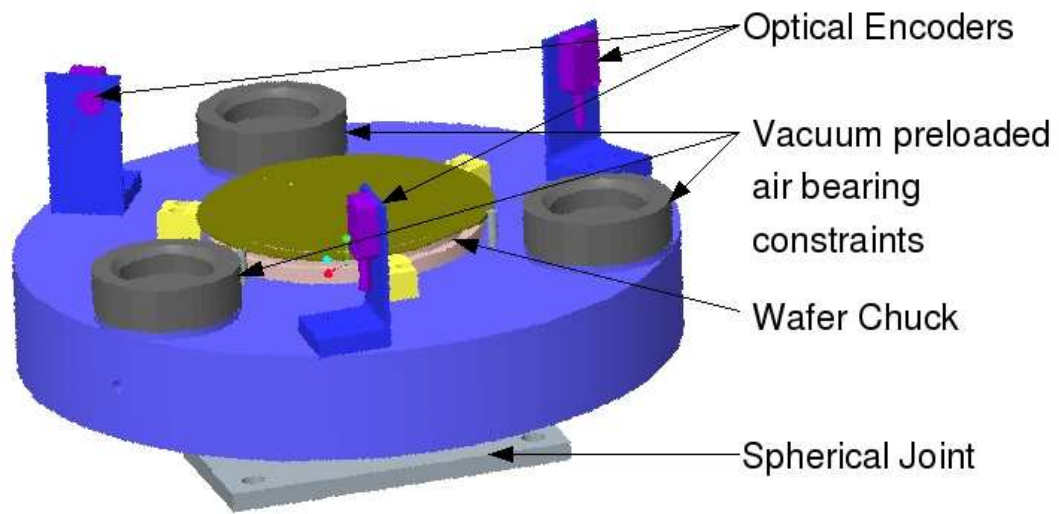


Figure 7.3: Air bearing wafer side mechanism

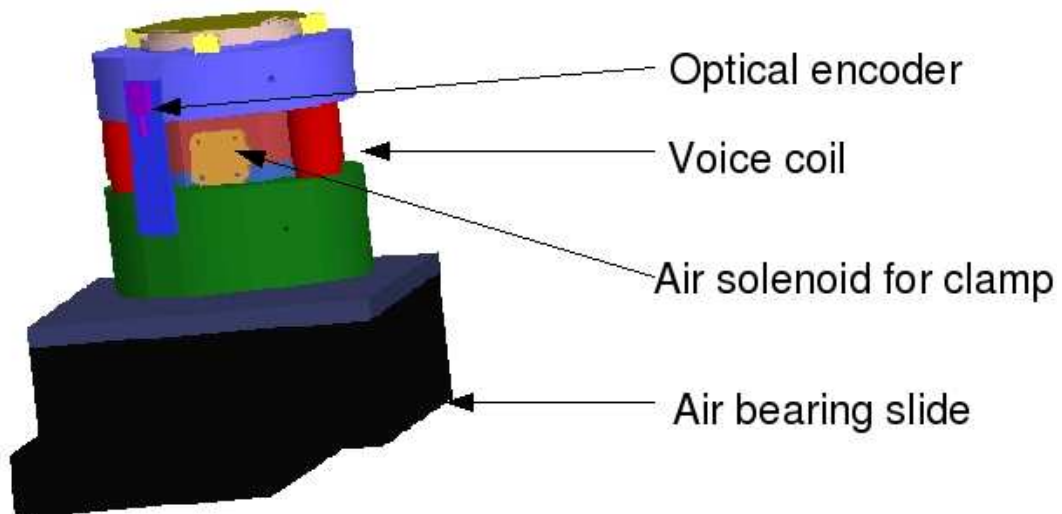


Figure 7.4: Wafer side mechanism

7.2 Force Compensation Designs

If a highly stiff machine is impractical, can the need for stiffness somehow be reduced? A compensation force, properly applied, could counteract the electrostatic force and prevent movement. The compensation force needs to be a pure force with no motion required. The compensator must not kinematically constrain the mechanism further, since that would result in over-constraint. The compensator also cannot interfere with the other physical requirements of the system. The active area must remain available for gap sensing, video, and ultraviolet illumination. An actuator with all of these properties seems utopian, but it is available. A voice coil or set of voice coils can meet these requirements. Using a voice coil as a pure force generator is an atypical application, but it can be used that way.

The voice coil system needs to supply a symmetric compensation force. Placing one voice coil directly over the center of the active area would provide symmetry, but it would also cover the active area, interfering with gap sensing, illumination, and video. A ring of voice coils provides the needed symmetry while allowing access to the active area. Based on the size of the available voice coils and the space available around the template, a ring of three voice coils was chosen.

Force compensation will depend either on accurate *a priori* knowledge of the force or feedback of the force signal. Since another actuator system simultaneously controls the position, force feedback could become problematic. In the pillar formation process, the applied force is well known, allowing the

use of feedforward control.

The complete Pillar Formation Tool, with voice coils for force compensation, is pictured in figure 7.5. With force compensation, the needed stiffness is reduced, but how much the necessary stiffness is reduced depends on the effectiveness of the force compensation. The proposed PFT has many issues with unproven solutions. The wafer side mechanism requires a clamp that is stiff, strong, and does not disturb the mechanism when engaged. The template side mechanism has high side loads on the piezo actuators. The sideloads can be reduced by making the flexure joints more compliant, but how much the stiffness can be reduced is unknown. It is desirable to determine the effectiveness of force compensation before building the complete system.

The Active Gap Tool, which was used in the early pillar formation experiments, meets all of the physical requirements for pillar formation and has the necessary travel. The AGT can be adapted to meet the actuation resolution requirements and to supply the voice coil force compensation. The AGT was originally developed for research in Step and Flash Imprint Lithography. Imprint Lithography has vastly different requirements from pillar formation, so the adapted tool may be suboptimal for use as a pillar tool. However, the effectiveness of feedforward force compensation can be investigated, and the results used to refine the requirements for the PFT.

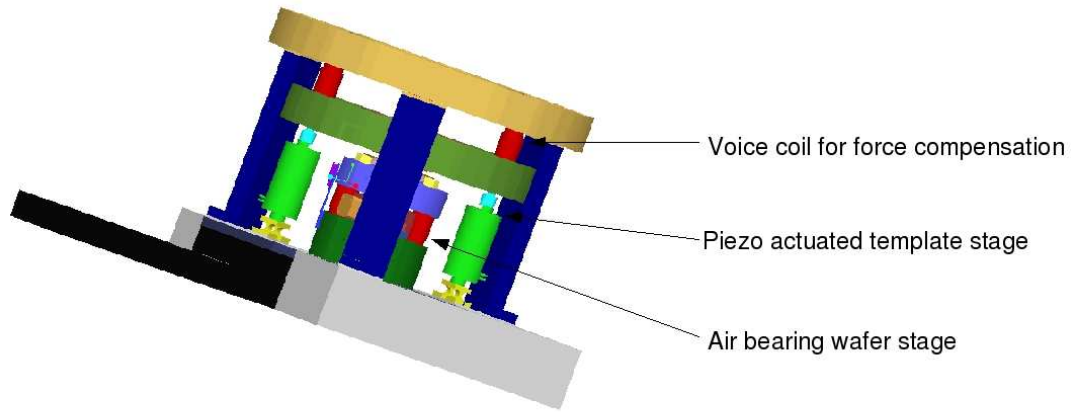


Figure 7.5: Pillar Formation Tool with voice coil compensation

7.2.1 Return to the Active Gap Tool

The Active Gap Tool has the necessary kinematics, range of motion, and wafer handling capabilities, but it lacks the required actuation precision and stiffness. The stiffness requirement can be reduced with the addition of voice coil compensation. The original micrometer motors can align the active area to within $\approx 0.5\mu\text{m}$. To increase the actuation resolution without sacrificing range of travel, piezo actuators are attached to the tip of the motors. The total system stiffness is less than the stiffness of the motors by themselves, but voice coil compensation should reduce the need for stiffness. Experience gained with the AGT shows that $\approx 5\mu\text{m}$ of precision actuation will correct for the misalignment remaining after alignment with the motors. Another $10\mu\text{m}$ of travel will allow for pillar stretching experiments. Experience also shows that about 20lbf (89N) is needed to separate the template and wafer after the pillars are cured. The P843.10 from Physik Instrumente was chosen to add to

the actuator legs. This actuator has $15\mu\text{m}$ of travel and can generate 800N of pushing force and 300N of pulling force. A strain gage built into the actuator provides feedback to the actuator power supply. The feedback sensor can make the actuator behave much stiffer than its open loop stiffness of $57\text{N}/\mu\text{m}$.

7.2.1.1 Modifications to the Active Gap Tool

Several modifications were made to the active gap tool. Adding the piezo actuator to the mechanism leg makes the leg longer by more than the 37mm length of the actuator because thread adapters are required. The longer mechanism leg requires longer structure uprights. A new force sensor is also needed. The original force sensor on the Active Gap Tool was a 100lbf piezo-electric force sensor. The 100lbf sensor made sense when the tool was used for imprint lithography, but the forces in pillar formation are much lower. Therefore, the force sensors were replaced with 10lbf piezoelectric sensors. The sensor electronics were also replaced with conditioners that allow quasi-static operation.

The voice coils chosen were model LA10-12-07A from BEI Kimco. These voice coils have a stroke of 9mm, a peak force of 13.3N and a continuous stall force of 4.6N. The force compensation design is a nontraditional application for a voice coil, so the peak and stall force specifications may not apply. The voice coils are mounted in a 1 inch bolt circle around the active area.

The template holder was also replaced. The template holder must hold

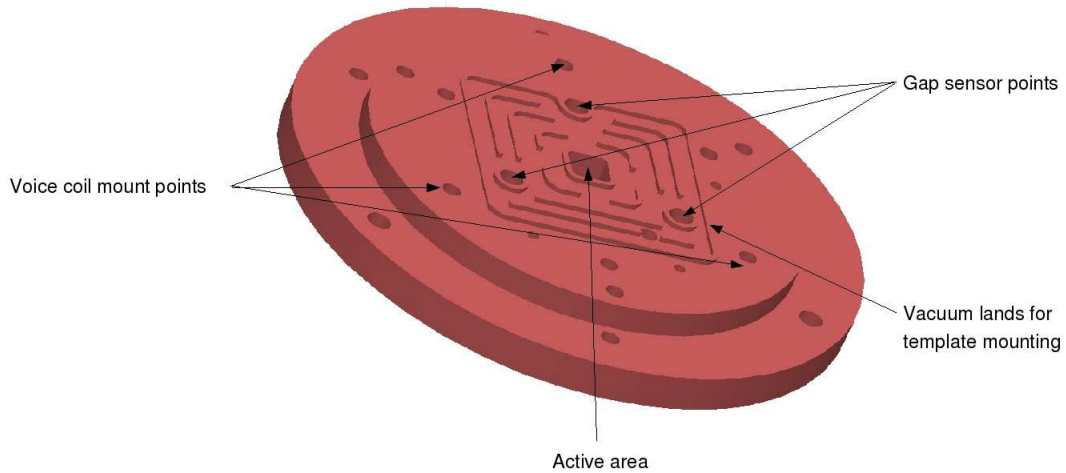


Figure 7.6: New template holder

several parts. It must hold the 65mm template with vacuum, the 3 gap sensors that sense gap alignment, and hold the magnet side of the voice coils. The template is held by a series of raised vacuum lands. The outer and inner land seal the vacuum area and the interior lands provide support against template bowing. The gap sensors are mounted in a 1in. circle around the active area. Vacuum lands around the gap sensing holes provide vacuum sealing. On the top side, the gap sensor focusing lenses screw into the gap sensing holes to mount the reflection probes. Several mounting locations are provided for the voice coils at a variety of bolt circle diameters and both at the same angular positions as the motors and halfway between the motors so different mounting positions could be tested. The template holder was made of 7075 aluminum and hard anodized. The vacuum land surface was polished to a flatness of 50nm. The template side of the template holder is pictured in figure 7.6

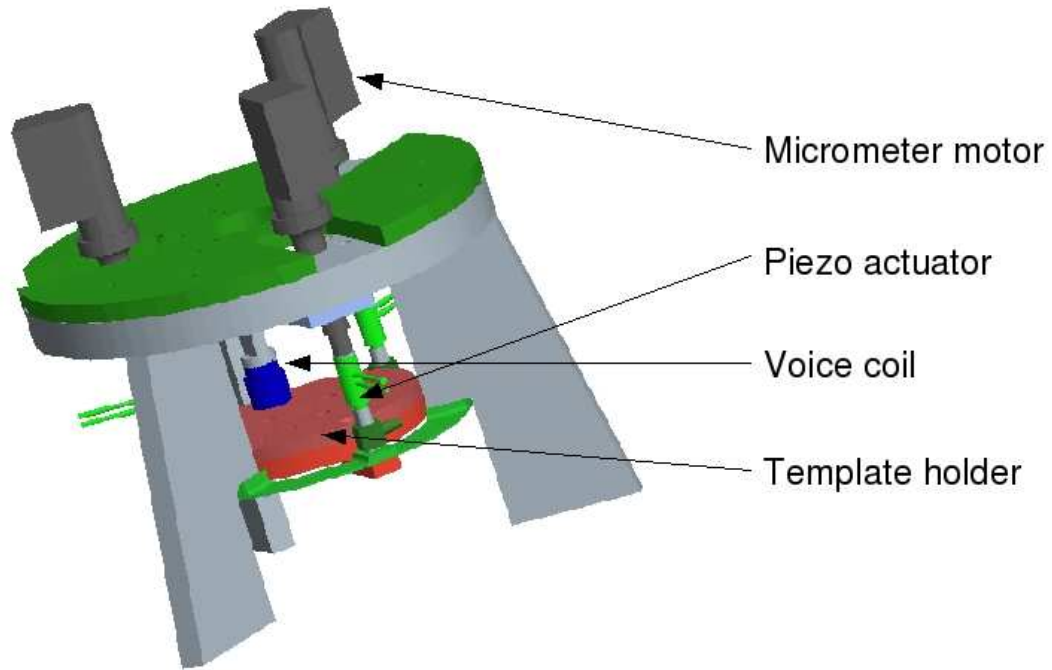


Figure 7.7: The Hybrid Active Gap Tool, with gap sensors and two voice coils removed for clarity

The coil side of the voice coils also needs a mount. A plate was machined to mount to the top of the tool with mounting holes corresponding to the holes in the template holder. Posts hold the coil and bridge the gap between the top mount and the voice coil position. The modifications to the Active Gap Tool are shown in figure 7.7. The Modified Active Gap Tool is shown in figure 7.9.

The side loads on the piezo actuators were estimated in the same manner as in the PFT design. The universal joint in the active gap tool has a stiffness of 22N-m/rad and the pin joint has a stiffness of 55.7N-m/rad . If the legs differ in length by $100\mu\text{m}$, a $.15\text{N}$ side load occurs. If the legs differ in

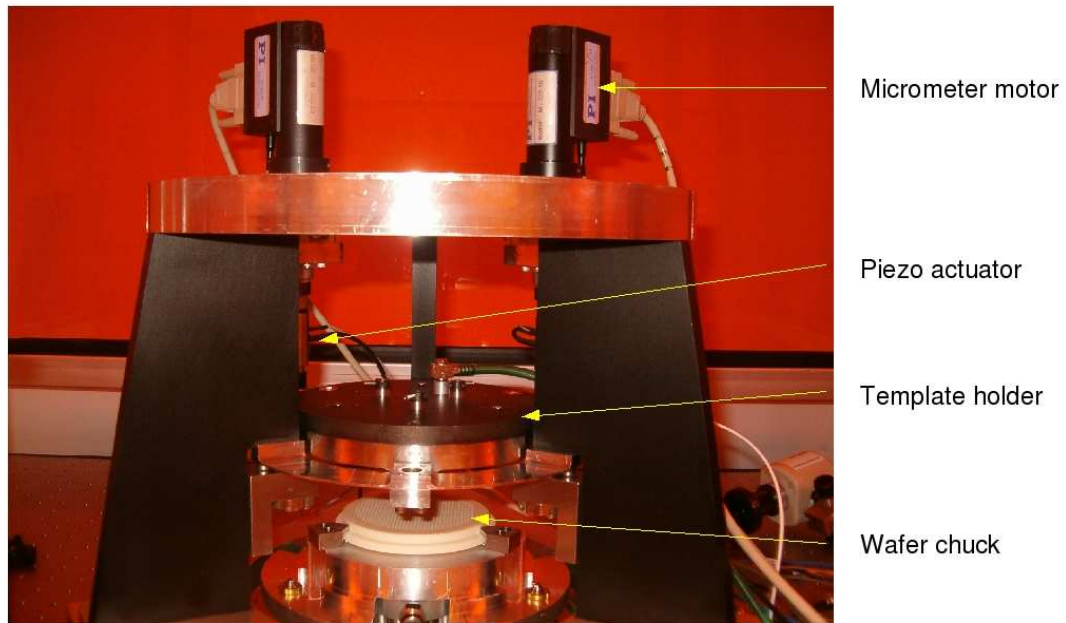


Figure 7.8: Hybrid Active Gap Tool, during assembly

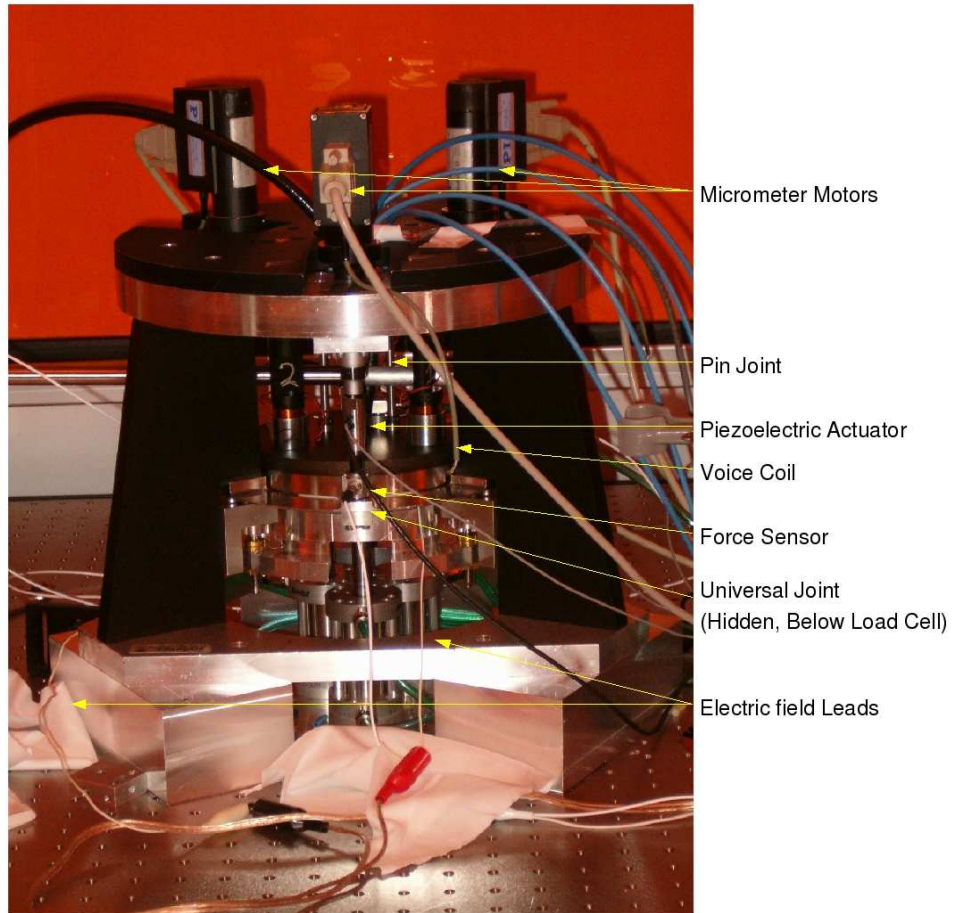


Figure 7.9: Hybrid Active Gap Tool

length by $10\mu\text{m}$, the side load decreases to .015N. The side load will likely increase slightly due to manufacturing tolerances and other nonidealities.

The modified Active Gap Tool has two types of actuators, piezoelectric actuators for position control and voice coils for force compensation. This arrangement can be described as hybrid actuation. The modified Active Gap Tool is therefore named the Hybrid Active Gap Tool (HAGT). The HAGT has the travel and actuation resolution required for the pillar process. The piezo actuators allow for high precision gap orientation alignment and the voice coils allow for force compensation. The HAGT is an adaptation of an existing tool, so it may be a suboptimal design. However, the feasibility of hybrid actuation using piezo actuators for position control and voice coils for force compensation can be investigated. The knowledge gained from the HAGT can then be used to refine the requirements and design for the PFT.

Chapter 8

Control System

The control system for the Hybrid Active Gap Tool performs several functions. When at large gaps, the operator manually controls the micrometer motors to approach the operating position. Once near the operating position, the piezoelectric actuators are controlled with a slow, quasi-static control law to achieve parallelism at the desired gap without exciting uncontrollable dynamics. The voice coils are used in a feedforward compensator to counteract the template electrostatic force. Each part of the control system will now be discussed in detail

8.1 Motor Control Mode and System Overview

The HAGT is controlled using Labview software with National Instruments data acquisition and analog output cards along with motor controller and spectrometer controller cards from other manufacturers. The motor control mode allows the operator to load wafers and templates, collect gap reference signals, roughly align the system, and move the template close to the operating position. A screenshot of the motor mode software is shown in Figure 8.1.

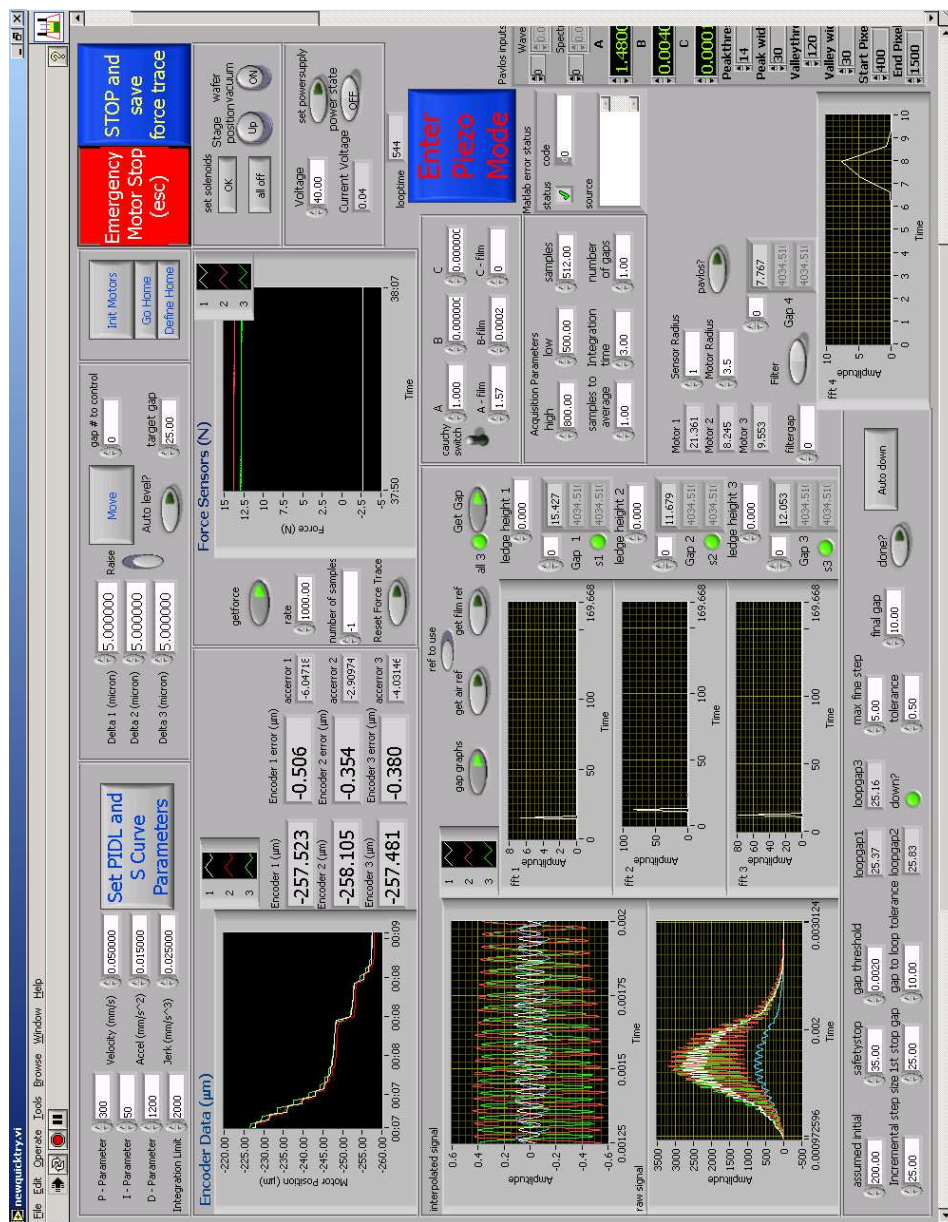


Figure 8.1: Screenshot of the motor mode software

The motor mode is an open loop control system. The operator reads the gap sensor output and issues appropriate position move commands to the motors. In motor mode, the gap sensor software generates unpadded Fourier transform graphs of the gap signal. These graphs are useful for detecting faint interference signals when the system is far from parallel due to reassembly or template installation. Alignment better than one micron is possible in motor mode. When the template is close to the desired operating condition, typically around $5\mu\text{m}$, the operator sends the system into piezo mode. The piezo mode software is shown in figure 8.2.

8.2 Quasi-Static Control

The piezo mode control uses the gap sensors as feedback to correct the gap between the template and wafer for parallelism and absolute gap. The system approaches the desired position slowly to avoid exciting any uncontrollable dynamics. The control commands are positions, not velocities. System overhead restricts the control system to operate at a rate of 1Hz. The slow sample rate, slow approach, and position commands lead to terming the control system a quasi-static system.

8.2.1 Gap Transform

The feedback for control comes from the gap sensors, which are arranged around a one inch radius circle. The control effort comes from the piezos, which are arranged around a 3.5 inch radius circle. If the template

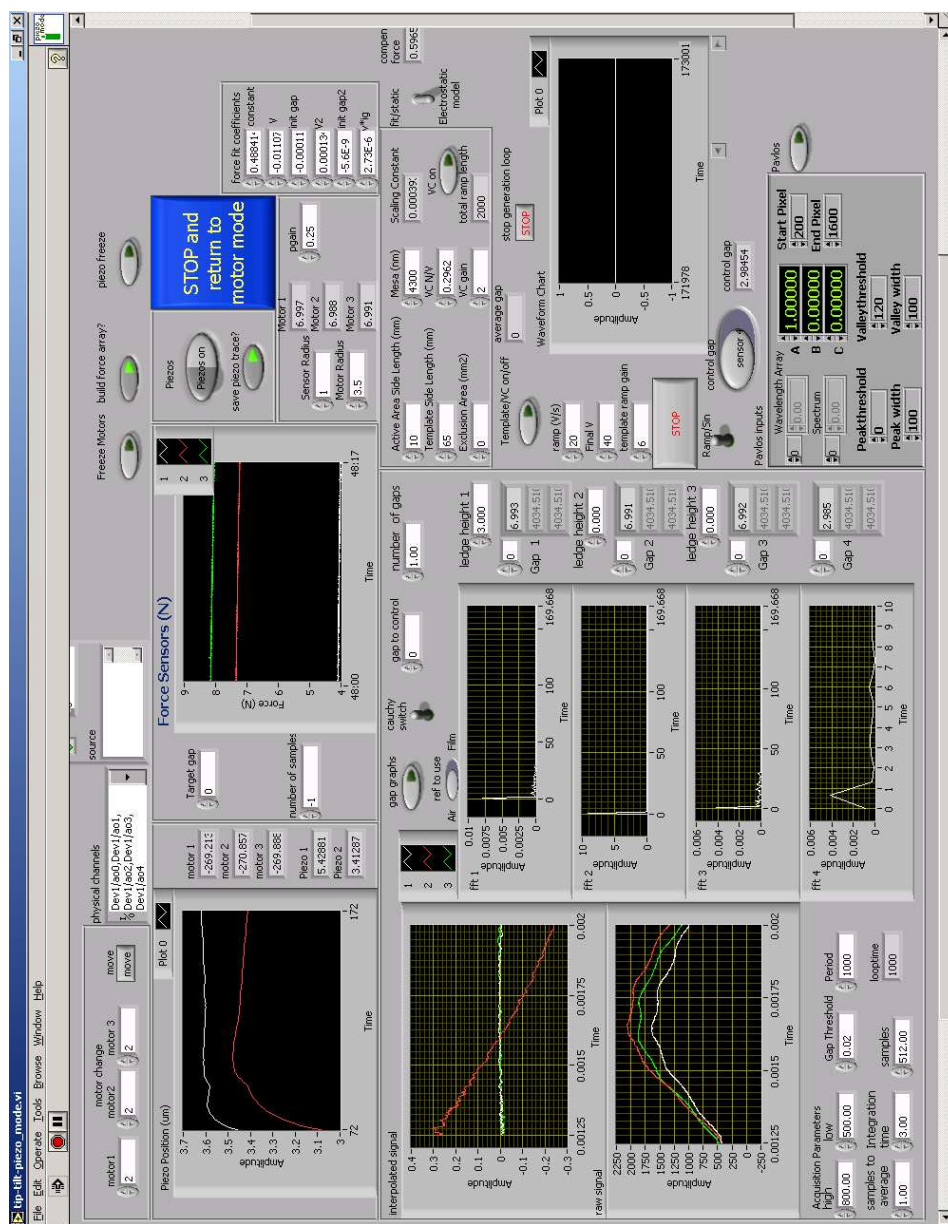


Figure 8.2: Screenshot of the piezo mode software

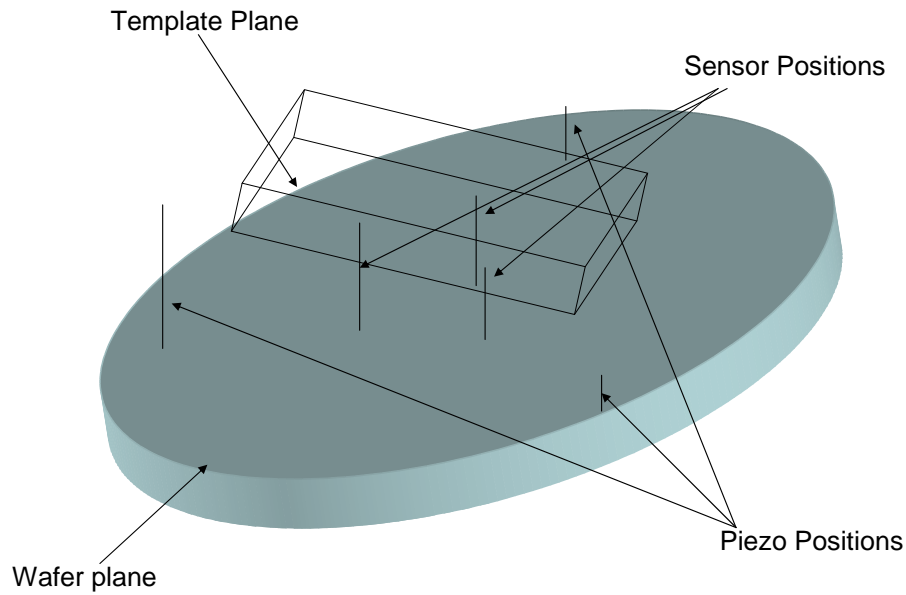


Figure 8.3: Template and wafer planes sensor and motor locations

holder behaves enough like a rigid body, a simple linear transform can take the feedback information from the gap sensors and determine how far the piezo actuators should move to reach the desired position.

The transform derivation starts with the assumption that the gap sensor points and the desired piezo positions lie in the same plane. The situation is shown in figure 8.3 The goal is to find the distance of the motor positions from the wafer surface. The motor positions are known in the template plane, as are the gap sensor positions. The gap sensor locations are also known with

respect to the wafer. The planes are out of parallel by microns over lengths of centimeters, so the x and y positions of the motors and sensors are assumed to be identical in both planes. The gap sensors can be used to define the template plane with respect to the wafer. The gap sensor positions with respect to the wafer are

$$\begin{aligned}\vec{a} &= (0, -r, g_a) \\ \vec{b} &= \left(\frac{-1}{\sqrt{3}}r, 0.5r, g_b \right) \\ \vec{c} &= \left(\frac{1}{\sqrt{3}}r, 0.5r, g_b \right)\end{aligned}\tag{8.1}$$

A plane can be described by the equation

$$n_x x + n_y y + n_z z + d = 0\tag{8.2}$$

where n_x , etc are the components of the plane normal vector in the desired reference frame, x, y , and z are the coordinates in the reference frame, and d is a constant. Any combination of x , y , and z that satisfy equation 8.2 are in the plane. The plane normal vector can be determined by defining the vectors

$$\vec{u} = \vec{a} - \vec{b}\tag{8.3}$$

and

$$\vec{v} = \vec{b} - \vec{c}\tag{8.4}$$

which lie in the plane. The normal vector is then

$$\vec{n} = \vec{u} \times \vec{v}\tag{8.5}$$

The final part of the plane equation, the constant d is determined by taking the dot product of the normal vector and one of the point vectors

$$-d = \vec{n} \cdot \vec{a}. \quad (8.6)$$

Equation 8.2 can now be used to determine the motor positions. The x and y positions of the motors are known.

$$\begin{aligned} M_{1x} &= 0 & M_{1y} &= -R \\ M_{2x} &= \frac{-1}{\sqrt{3}}R & M_{2y} &= 0.5R \\ M_{3x} &= \frac{1}{\sqrt{3}}R & M_{3y} &= 0.5R \end{aligned} \quad (8.7)$$

The desired heights are then found by solving Eq. 8.2 for z and substituting the appropriate x and y values.

$$\begin{aligned} M_{1z} &= \frac{-d - n_x M_{1x} - n_y M_{1y}}{n_z} \\ M_{2z} &= \frac{-d - n_x M_{2x} - n_y M_{2y}}{n_z} \\ M_{3z} &= \frac{-d - n_x M_{3x} - n_y M_{3y}}{n_z} \end{aligned} \quad (8.8)$$

The sensor and motor positions are at the same angular positions equally spaced around circles of radii r and R , respectively. The transform therefore simplifies to the simple matrix equation

$$\begin{bmatrix} M_{1z} \\ M_{2z} \\ M_{3z} \end{bmatrix} = \frac{1}{3r} \begin{bmatrix} r + 2R & r - R & r - R \\ r - R & r + 2R & r - R \\ r - R & r - R & r + 2R \end{bmatrix} \begin{bmatrix} g_1 \\ g_2 \\ g_3 \end{bmatrix} \quad (8.9)$$

where M_{1z} , etc. is the z position of the corresponding motor point, R is the motor radius, r is the sensor radius, and g_1 , etc. is the corresponding gap sensor reading.

A few sanity checks show that the transform has the proper properties. First, the matrix is dimensionless, as it must be to transform a length into

another length. If the radii are equal, the matrix simplifies to the identity matrix. If the motor radius is 0, meaning that each motor point is at the center of the sensor circle, the matrix gives each motor point the average of the three gap sensors, as expected. If the transform is inverted, the gap radius r and motor radius R trade places, as expected.

A physical check further verifies the validity of the transform. In the Active Gap Tool, if one motor or piezo is moved it should not affect the other two motors, but all three gap sensors are affected. Experience on the Active Gap Tool shows that this is indeed the case. Moving one or two motors by 10 or 20 μm results in the reported position of the unmoved motor changing by no more than 1 μm . The machine is not infinitely stiff and the radius of the motors is only known to a few thousandths of an inch, so that amount of change is expected.

8.2.2 Control Law

Now that the position of the motors is known, the error from the desired position can be determined and corrected. When the template is parallel to the wafer and at the desired height, the gap sensors and the motor positions will all be equal to the desired height. If the desired gap is H , the error E_i is

$$\begin{aligned} E_1 &= M_{1z} - H \\ E_2 &= M_{2z} - H \\ E_3 &= m_{3z} - H \end{aligned} \tag{8.10}$$

If the entire error is corrected at once, the system may become unstable. The individual control efforts e_i are therefore found by multiplying the error by a

gain P less than 1.

$$\begin{aligned} e_1 &= PE_1 \\ e_2 &= PE_2 \\ e_3 &= PE_3 \end{aligned} \tag{8.11}$$

The control effort is the desired expansion of the piezo actuator. In general, the actuator is already displaced, so at each control cycle the new control effort must be added to the previous effort.

$$e(i+1) = e(i) + PE(i) \tag{8.12}$$

The control law assumes the velocity of the machine is essentially zero. so the control law is quasi-static. The control law consists of a term proportional to the current error and the sum of previous efforts. The control effort is essentially an integral of the error, so it is termed a quasi-static integral controller.

8.2.2.1 Control Results

Several times during these experiments and during assembly, internal loading resulted in piezo actuators breaking. We believe that better understanding of the mechanism and its sensitivity will lead to making the design more robust. Having said that, the broken actuator resulted in a mechanism with high resolution tip/tilt capabilities and lower resolution Z-axis control capability. The control law was adapted to control the two mechanism legs with piezo actuators to the same height as the third, lower resolution leg. The absolute gap was adjusted by moving the micrometer motors with the two piezo actuators controlling the orientation. The gap control scheme was

more than sufficient to maintain parallelism of the wafer and template. Piezo actuated orientation control with voice coil force compensation was demonstrated on the HAGT. The main goal of achieving parallel template and wafer at a known gap, and holding that gap when the electric field is applied, was achieved.

The tip-tilt control law was tested without application of the electric field. With a gain of 0.25, the controller corrected parallelism with a steady state error near zero. The absolute gap would drift, however. The drift was sometimes as much as 50nm/min. The drift was determined to be caused by temperature variation in the room. The controller can adjust the two legs with piezos to counteract any thermal drift, but the third leg expands freely. The controller in tip/tilt mode kept the template parallel to the wafer, and tracked the thermal expansion of the third leg. Temperature tracking and gap control experiments conducted over several hours showed that the observed drift in the tool matches the room temperature variation. The central gap and room temperature over several hours are shown in figure 8.4. The room temperature varies by about 3°C and the machine drifts by about 1 μ m .

Several approaches can be taken to eliminate the thermal drift. The temperature controller for the cleanroom can be replaced with a new one. The current controller keeps the temperature of the room within about 2°C. Newer controllers can keep the temperature of the room stable to 0.5°C. This would cut the thermal drift to about a quarter of the previous 1 μ m . The machine can also be placed within a temperature controlled microenvironment.

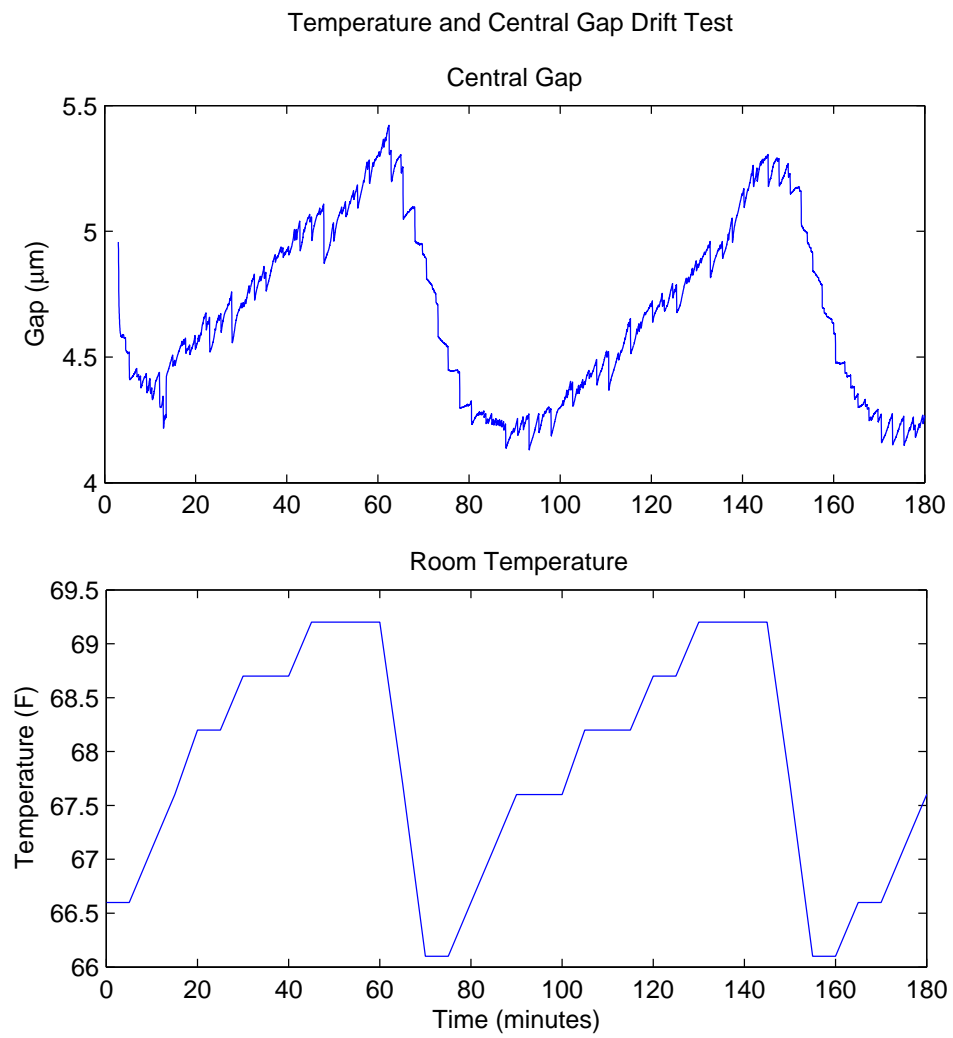


Figure 8.4: Central gap and temperature drift over several hours.

Microenvironments can control the temperature to a few millidegrees, but they are expensive. Better understanding of the mechanism internal loading will lead to a more robust design with high resolution absolute gap control. With high resolution absolute gap control, the control law will automatically adjust for thermal drift, but the thermal drift must be accounted for in available travel calculations. The amount of thermal drift the controller must compensate for is unavailable for orientation and gap control, so the total available travel is decreased. The ideal solution would be to reduce the temperature variation by either or both of the available methods and to develop a more robust design that can correct for the inevitable disturbances.

8.2.3 Mesa Calibration

The Hybrid Active Gap Tool's purpose is to keep a template parallel to a wafer at a known gap. The template has a mesa etched into the surface, resulting in the active area protruding from the template surface. The gap sensors are located around the active area, not inside the active area. The mesa height needs to be precisely known so the it can be subtracted from the gap sensor readings, yielding the active area gap. The problem of mesa calibration is not a simple one. Several approaches were tried before a satisfactory method was determined.

The first attempts to measure the mesa height were direct measurements. The step height at the mesa edge can be measured with a profilometer or a gap sensor. This yields a very accurate measure of the step height, but

the etch used to create the mesa is not uniform enough for the direct measurement to be used. Wet buffered oxide etch, stirred wet buffered oxide etch, and dry reactive ion etches were utilized in an attempt to produce a uniform mesa height, but all of the etching methods yielded similar results. The etch height varies by several hundred nanometers, too much to allow the use of a single mesa height to calibrate the gap sensors.

A Zygo interferometer was also used in an attempt to measure the profile of the whole template, but the step height was too great for the interferometer to measure. The interferometer did, however reveal an aspect of the difficulty in mesa calibration. The interferometer was used to measure the profile of the template holder, a template on the template holder, and a wafer on the wafer chuck. The results are shown in figures 8.6 ,8.7 and 8.8. The wafer chuck and template chuck, even though polished to be highly flat, are not perfectly flat. The wafer chuck and template chuck each have several hundred nanometers of non-flatness. What started as a mesa height measurement problem turns out to be a system calibration problem. The situation is shown in figure 8.5. A mesa of unknown height and flatness is etched into a template that is mounted on a template holder that is also not flat. A wafer that is not flat is mounted on a wafer chuck that is not flat. The gap of interest is the gap between the active area and the wafer. The gap can be directly measured with a fourth sensor, but the parallelism cannot be controlled unless the three surrounding gap sensors are corrected by subtracting the total height of all the flatness variations and the local mesa height for each sensor.

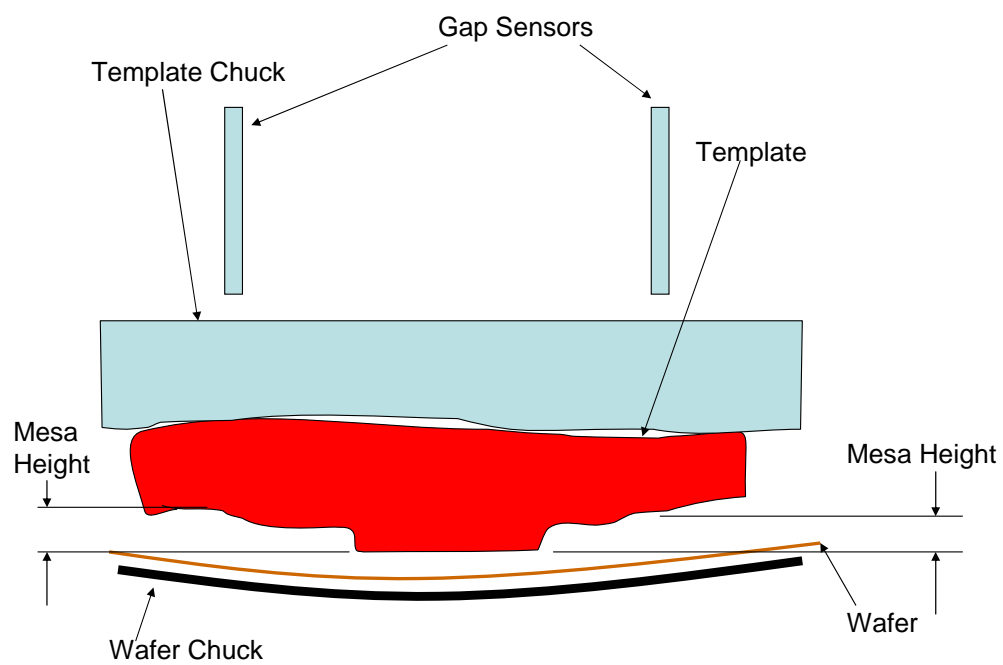


Figure 8.5: Illustration of mesa calibration problem, with unflatness exaggerated

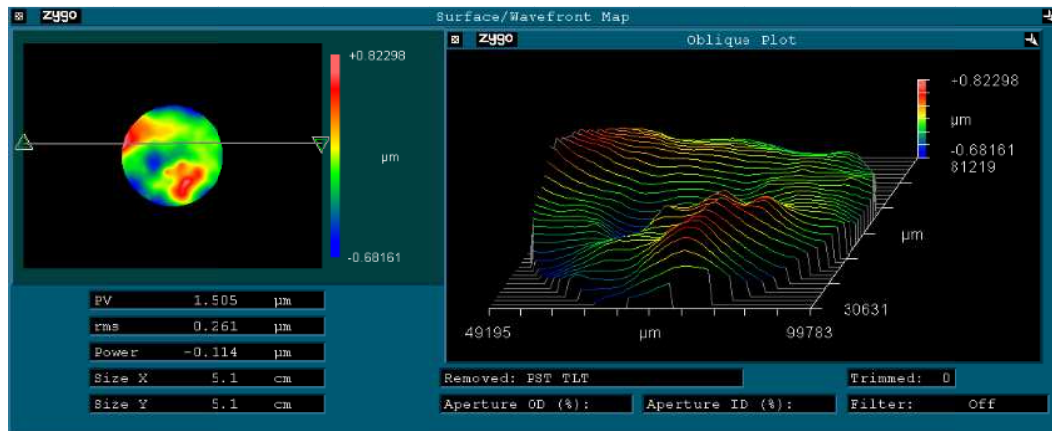


Figure 8.6: Profile of wafer on wafer chuck, measured with Zygo Interferometer

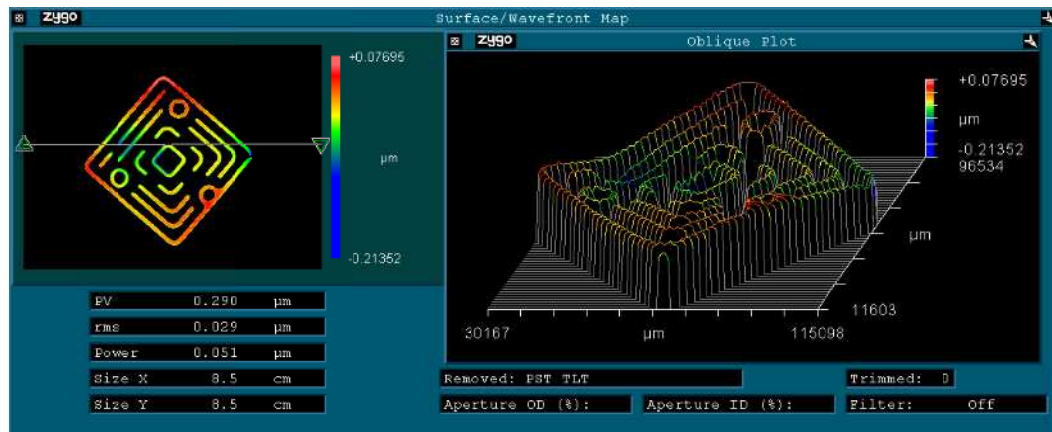


Figure 8.7: Profile of template chuck, measured with Zygo Interferometer

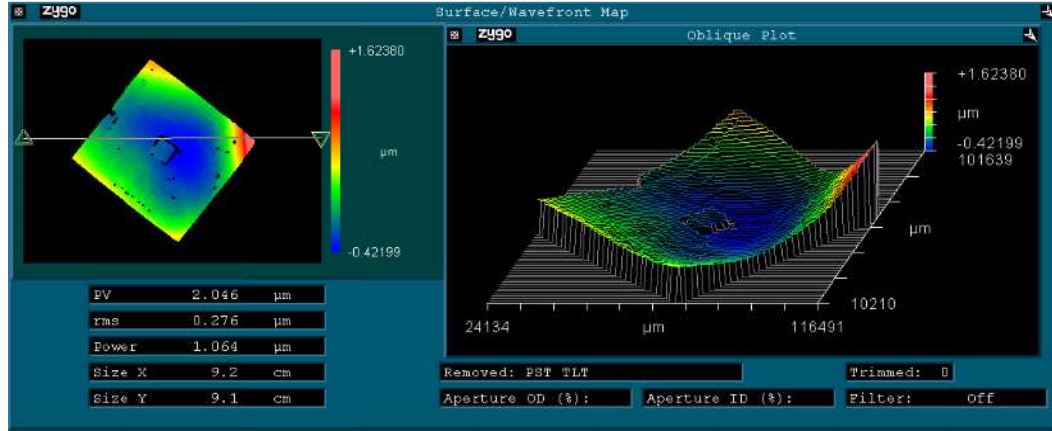


Figure 8.8: Profile of template on template chuck, measured with Zygo Interferometer

The calibration problem was solved by using a fourth gap sensor and calibrating the system as a whole. To calibrate the system, the tool is set to a gap of about $10\mu\text{m}$. The fourth gap sensor is used to measure the gap between the active area and the wafer at three locations corresponding to the angular positions of the gap sensors. The fourth sensor measurements are transformed to the gap positions and the difference between the outer gap sensor and the transformed inner sensor reading is taken to be the calibrated mesa height. These heights are input to the control system and the controller is engaged. The fourth sensor measurements are repeated and the mesa heights further refined. The thermal drift of the tip/tilt system makes a perfect calibration difficult, but a total indicated range across the active area of less than 100nm is possible.

8.3 Voice Coil Compensation

The voice coils are intended to provide static force compensation to keep the gap between the wafer and template constant when the electric field is applied. Voice coils are generally used as motion generators, not force generators, so the calibration supplied by the manufacturer is not sufficient. The voice coils were calibrated both separate from the machine and installed in the machine. The calibration was used with the electrostatic model of the template force to derive a feedforward compensator.

8.3.1 Voice Coil Calibration

The voice coil system consists of the voice coils and the voice coil driver. The input is a voltage signal from the analog output card in the system computer. The voice coil driver is the TA115 linear servo amplifier from Trust Automation. The driver is controlled via a differential analog input and outputs current when in torque mode and voltage when in velocity mode. The voice coils are intended to produce a force, so the controller is configured for torque mode. The driver produces a current proportional to the input voltage, and the current generates a force. The relationship between input voltage and force generated was determined by calibration.

A frame was built to hold the voice coils and a piezoelectric force sensor. The frame is shown in figure 8.9. The frame was built so that the height of the coil relative to the permanent magnet could be adjusted to the height seen when installed in the Hybrid Active Gap Tool. Each voice coil was calibrated

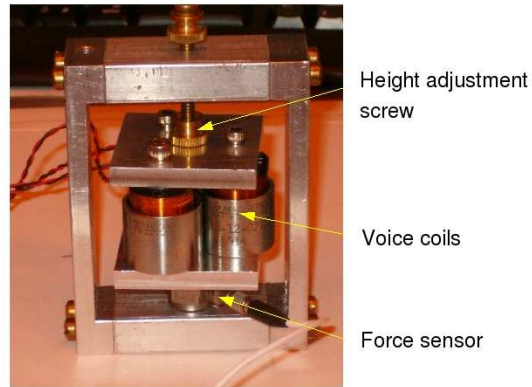


Figure 8.9: Voice coil calibration frame

separately and the three voice coils were calibrated together. The calibration curves are shown in figure 8.10. The calibration curves are all remarkably straight lines. The difference in slopes of the individual voice coils is $.0027N/V$, less than 2% of the average slope. The three voice coils wired in parallel has a slightly higher slope, about 3% higher than the average of the individual voice coils. The voice coil system behaves in a predictable, linear, very low noise manner. This makes the feedforward system simpler.

8.3.2 Feedforward Compensation

The intent of the voice coils is to counteract the force applied by the template, thereby canceling any change of gap induced by the electric field. If the template voltage is applied instantaneously, the resulting impulse force will be impossible to match in time or in magnitude. The template voltage is therefore ramped up over a period of 1 or 2 seconds. The compensating force

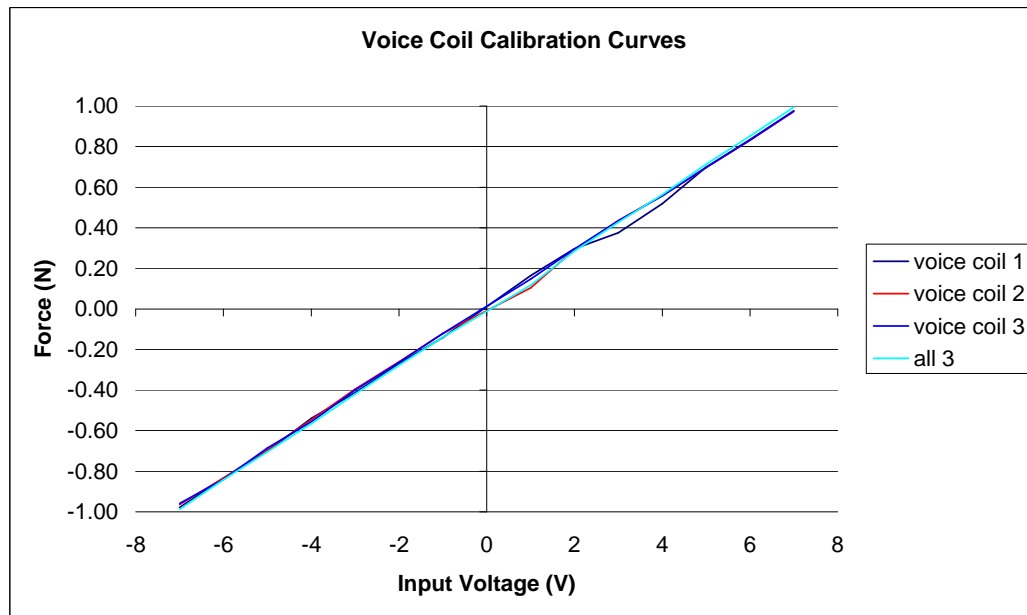


Figure 8.10: Voice coil calibration results

can then be calculated and ramped up at the same rate. Supplying the ramp signals from the same analog output card ensures the two signals are sent at the same time.

To determine the compensating force needed, the electrostatic force needs to be found first. From Eq. 5.4, the electrostatic force is

$$F = \frac{aa^2V^2\epsilon}{2g^2} + \frac{(L^2 - aa^2 - A_e)V^2\epsilon}{2(g+m)^2} \quad (8.13)$$

This equation can be factored into a constant that depends on the geometry multiplied by the voltage squared.

$$F = \left(\frac{aa^2\epsilon}{2g^2} + \frac{(L^2 - aa^2 - A_e)\epsilon}{2(g+m)^2} \right) V^2 = CV^2 \quad (8.14)$$

The force generated by the voice coils is

$$F = kV_{vc} \quad (8.15)$$

where k is the slope of the voice coil calibration curve in N/V and V_{vc} is the control voltage supplied to the voice coil driver. The forces should be equal, so the voice coil control voltage is

$$V_{vc} = \frac{CV^2}{k} \quad (8.16)$$

The compensation force may need to be adjusted for nonideal behavior, such as an uneven mesa etch. An adjustable gain is therefore included in the voice coil control voltage

$$V_{vc} = \frac{CV^2}{k}G \quad (8.17)$$

The adjustable gain is important for several reasons. The voice coil compensation is intended to hold the template holder still. The wafer side of the tool is still free to move. As discussed in the design requirement chapter, the total machine stiffness consists of the stiffness of both the wafer and template sides. The wafer side will still move because the electrical force is still applied to it. If the voice coils compensate exactly for the electrical force, the template holder will remain in place, but the wafer will still move, making the gap smaller. If the voice coils apply the proper amount of extra force, they will move the template holder up at the same time as the wafer moves up. The voice coils will then compensate for the stiffness of both sides of the tool with a force applied to only one side of the tool. The proper value of the voice coil gain was determined by a calibration for each template.

Now that the voice coil control voltage has been determined, the feed-forward ramp can be calculated. The voltage ramps need to be smooth to allow the force to grow slowly without impulsive jumps. An update rate of 1kHz was chosen. The control system sample rate is 1Hz, so 1000 points of the ramp need to be calculated and written for each control cycle. In each control cycle, the template constant is calculated based on the current gap readings. The template voltage follows a smooth linear ramp up to the desired final voltage. The voice coil control voltage is calculated based on the current template constant and equation 8.17. Once the template voltage reaches the desired final value, it is held constant and the voice coil control voltage is updated based on the current template constant and gap reading. In the current im-

plementation, the wafer and template are typically separated after the pillars are cured and before the voltage is turned off, so there is no need for smooth voltage reduction. The control voltages are therefore simply turned off when the experiment is finished. A smooth reduction can be easily implemented in software if it is desired in the future.

Template damage can affect the applied force. The conductive surface of the template is susceptible to damage by a variety of means. The most common is damage by arcing. Arcing occurs between the template and the wafer when the electric field becomes too strong. The field strength at which arcing occurs is difficult to predict because it typically starts at the edge of the mesa. The sharp corner at the edge of the mesa causes charge concentration and other nonlinear effects that reduce the field required for arcing. The sharpness of the corner and other unpredictable factors affect how much the dielectric breakdown voltage is reduced. Once arcing occurs, a spider web pattern forms on the template surface where locally high currents flow. The spider web pattern reduces the effective conductive area. A damaged template can still form pillars, but not in the damaged area. The effect of the damage is to reduce the effective area of the template. In cases of damaged templates, the applied force needs to be reduced. Each template will need to be calibrated to determine the effective area and mesa height. The calibration will need to be repeated after arcing damage occurs.

8.3.3 Sensitivity Test

A sensitivity test was conducted to determine the proper value of the gain in Equation 8.17 for the template in use. The template and wafer were moved to a gap of 3600nm. The template voltage was set to a final value of 40V with a ramp rate of 20V/s. The voice coil gain was varied from 0.33 to 2. The results are shown in figure 8.11. For the template in use at the time, the proper gain value was 1. Lower gain values resulted in the gap shrinking while higher values resulted in larger gaps. The voice coil gain can be used to correct for uncertainty in mesa height, unelectrified areas, template and wafer unflatness, and other unknown effects, such as the various fluid forces.

8.4 Conclusion

The control system consists of a feedback section that uses the gap sensors to control the piezo actuators and a feedforward section to compensate for the applied electrical force. The system is currently operated in tip/tilt mode. The signal flow diagram of the control system is shown in figure 8.12. The voice coil feedforward control can compensate for the electrical field. A set of gap control experiments is described in the next chapter that investigates how well the tool functions throughout its operational range.

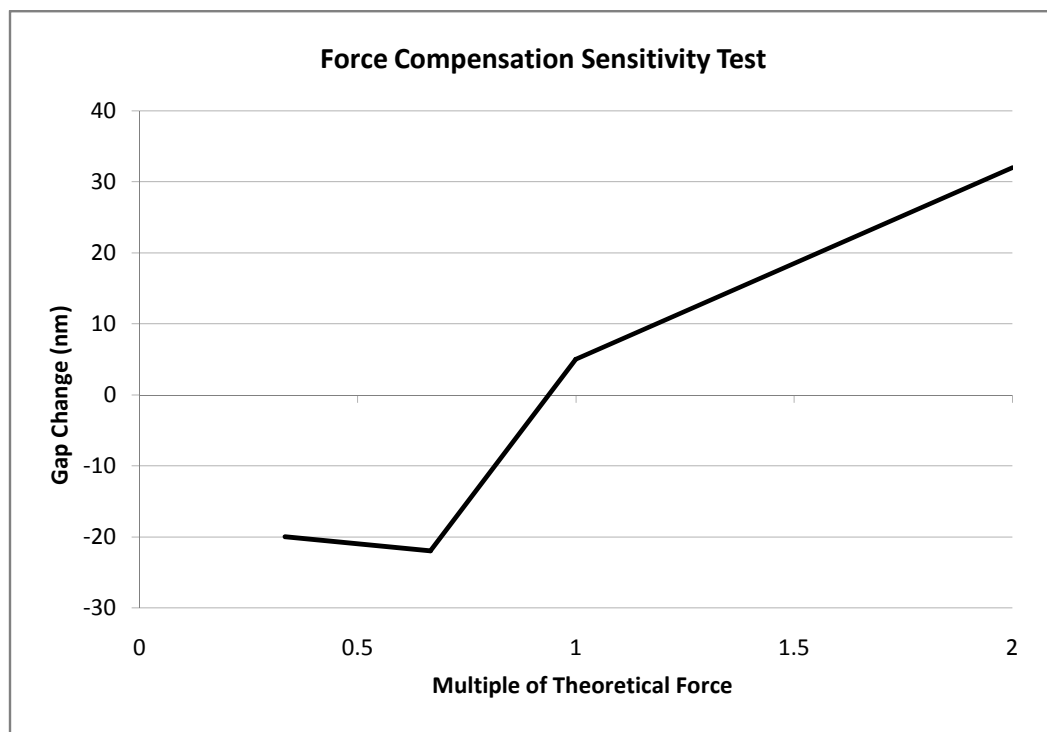


Figure 8.11: Force compensation sensitivity test

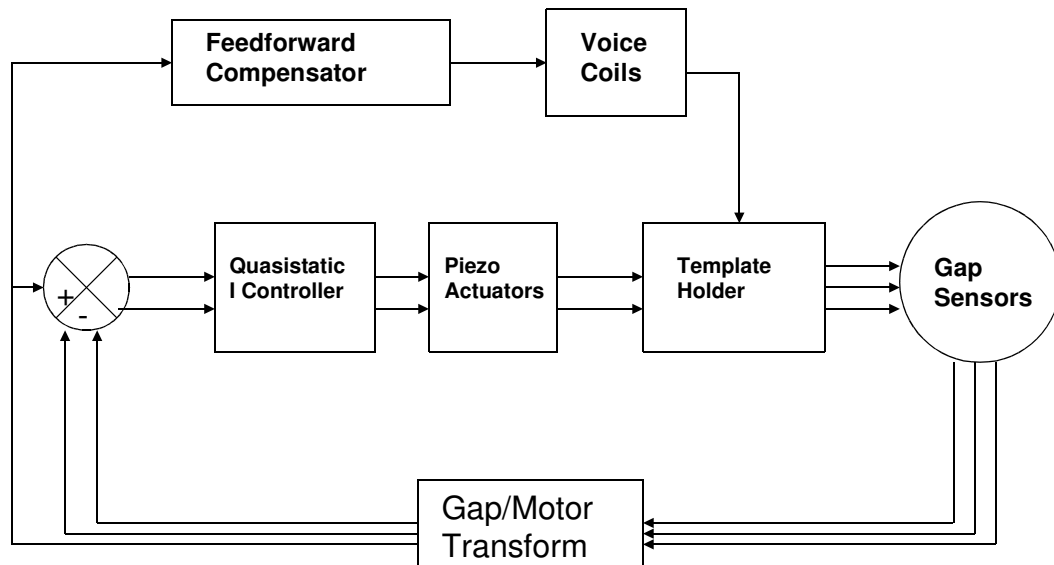


Figure 8.12: Control System Flowchart

Chapter 9

System Performance Experiments

A set of experiments was performed to investigate the performance of the Hybrid Active Gap Tool both with and without voice coil compensation throughout the operating range.

9.1 Experimental Methodology

The system software recorded both control inputs and system response. The control inputs recorded were the piezo actuator commands, gap electric field voltage, and voice coil voltages. The responses recorded were the force applied to each leg, the three gap sensors used to control orientation, and the central gap sensor. The forces, template voltage, and voice coil control voltage were recorded at a rate of 1kHz while the piezo control voltages and gaps were recorded at a rate of 1Hz. The experimental runs proceeded as follows:

1. The machine was adjusted to the desired operating gap.
2. The piezo actuators were engaged and the data recording started.
3. Once the control system settled, the gap electric field voltage was turned on, with or without the voice coils, as desired.

4. After a few seconds, the template (and voice coil) voltages were turned off.
5. The template and voice coil voltages were cycled for the desired number of cycles.
6. Once the desired number of cycles was complete, piezo control was disengaged and the data recorded.

An example data set is shown in figure 9.1. The top graph shows the gap values from the sensors used for orientation control. The middle graph is the gap between the active area and template. The bottom graph shows the gap electric field voltage and voice coil voltage. The recorded forces and are not shown in figure 9.1. The piezo commands are not graphed either. The piezo command information is useful in evaluating the control algorithm, but is not directly used in the performance experiments.

The recorded force is not necessary to determine the gap change when the electric field is turned on, but it is useful. The force of most interest is the total force applied to the template, which is the sum of the forces applied to the three legs. The force was filtered with a Gaussian mean line filter to remove noise. The recorded force serves several functions. First, the force is needed to determine the stiffness of the tool. Due to latencies in the control loop, the gap and voice coil voltage traces are not exactly in sync with the gap sensor traces. The recorded force information shows the precise times the voltages actually turn on and off. The force information can therefore be used

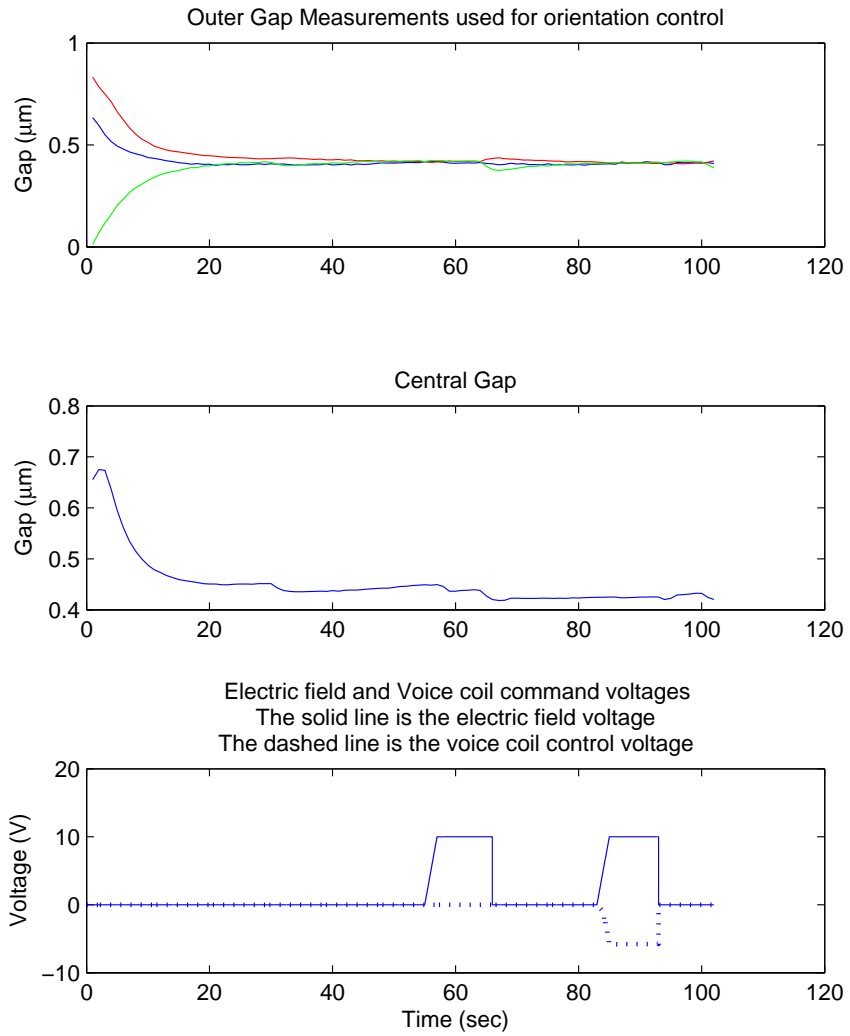


Figure 9.1: Experimental data set taken at a gap of 500nm with an applied voltage of 10volts

to help determine when the voltage ramp starts and stops if it is unclear in the gap graph. The total force for the experimental run shown in figure 9.1 is shown in figure 9.2. Since the object of the voice coil system is to eliminate all gap change, it can be difficult to determine when the electric field turns on and off from the gap trace alone. The timing information derived from the force trace is very useful in these situations. Finally, the gap change and measured force are related, so if the gap data has a good statistical fit, the force data should have a good fit as well. The applied force data can be used to help determine if specific data points are statistical outliers. The results of the gap change experiments showed that both gap change and applied force had fits of similar quality. Figure 9.2 shows the force, central gap, and gap electric field and voice coil voltages for one experimental run.

Analysis of the performance experiments requires the reduction of the data as shown in figures 9.1 and 9.2 to a set of performance values. The control factors needed are the initial gap, applied voltage, and whether or not the voice coils are used. The responses needed are the total force and the change in the central gap once the electric field voltage is fully applied. The control factors are easily extracted. Thermal drift and zero drift must be removed from the raw data to determine the force and gap change responses. Thermal drift is visible in the gap measurements. The force sensors are piezoelectric load cells with long time constants operated in a quasi-static mode. The long time constant manifests as a zero drift. Both drift sources have time constants or periods that are long with respect to the experiment length and can be treated

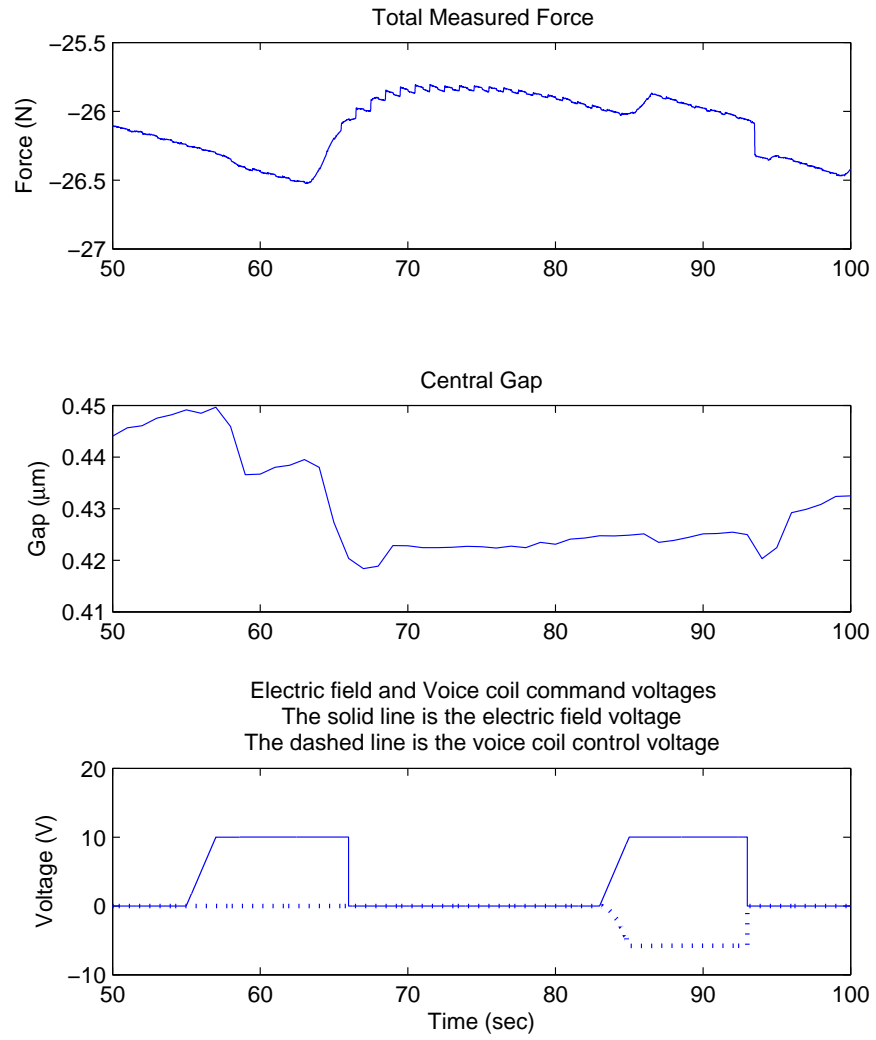


Figure 9.2: Experimental data set taken at a gap of 500nm with an applied voltage of 10 volts, including the total force applied to the template

as linear drifts over the duration of the experiment. To remove the effects of the drift, a single experimental event is located in the data (see fig 9.2). The filtered force and central gap data from before and after the experimental event are copied to a spreadsheet program. A linear trend line is fit to the data before the event (see fig. 9.3). The slope of the trend line is then used to subtract the effect of the drift from the raw data. The desired information, either the force change or gap change, can now be read from the graph of the corrected data trace.

9.2 Compensation Performance Experiments

Two performance experiments were conducted to investigate the effectiveness of the voice coil compensation. Both experiments were designed as $3 \times 3 \times 2$ full factorial experiments with 5 runs at each set of conditions. One experiment investigated the high gap/high voltage region of the performance envelope and the other investigated the small gap/low voltage region.

9.2.1 Experiment Design

The experiments were designed to investigate the operating space of the Hybrid Active Gap Tool. The independent variables in the experiment are the initial gap, the applied voltage, and whether or not the voice coils are used. The design space, with experimental points indicated, is shown in figure 9.4. The experimental points are clustered in the large gap, high voltage and the small gap, low voltage regions. The large gap, low voltage region is not investigated

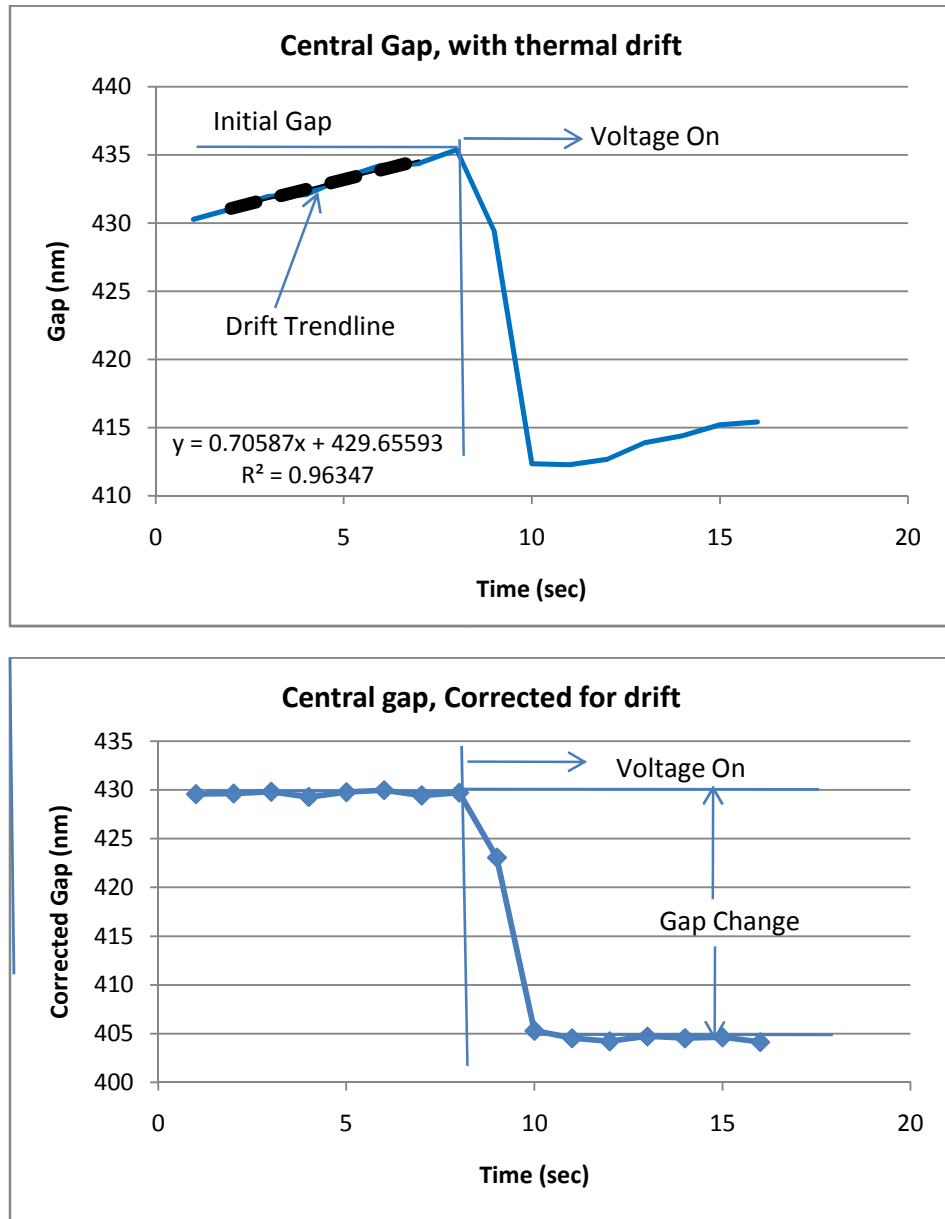


Figure 9.3: Central gap with drift correction. The top graph is the uncorrected gap data and the bottom graph is the central gap with the drift removed.

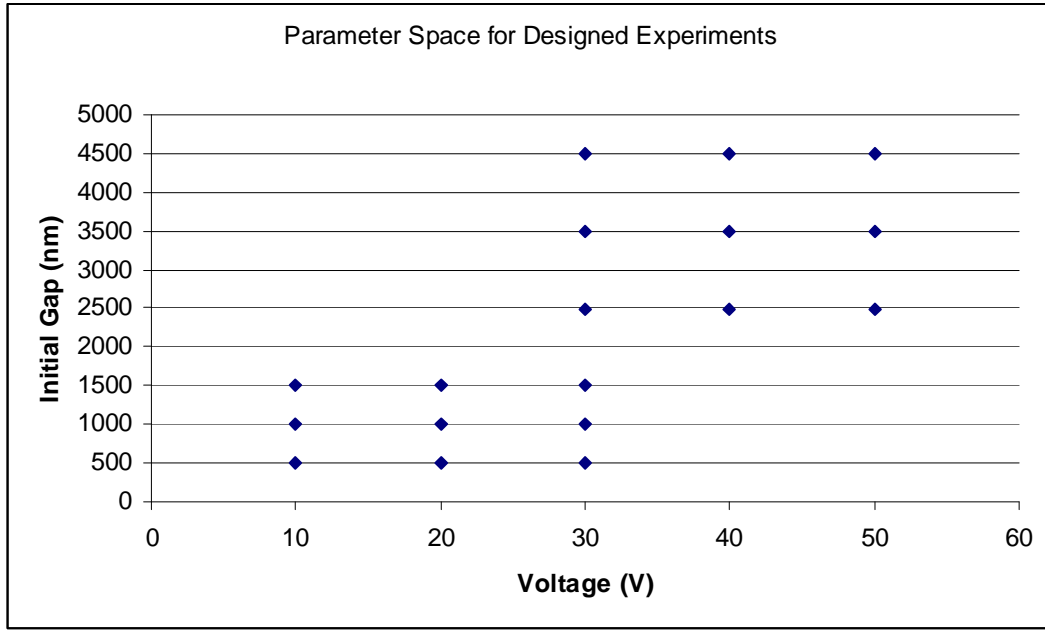


Figure 9.4: Parameter space for gap control experiments

because the electric field is too low to effectively make pillars. The small gap, high voltage region is excluded because the field is high enough to cause arcing between the template and wafer. Three values of voltage and initial gap were chosen so that curvature of the response surface could be seen. Each set of conditions was repeated 5 times to reduce the effect of measurement noise.

The data from the large gap, high voltage experiment with the voice coils off was collected first. The voltages for the first data set were chosen to give three values of active area electric field strength. Experience from this data set showed that it was preferable to choose three voltages. The voltage is directly controllable while the field is determined by the voltage and the gap.

Later data sets were designed with three uniform voltages because the voltage is independent of the gap.

The experiments were designed with three independent factors and two responses. The independent factors are the voltage, initial gap, and whether the voice coils are on or off. The responses are the gap change and the applied force. Gap change is the response of greatest interest. The force was included in the fit so the apparent stiffness of the machine could be estimated. The applied force should be related to the gap, so fitting the force can also serve as a check on the gap fit.

The apparent stiffness is the stiffness that the tool appears to have when the whole system, including gap control and force compensation, is considered. To determine the apparent stiffness, the electric field force is measured, with no force compensation, over the range of voltages and gaps of interest. The gap change is also measured, both with and without voice coil force compensation. Plotting the change in gap versus the electric field force shows the apparent stiffness behavior of the tool system. The slope of the gap change vs. applied force line is the apparent stiffness. If the force compensation is perfect, the gap change vs. force line will be vertical. If the voice coils overcompensate at some process conditions, the apparent stiffness may be negative. The actual structural stiffness is not negative, but the complete system, including the slight overcompensation from the voice coils, makes the tool have a negative displacement when a positive electric field force is applied, so the stiffness appears to be negative.

9.2.2 Experimental Results

Once collected, the data was analyzed in Design ExpertTM. Design Expert is a statistical package available from Stat-Ease, Inc. [52] to design and analyze experiments using principles of Design of Experiments. The Design Expert software can suggest sets of experimental conditions that will provide the most statistical information with the least number of experimental runs. Once the data is collected, the data is fitted to appropriate models (linear, cubic, etc) using least squares or other fitting methods and recommends which model provides the best statistical fit. After the experimenter chooses which model to use, based on the software suggestion and *a priori* knowledge of the system in question, Analysis Of Variance (ANOVA) is performed. The model that provides the best statistical fit is determined and the ANOVA results, statistical model, statistical diagnostic graphs, factor interaction graphs and response surface graphs are generated. The experimenter can then use the results to detect statistical outliers and to determine whether the model reasonably represents the data.

9.2.2.1 Large Gap, High Voltage

For the large gap, high voltage experiment, the gaps chosen were 2500, 3500, and 4500nm. The voltages chosen were 30, 40, and 50V. The gap and force data resulted in very good statistical models. The gap change is the response of greatest interest, and is discussed here. The force fit information is included in the appendix. The force fit was used for troubleshooting and

tool stiffness determination, as discussed earlier. The R^2 value for the fit shows how well the fitted model represents the data, with a perfect R^2 being 1. The Adequate Predictor statistic is a measure of the signal to noise ratio, with values greater than 4 indicating that the signal to noise ratio is large enough to allow the model to be used to predict system response. For the gap response of the large gap, high voltage experiment, the R^2 value is 0.99, which is exceptionally good and the adequate predictor statistic is 77.5, which is also exceptionally high. The high R^2 and adequate predictor values, along with other diagnostics included in the appendix, indicate that the statistical fit adequately represents the data.

The gap change without voice coil compensation is graphed in figure 9.5. The red dots represent the experimental points and the contours are the results of the statistical model. The gap change behaves as one would expect. The gap change is everywhere negative (the template and wafer move closer together) and the magnitude of the gap change increases with decreasing initial gap and increasing voltage. At a gap of 4000nm and a 40V, the gap decreases by about 20nm. At a gap of 2000nm and 50V, the gap decreases by 90nm.

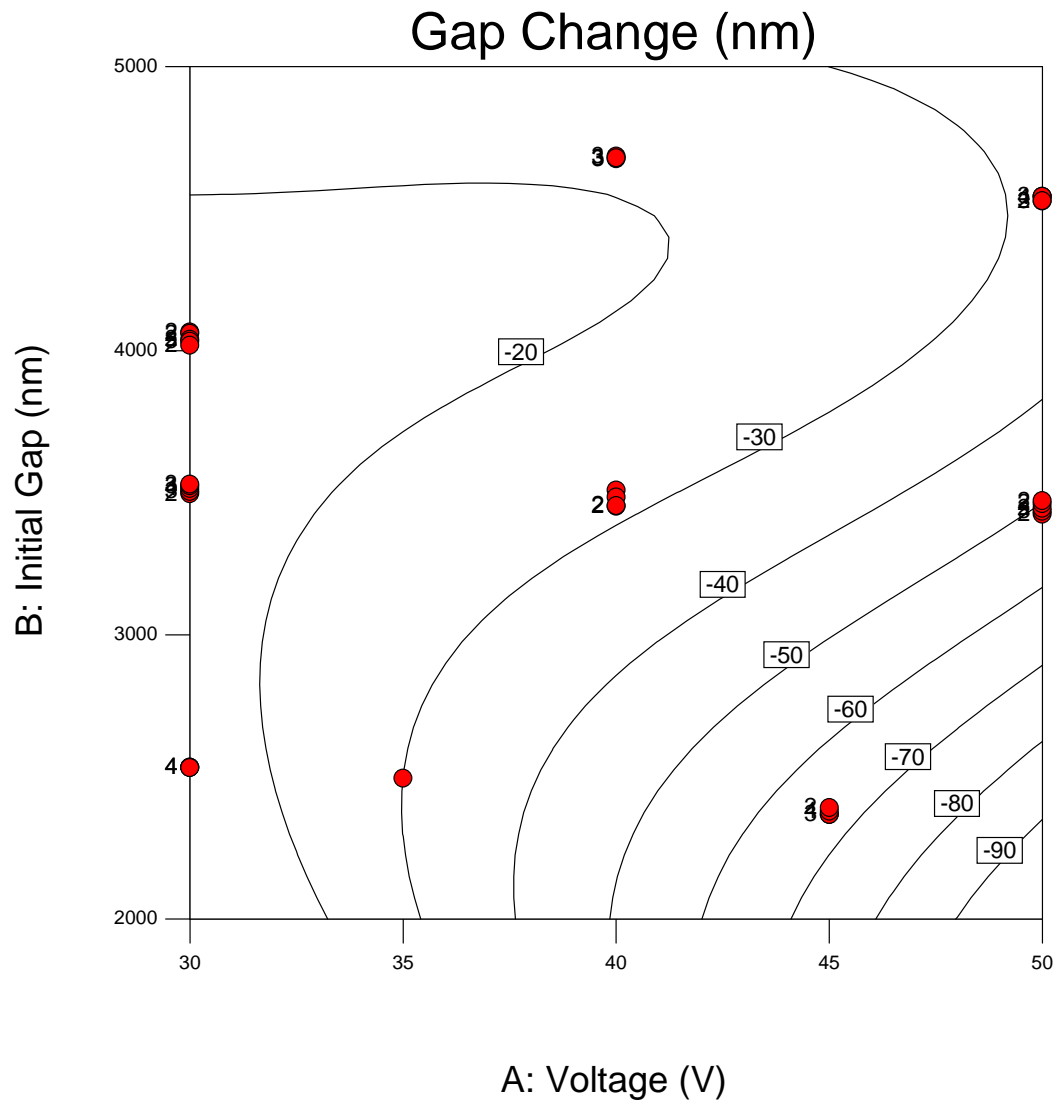


Figure 9.5: Response surface from the large gap, high voltage experiment for gap change without voice coil compensation

The best model was a cubic model. The fit equation for the voice coils off is

$$\begin{aligned}
 G = & 701.2834 \\
 & - 26.1158V \\
 & - 0.30888G_i \\
 & + 0.005676VG_i \\
 & + 0.350805V^2 \\
 & + 5.73 \times 10^{-5}G_i^2 \\
 & - 1.4 \times 10^{-5}V^2G_i \\
 & - 4.4 \times 10^{-7}VG_i^2 \\
 & - .00289V^3 \\
 & - 4.2 \times 10^{-9}G_i^3
 \end{aligned} \tag{9.1}$$

Figure 9.6 shows the gap change when the voice coils are engaged. The response surface is remarkably flat, with gap changes near zero. In some regions of the parameter space, the gap increases by as much as 6nm and in others the gap decreases by 6nm. The gap change is decreased from a range of 20 to 90nm of shrinkage to a range of from 6nm shrinkage to 6nm growth.

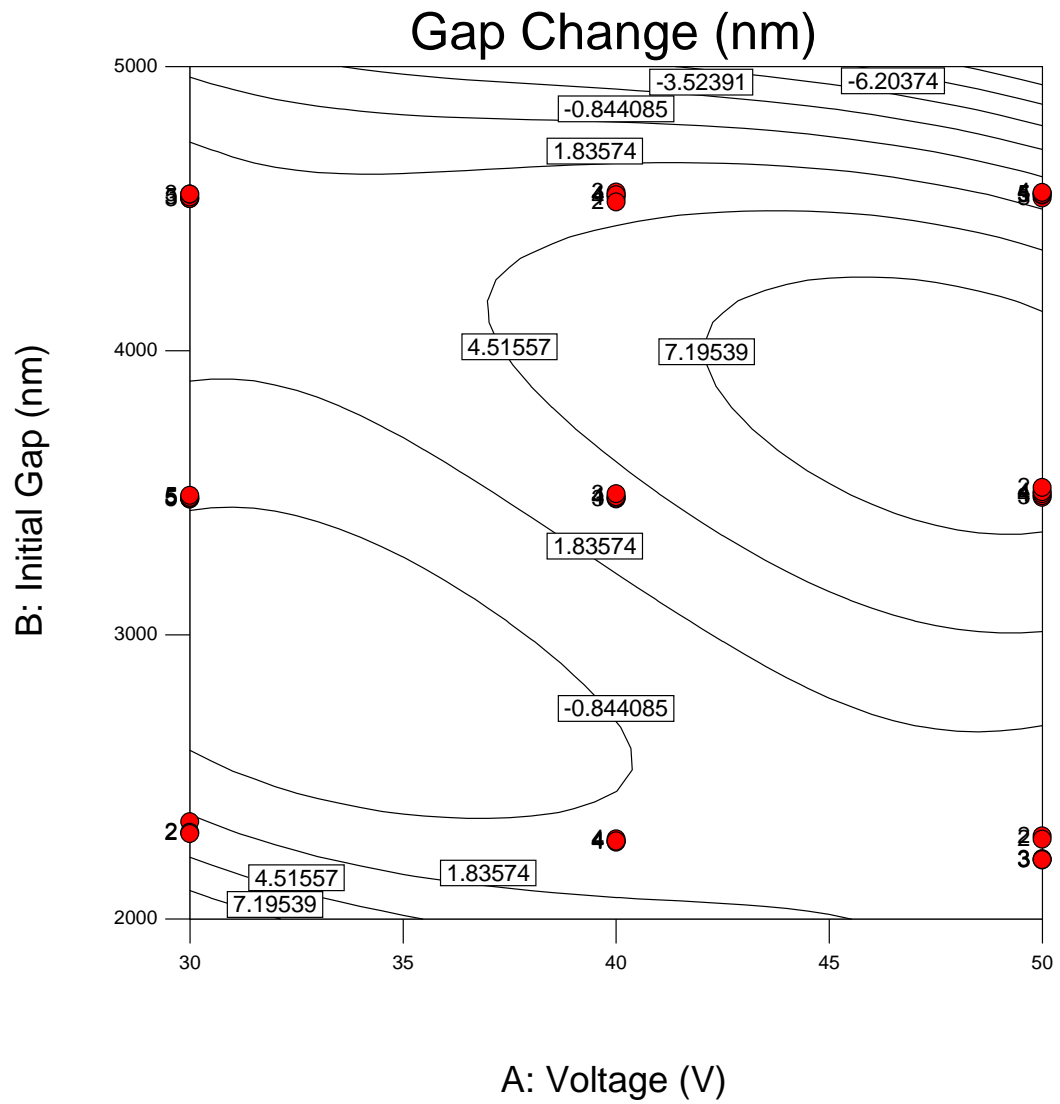


Figure 9.6: Response surface from the large gap, high voltage experiment for gap change with voice coil compensation

The fit equation for the voice coil on condition is

$$\begin{aligned}
G = & 576.5753 \\
& - 22.2315V \\
& - 0.2769G_i \\
& + .004159VG_i \\
& + 0.39453V^2 \\
& + 5.984 \times 10^{-5}G_i^2 \\
& - 1.4 \times 10^{-5}V^2G_i \\
& - 4.4 \times 10^{-7}VG_i^2 \\
& - .002889 \times 10^{-3}V^3 \\
& - 4.2 \times 10^{-9}G_i^3
\end{aligned} \tag{9.2}$$

Figure 9.7 shows the gap change predicted by the fit model versus the actual measured gap change. The X axis is the measured gap change and the Y axis is the gap change predicted by the statistical model. If the model represents the data, the predicted and measured gap changes should be the same, resulting in the the actual versus predicted points lying on the line $X = Y$. Figure biggpred shows the actual versus predicted results for the big gap experiment. The points do lie on the line $X = Y$, as they should for a good model. Figure 9.7 includes both the voice coil on and voice coil off conditions. The ANOVA results and more statistical diagnostic plots are included in the appendix.

The large gap, high voltage experiment shows that voice coil compen-

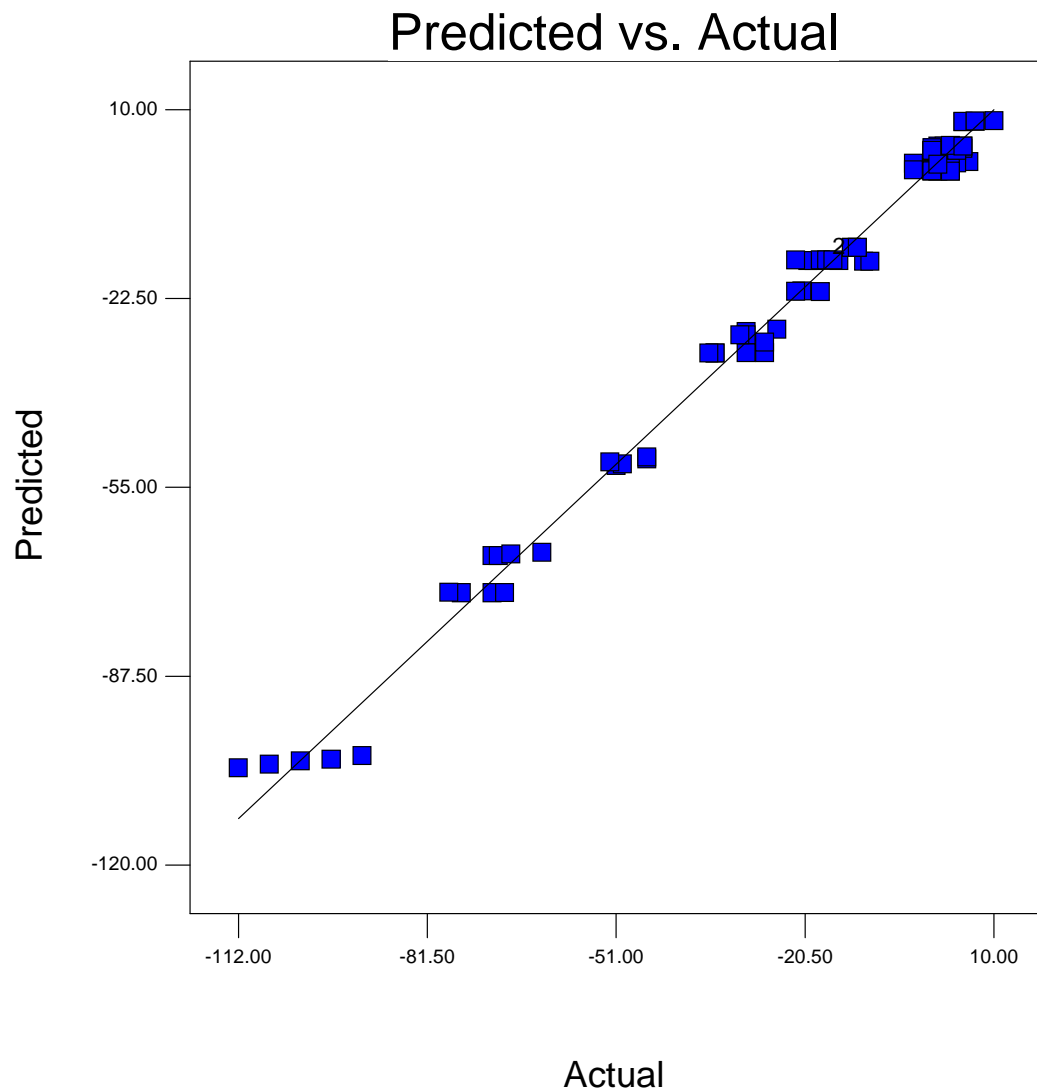


Figure 9.7: Predicted Gap Change versus measured Gap Change for the large gap, high voltage experiment. If the model predicts the value measured in the experiment, the predicted vs actual value will lie on the solid line in the graph. Values clustered along the line indicate a good statistical fit.

sation can nearly eliminate the gap change caused by the electrostatic force. The range of gap change is twice the uncertainty of the gap measurement, $\pm 3\text{nm}$. Over much of the response surface, the predicted value of gap change is much less than the uncertainty of the gap measurement.

Figure 9.8 shows the applied force vs. gap change of the new active gap tool with and without voice coil compensation. Without voice coil compensation, the tool has an apparent stiffness that varies from less than $1\text{N}/\mu\text{m}$ to $3\text{N}/\mu\text{m}$. With voice coil compensation, the stiffness is ill defined. The gap changes by less than $\pm 8\text{nm}$. The gap change is less than $\pm 3\text{nm}$ over much of the operating range. Depending on the process conditions, the tool appears to have a stiffness of anywhere from $30\text{N}/\mu\text{m}$, increasing to near infinite and passing into negative stiffness. With the success of voice coil compensation at large gaps, the experiment was repeated at small gaps with lower voltages.

9.2.2.2 Small Gap, Low Voltage

For the small gap experiment, the gap values chosen were 500, 1000, and 1500nm and the voltages were 10, 20, and 30V. Each process condition was repeated 5 times. The experimental initial gaps ranged $\pm 150\text{nm}$ from the design conditions. The R^2 statistic was 0.71 and the adequate predictor statistic was 18. These are not as high as the results of the large gap experiment, but they are sufficient to give highly significant fits. The graph of actual versus predicted values (figure 9.9) appears to show the data scattered more than the results of the large gap experiment. A look at the scale, however,

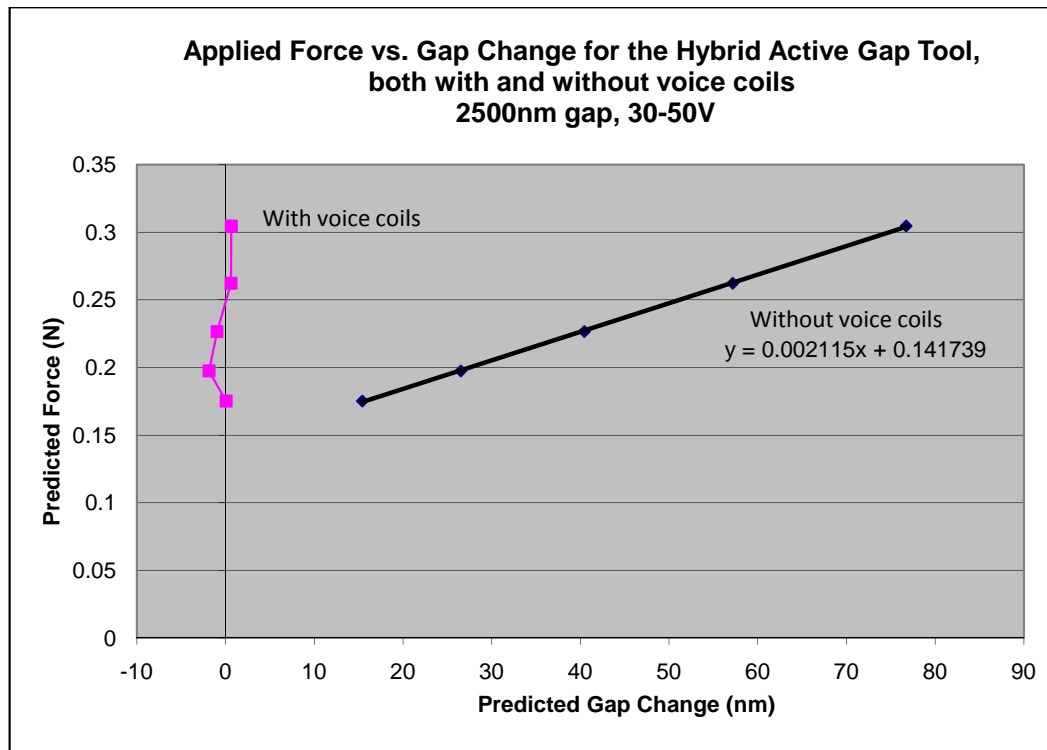


Figure 9.8: Applied force vs. gap change for the Hybrid Active Gap Tool. The gap change and force are predicted from the statistical models for the large gap experiment. The line to the right is the predicted gap change and force without the voice coils and the line on the left is the predicted response with the voice coils. The gap change predicted with the voice coils engaged is near zero and does not fall on a line. The gap change is never greater than 5 nm. This is the expected result if the force compensation is nearly perfect.

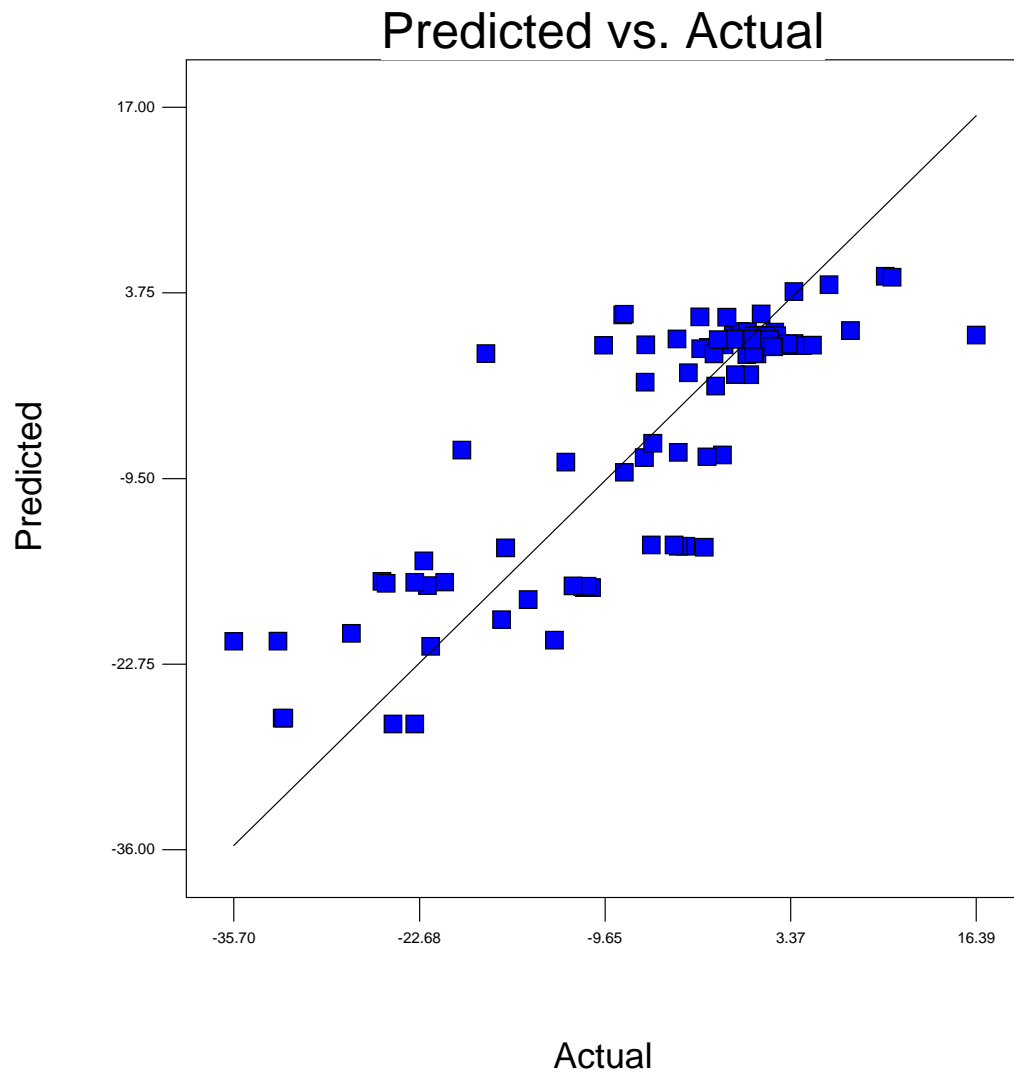


Figure 9.9: Predicted Gap Change versus measured Gap Change for the small gap, low voltage experiment. If the model predicts the value measured in the experiment, the predicted vs actual value will lie on the solid line in the graph. Values clustered along the line indicate a good statistical fit.

shows that the absolute deviation from the ideal line is the same as for the large gap experiment, but the range of gap change is smaller, so the graphs appears to be worse. The gap changes measured in the small gap experiment are smaller, but are a larger percentage of the total gap, so the noise results in a lower R^2 value.

The model that provided the best fit to the data was a two factor interaction model. The contour plot for the voice coil off condition is shown in figure 9.10. The gap change behaves as it did in the large gap experiment, with the gap shrinking more as the initial gap shrinks and the voltage rises. The largest value of gap change is 27nm. The equation for the voice coil off condition is

$$\begin{aligned}
 F = & -22.9604 \\
 & -0.26328V \\
 & +0.020407G_i \\
 & -3.86605 \times 10^{-4}VG_i
 \end{aligned} \tag{9.3}$$

The results of the voice coil compensation are shown in figure 9.11. The gap change ranges from 3nm shrinkage to 5nm expansion. As in the large gap experiment, the range of gap change predicted from the statistical fit is less than the ± 3 nm uncertainty in the gap measurement over much of the range.

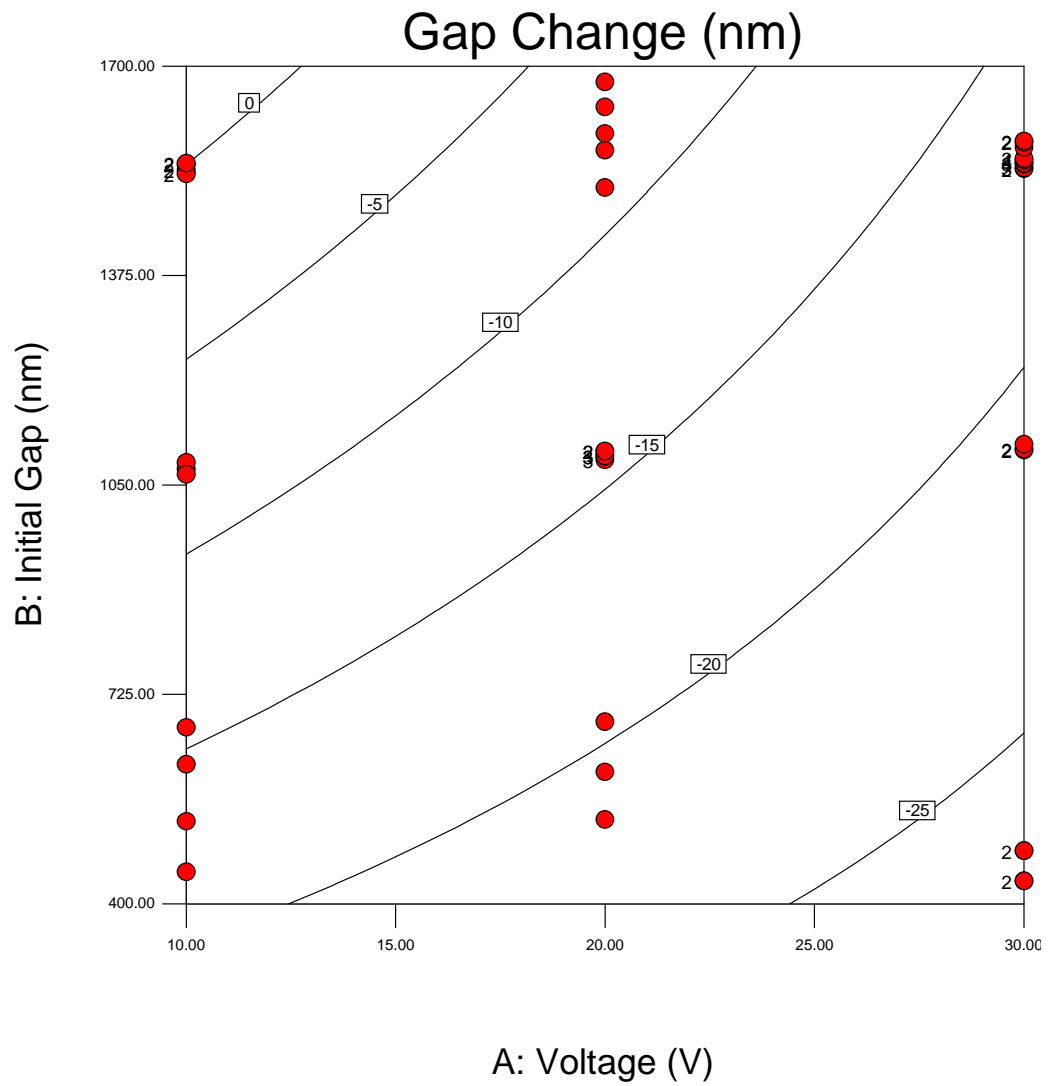


Figure 9.10: Gap Change for the small gap, low voltage experiment without voice coil compensation

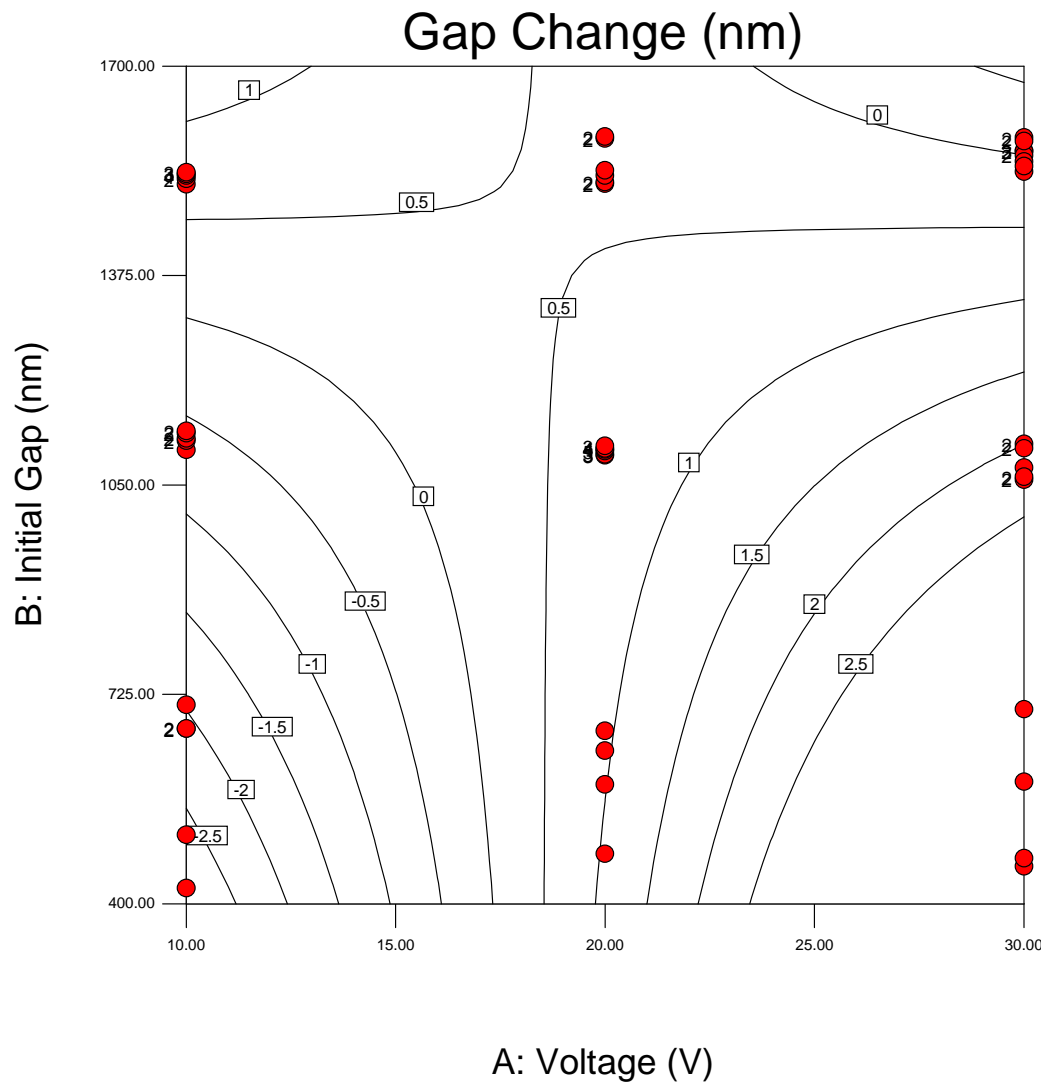


Figure 9.11: Gap Change for the small gap, low voltage experiment with voice coil compensation

The fit equation for the voice coil on condition is

$$\begin{aligned}
F = & -9.92432 \\
& + 0.56254V \\
& + 7.149 \times 10^{-3}G_i \\
& - 3.86605 \times 10^{-4}VG_i
\end{aligned} \tag{9.4}$$

Much of the observed gap change can not be distinguished from the noise in the gap measurement. The full ANOVA results and the results of the force analysis are included in the appendix. The applied force vs. gap change at small gaps is graphed in figure 9.12. As in the large gap experiment, without voice coil compensation the tool has very low stiffness and with voice coil compensation the gap changes less than 5nm. The model results for a gap of 1000nm shows gap change decreasing as the applied force increases. Over the entire range of gaps and voltages investigated, the apparent stiffness varies from about 30N/ μ m to infinite stiffness, and into negative stiffness.

9.3 Conclusions

Voice coil compensation has taken a machine with a stiffness of 3N/ μ m and compensated for the applied electrical force so that the tool behaves as if it is much stiffer. Voice coil compensation corrects for the electric field force and enables the tool to meet the specification of not moving more than 5nm when the electric field is applied. Gaps as small as 400nm have been held constant while the electric field was applied. Smaller gaps can be achieved with improvements in machine precision capability and calibration of tool flatness.

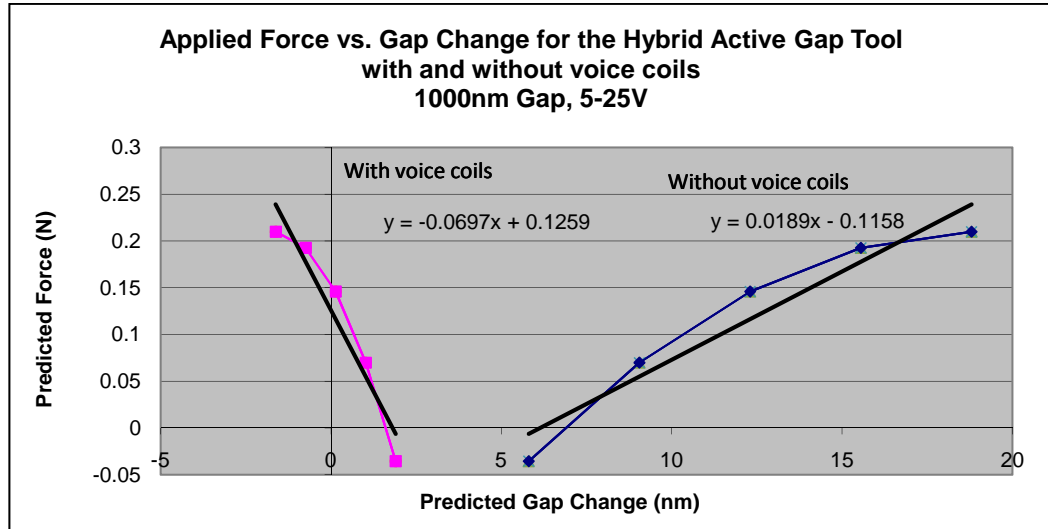


Figure 9.12: Applied force vs. gap change for the Hybrid Active Gap Tool. The gap change and force are predicted from the statistical models for the small gap experiment. The line to the right is the predicted gap change and force without the voice coils and the line on the left is the response predicted with the voice coils. The gap change predicted with the voice coils engaged has a negative slope, indicating that the tool behaves as if it has a high negative stiffness (a positive force results in a negative displacement). This indicates that at a gap of 1000nm and a voltage range from 5-20V the tool sometimes overcompensates slightly. The force compensation is again nearly perfect, with displacement never exceeding 5nm.

Chapter 10

Conclusions and Recommendations

The Hybrid Active Gap Tool meets the motion control specifications defined for a pillar formation tool. The 3-RPS mechanism with micrometer and piezo actuation satisfactorily controls the parallelism of the template and wafer. Voice coil compensation corrects for the applied electrical force, as long as the template surface geometry is characterized to less than 50nm. Gap control experiments showed that voice coil compensation reduced gap change to less than 5nm. At smaller gaps ($\approx 500\text{nm}$) the gap change was less than 3nm.

The contributions of this dissertation are as follows:

1. 3-RPS mechanism design for hybrid actuation capability
2. HAGT control for achieving high apparent stiffness and high resolution positioning
3. High frequency gap sensing technique ($\approx 10\times$ faster than the apparatus presented in the literature) as required by the control system

There are several areas where this technology can be further improved. The first is that the tool proved very sensitive to side loads, manufacturing

tolerances, assembly misalignments, and micrometer motor controller malfunctions. Better understanding of the internal loading of the mechanism will lead to more robust mechanical designs. The piezo actuators are especially sensitive to internal loads. The options to resolve this issue are to switch to kinematics that do not place side loads on the actuators or to select actuators that are insensitive to side loads. Piezo crawler motors are one option that have both the long travel and high motion resolution necessary and are immune to side loads. Other tip/tilt/Z mechanisms are available, but they are generally designed for low stiffness applications.

The minimum achievable gap is controlled by the flatness of the template and wafer and their support structures. Smaller gaps can be achieved with improved template flatness and geometric characterization. Mask blanks being developed for Extreme UV lithography will have a flatness of $<50\text{nm}$ over a 150mm circle on both the front and back sides. These mask blanks will provide flatter template blanks than are available now. Flatter templates, along with better geometric characterization of all the components in the template/wafer stack, will allow for sub- 100nm gaps.

Sub- 100nm gaps need to be investigated for nanometer scale pillar formation. As the gap between the template and wafer decreases, arcing from the sharp corner at the edge of the active area of the template becomes both more likely and more unpredictable. Development of templates that are resistant to arcing is necessary for pillar formation at sub 100nm gaps.

The force compensation scheme investigated in this dissertation only

compensates for the electric field force. Fluid forces in the pillar formation process are also significant. These forces can be added to the feedforward compensation scheme. Compensation of all predictable forces will further improve the gap control during pillar formation and reduce the need for a high stiffness mechanism.

Faster computer and optical hardware will improve the bandwidth of the tool and facilitate further experiments to characterize the forces and motion produced by different templates. Voice coil compensation can then be further refined.

In summary, piezoelectric actuation with feedforward voice coil compensation improved the performance of the Hybrid Active Gap Tool, reducing the need for high static stiffness and allowing a compliant tool to meet the stringent requirements for sub- $0.5\mu\text{m}$ gap control in the presence of electric fields.

Appendices

Appendix A

Results of Gap Control Experiments

Response 2 force

ANOVA for Response Surface Reduced Cubic Model

Analysis of variance table [Partial sum of squares - Type III]

Source	Sum of Squares	df	Mean Square	F Value	p-value Prob > F	
Model	9.082888	13	0.698684	3960.726	< 0.0001	significant
A-Voltage	0.133506	1	0.133506	756.8264	< 0.0001	
B-Initial Gap	0.004427	1	0.004427	25.09862	< 0.0001	
C-Voice Coil	0.962289	1	0.962289	5455.063	< 0.0001	
AB	0.049089	1	0.049089	278.2798	< 0.0001	
AC	0.84199	1	0.84199	4773.107	< 0.0001	
BC	0.212531	1	0.212531	1204.803	< 0.0001	
A^2	2.37E-06	1	2.37E-06	0.013421	0.9081	
B^2	0.00137	1	0.00137	7.764173	0.0068	
ABC	0.016081	1	0.016081	91.15859	< 0.0001	
A^2C	0.002224	1	0.002224	12.60748	0.0007	
AB^2	0.002615	1	0.002615	14.82376	0.0003	
B^2C	0.006787	1	0.006787	38.47533	< 0.0001	
B^3	0.00049	1	0.00049	2.776713	0.1000	
Residual	0.012701	72	0.000176			
Lack of Fit	0.011805	65	0.000182	1.419568	0.3318	not significant
Pure Error	0.000896	7	0.000128			
Cor Total	9.095589	85				

The Model F-value of 3960.73 implies the model is significant. There is only a 0.01% chance that a "Model F-Value" this large could occur due to noise.

Values of "Prob > F" less than 0.0500 indicate model terms are significant.

In this case A, B, C, AB, AC, BC, B2, ABC, A2C, AB2, B2C are significant model terms.

Values greater than 0.1000 indicate the model terms are not significant.

If there are many insignificant model terms (not counting those required to support hierarchy), model reduction may improve your model.

The "Lack of Fit F-value" of 1.42 implies the Lack of Fit is not significant relative to the pure error. There is a 33.18% chance that a "Lack of Fit F-value" this large could occur due to noise. Non-significant lack of fit is good -- we want the model to fit.

Std. Dev.	0.013282	R-Squared	0.998604
Mean	0.11795	Adj R-Squared	0.998351
C.V. %	11.26043	Pred R-Squared	0.998002
PRESS	0.018176	Adeq Precision	215.0391

The "Pred R-Squared" of 0.9980 is in reasonable agreement with the "Adj R-Squared" of 0.9984.

"Adeq Precision" measures the signal to noise ratio. A ratio greater than 4 is desirable. Your ratio of 215.039 indicates an adequate signal. This model can be used to navigate the design space.

Factor	Coefficient Estimate	df	Standard Error	95% CI Low	95% CI High	VIF
--------	----------------------	----	----------------	------------	-------------	-----

Table A.1: ANOVA for force response of large gap experiment

Intercept	0.129302	1	0.003236	0.122852	0.135753	
A-Voltage	0.07667	1	0.002787	0.071114	0.082225	3.772849
B-Initial Gap	-0.07614	1	0.015197	-0.10643	-0.04584	78.47037
C-Voice Coil	0.238128	1	0.003224	0.231701	0.244555	5.056764
AB	-0.04222	1	0.002531	-0.04727	-0.03718	1.970404
AC	0.134564	1	0.001948	0.130681	0.138446	1.873787
BC	-0.07892	1	0.002274	-0.08345	-0.07439	1.762042
A^2	-0.00029	1	0.002508	-0.00529	0.00471	3.698755
B^2	0.008683	1	0.003116	0.002471	0.014894	1.762001
ABC	-0.02341	1	0.002452	-0.0283	-0.01852	1.800255
A^2C	0.008937	1	0.002517	0.003919	0.013954	6.588211
AB^2	0.012996	1	0.003375	0.006267	0.019724	4.078179
B^2C	0.019248	1	0.003103	0.013062	0.025433	4.013982
B^3	0.02126	1	0.012759	-0.00417	0.046694	88.42343

Final Equation in Terms of Coded Factors:

$$\begin{aligned}
 \text{force} = & 0.129302 \\
 & 0.07667 * A \\
 & -0.07614 * B \\
 & 0.238128 * C \\
 & -0.04222 * A * B \\
 & 0.134564 * A * C \\
 & -0.07892 * B * C \\
 & -0.00029 * A^2 \\
 & 0.008683 * B^2 \\
 & -0.02341 * A * B * C \\
 & 0.008937 * A^2 * C \\
 & 0.012996 * A * B^2 \\
 & 0.019248 * B^2 * C \\
 & 0.02126 * B^3
 \end{aligned}$$

Final Equation in Terms of Actual Factors:

$$\begin{aligned}
 \text{Voice Coil} & -1 \\
 \text{force} = & -1.97574 \\
 & 0.024096 * \text{Voltage} \\
 & 0.001297 * \text{Initial Gap} \\
 & -1.1\text{E-}05 * \text{Voltage} * \text{Initial Gap} \\
 & -9.2\text{E-}05 * \text{Voltage}^2 \\
 & -2.9\text{E-}07 * \text{Initial Gap}^2 \\
 & 1.3\text{E-}09 * \text{Voltage} * \text{Initial Gap}^2 \\
 & 2.13\text{E-}11 * \text{Initial Gap}^3
 \end{aligned}$$

Table A.2: ANOVA for force response of large gap experiment, cont.

Voice Coil	1
force	=
-1.92149	
0.053097	* Voltage
0.001057	* Initial Gap
-1.6E-05	* Voltage * Initial Gap
8.65E-05	* Voltage^2
-2.5E-07	* Initial Gap^2
1.3E-09	* Voltage * Initial Gap^2
2.13E-11	* Initial Gap^3

Table A.3: ANOVA for force response of large gap experiment, cont.

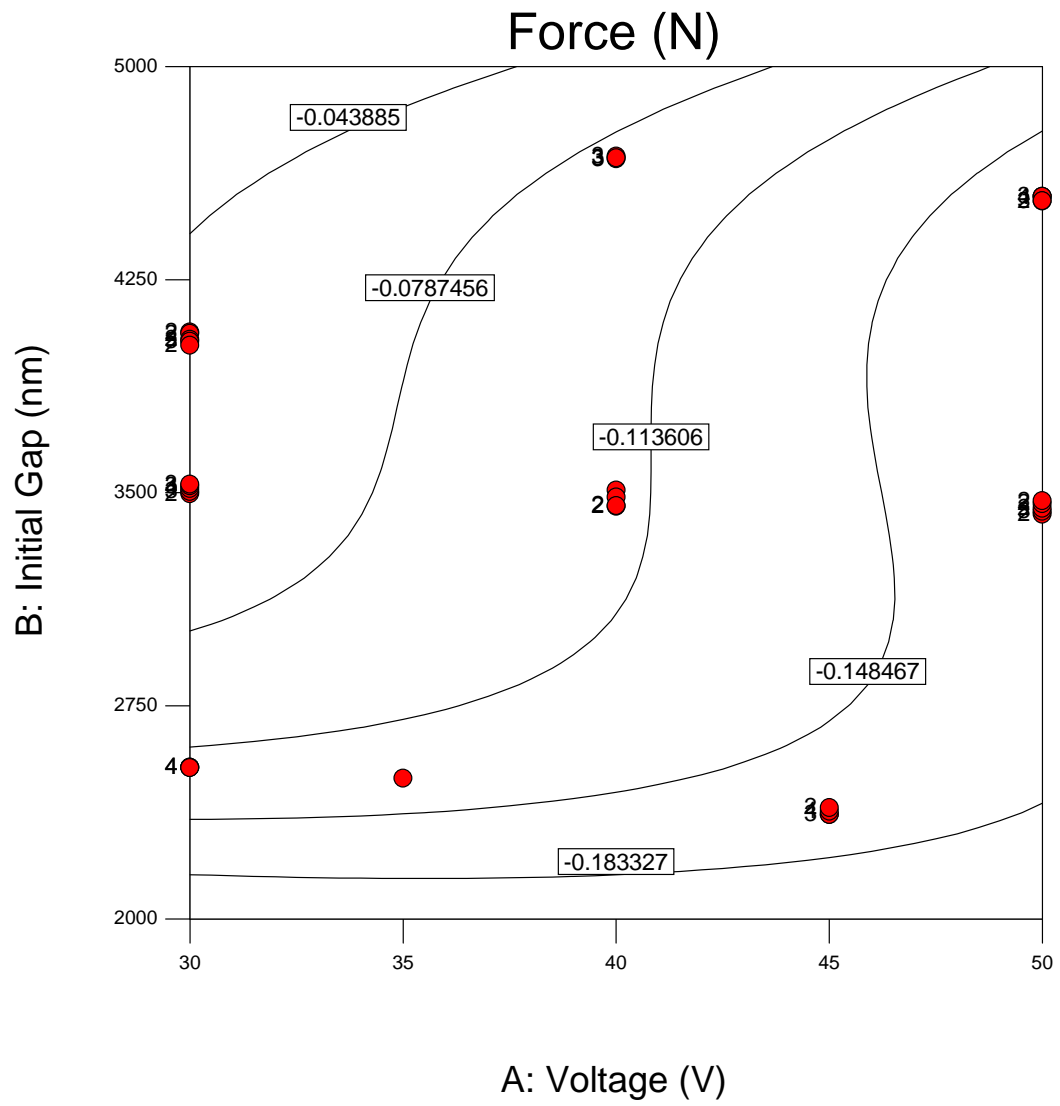


Figure A.1: Response surface for measured force without voice coil compensation, large gap experiment

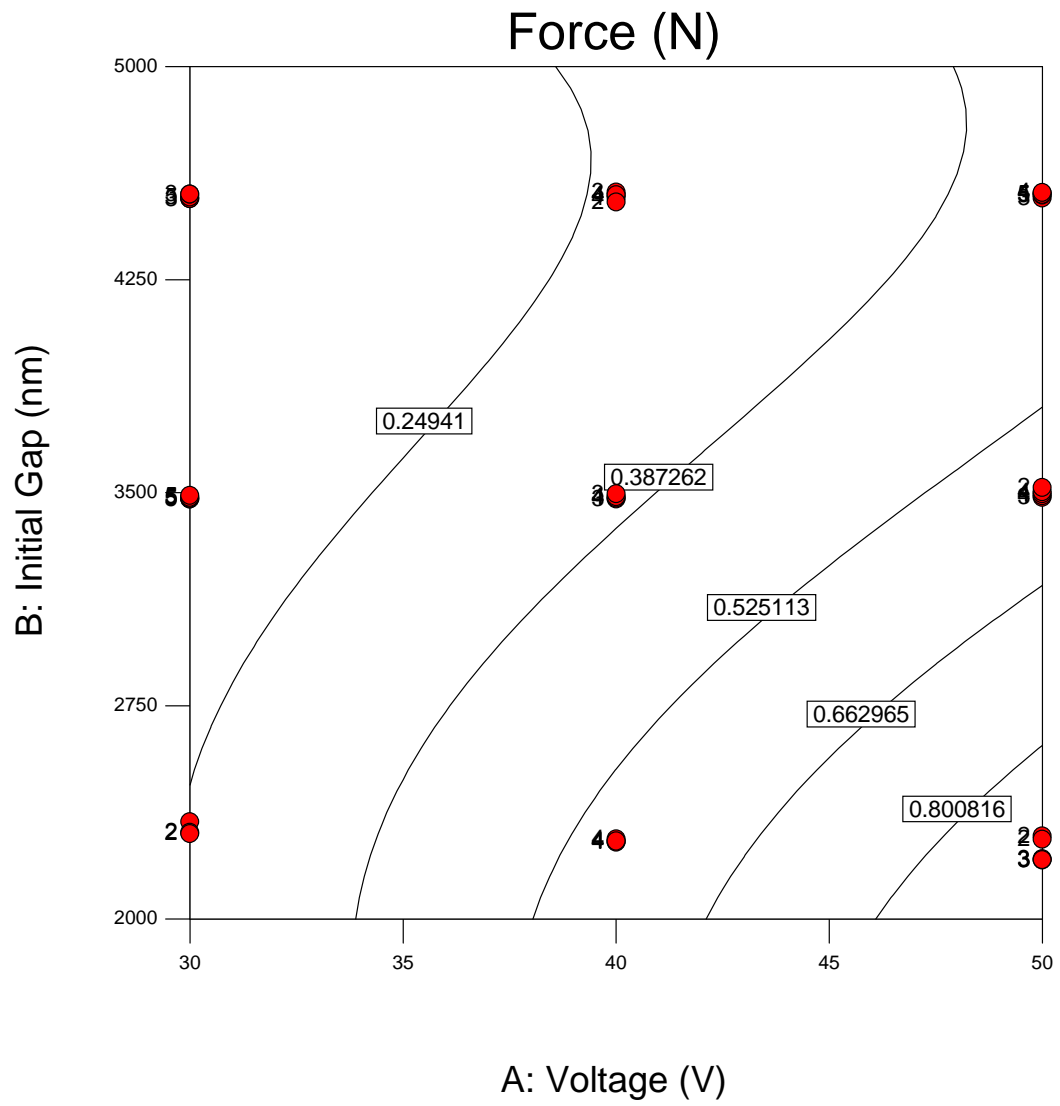


Figure A.2: Response surface for measured force with voice coil compensation, large gap experiment

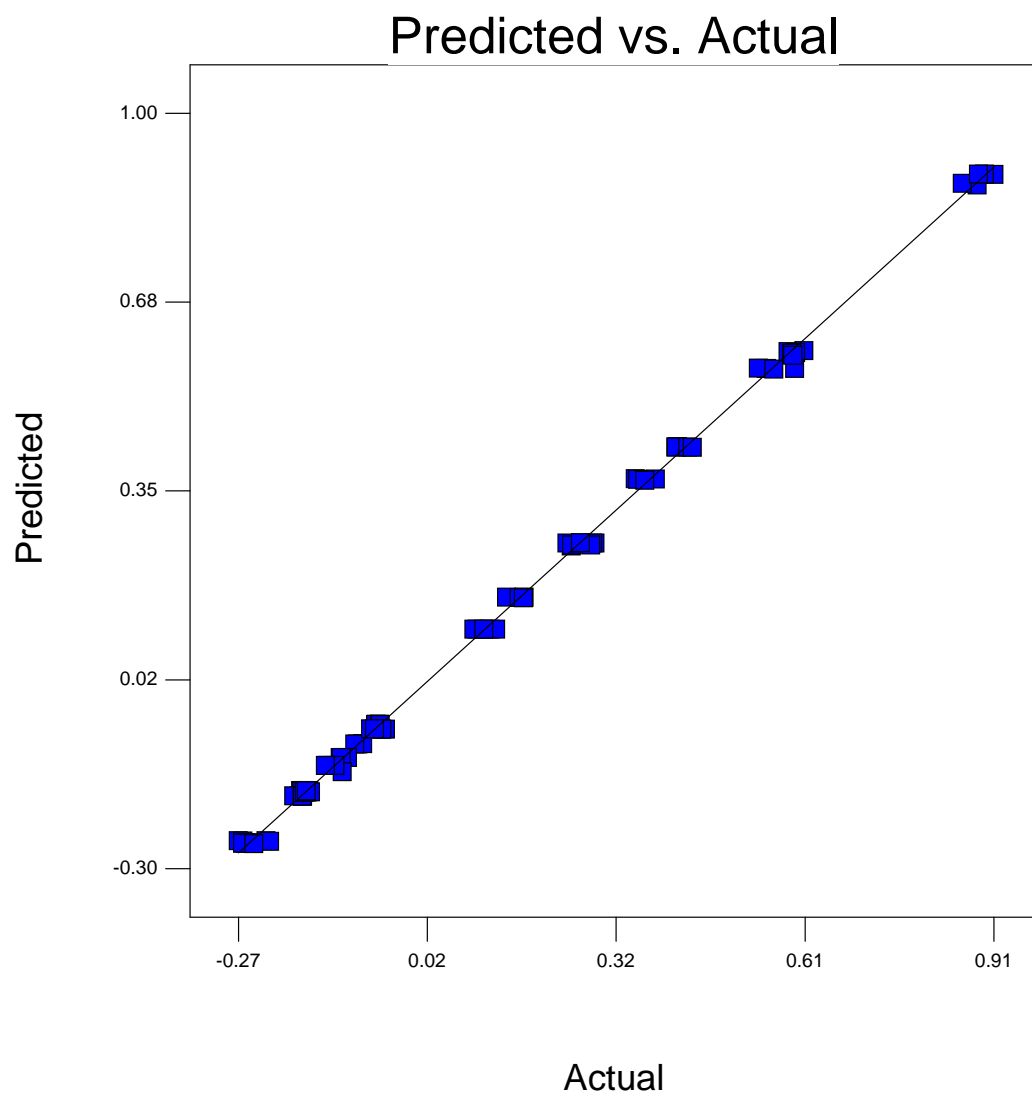


Figure A.3: Predicted versus actual values for force response, large gap experiment

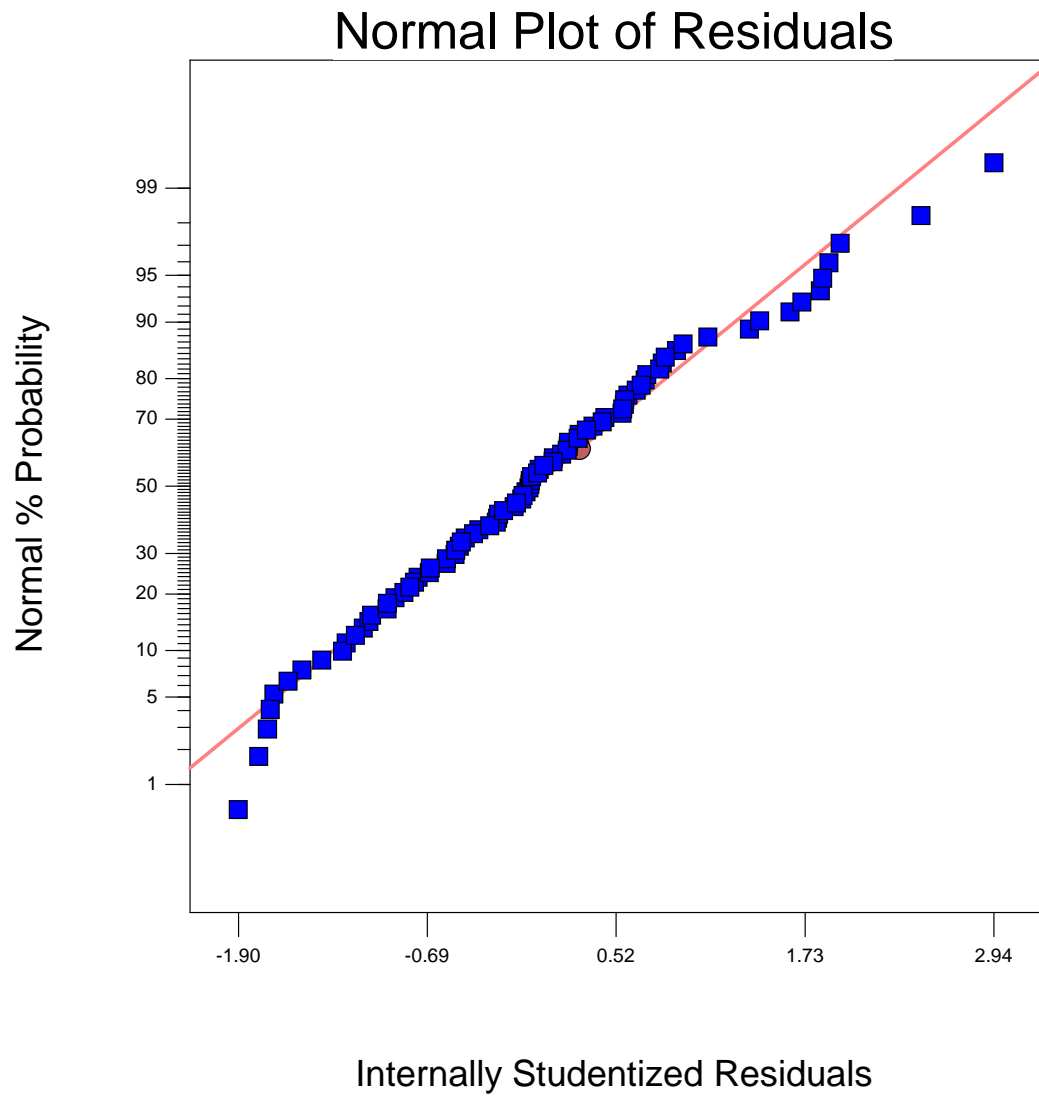


Figure A.4: Normalized residuals of force response, large gap experiment

Response 1 gap Change						
ANOVA for Response Surface Cubic Model						
Analysis of variance table [Partial sum of squares - Type III]						
Source	Sum of Squares	df	Mean Square	F Value	p-value Prob > F	
Model	80390.55	15	5359.37	483.9069	< 0.0001	significant
A-Voltage	72.37693	1	72.37693	6.53504	0.0127	
B-Initial Gap	57.1349	1	57.1349	5.158811	0.0262	
C-Voice Coil	2849.118	1	2849.118	257.2519	< 0.0001	
AB	772.6101	1	772.6101	69.76032	< 0.0001	
AC	4499.457	1	4499.457	406.2638	< 0.0001	
BC	766.3695	1	766.3695	69.19684	< 0.0001	
A^2	53.76332	1	53.76332	4.854384	0.0309	
B^2	189.9659	1	189.9659	17.15235	< 0.0001	
ABC	1229.587	1	1229.587	111.0216	< 0.0001	
A^2B	33.78729	1	33.78729	3.050713	0.0851	
A^2C	48.89294	1	48.89294	4.414629	0.0392	
AB^2	269.6026	1	269.6026	24.34289	< 0.0001	
B^2C	28.67558	1	28.67558	2.589169	0.1121	
A^3	88.76596	1	88.76596	8.014835	0.0061	
B^3	11.13011	1	11.13011	1.004958	0.3196	
Residual	775.2646	70	11.07521			
Lack of Fit	763.0979	63	12.11267	6.968931	0.0058	significant
Pure Error	12.16667	7	1.738095			
Cor Total	81165.81	85				

The Model F-value of 483.91 implies the model is significant. There is only a 0.01% chance that a "Model F-Value" this large could occur due to noise.

Values of "Prob > F" less than 0.0500 indicate model terms are significant.

In this case A, B, C, AB, AC, BC, A², B², ABC, A²C, AB², A³ are significant model terms.

Values greater than 0.1000 indicate the model terms are not significant.

If there are many insignificant model terms (not counting those required to support hierarchy), model reduction may improve your model.

The "Lack of Fit F-value" of 6.97 implies the Lack of Fit is significant. There is only a 0.58% chance that a "Lack of Fit F-value" this large could occur due to noise.

Significant lack of fit is bad -- we want the model to fit.

Std. Dev.	3.327944	R-Squared	0.990448
Mean	-21.0465	Adj R-Squared	0.988402
C.V. %	15.81233	Pred R-Squared	0.985504
PRESS	1176.541	Adeq Precision	77.55637

The "Pred R-Squared" of 0.9855 is in reasonable agreement with the "Adj R-Squared" of 0.9884.

"Adeq Precision" measures the signal to noise ratio. A ratio greater than 4 is desirable. Your ratio of 77.556 indicates an adequate signal. This model can be used to navigate the design space.

Table A.4: ANOVA for gap response of large gap experiment

Factor	Coefficient Estimate	df	Standard Error	95% CI Low	95% CI High	VIF
Intercept	-12.0693	1	1.008199	-14.0801	-10.0585	
A-Voltage	-3.24156	1	1.268032	-5.77057	-0.71255	12.44036
B-Initial Gap	12.01223	1	5.2887	1.464253	22.56021	151.3676
C-Voice Coil	15.89241	1	0.990856	13.91621	17.86861	7.607237
AB	7.11028	1	0.8513	5.412416	8.808144	3.550432
AC	10.37106	1	0.51454	9.344839	11.39727	2.082848
BC	-5.32548	1	0.6402	-6.60232	-4.04864	2.225156
A^2	-2.26715	1	1.028996	-4.31942	-0.21488	9.913137
B^2	-3.60689	1	0.870906	-5.34386	-1.86993	2.192312
ABC	-7.58299	1	0.719676	-9.01834	-6.14764	2.470402
A^2B	-1.38986	1	0.79574	-2.97692	0.197191	6.309487
A^2C	2.186272	1	1.040536	0.110989	4.261556	17.93482
AB^2	-4.42061	1	0.895975	-6.20757	-2.63364	4.576931
B^2C	1.28817	1	0.800558	-0.30849	2.884833	4.25541
A^3	-2.88912	1	1.020511	-4.92446	-0.85377	53.64525
B^3	-4.23661	1	4.226147	-12.6654	4.192174	154.5268

Final Equation in Terms of Coded Factors:

$$\begin{aligned}
 \text{gap Change} = & -12.0693 \\
 & -3.24156 * A \\
 & 12.01223 * B \\
 & 15.89241 * C \\
 & 7.11028 * A * B \\
 & 10.37106 * A * C \\
 & -5.32548 * B * C \\
 & -2.26715 * A^2 \\
 & -3.60689 * B^2 \\
 & -7.58299 * A * B * C \\
 & -1.38986 * A^2 * B \\
 & 2.186272 * A^2 * C \\
 & -4.42061 * A * B^2 \\
 & 1.28817 * B^2 * C \\
 & -2.88912 * A^3 \\
 & -4.23661 * B^3
 \end{aligned}$$

Table A.5: ANOVA for gap response of large gap experiment, cont.

Final Equation in Terms of Actual Factors:

Voice Coil	-1
gap Change	=
701.2834	
-26.1158	* Voltage
-0.30888	* Initial Gap
0.005676	* Voltage * Initial Gap
0.350805	* Voltage^2
5.73E-05	* Initial Gap^2
-1.4E-05	* Voltage^2 * Initial Gap
-4.4E-07	* Voltage * Initial Gap^2
-0.00289	* Voltage^3
-4.2E-09	* Initial Gap^3

Voice Coil	1
gap Change	=
576.5753	
-22.2315	* Voltage
-0.2769	* Initial Gap
0.004159	* Voltage * Initial Gap
0.39453	* Voltage^2
5.98E-05	* Initial Gap^2
-1.4E-05	* Voltage^2 * Initial Gap
-4.4E-07	* Voltage * Initial Gap^2
-0.00289	* Voltage^3
-4.2E-09	* Initial Gap^3

Table A.6: ANOVA for gap response of large gap experiment, cont.

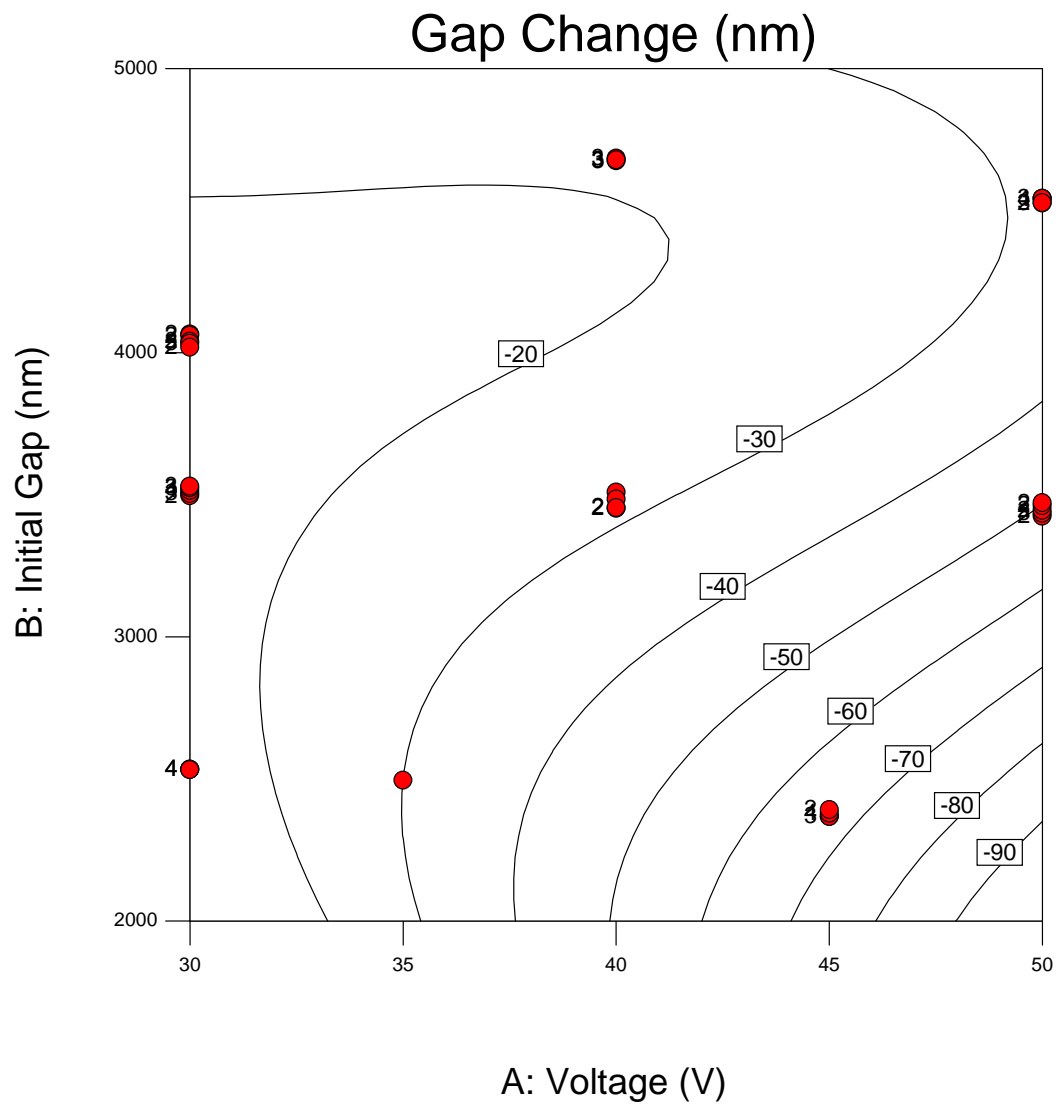


Figure A.5: Response surface for gap change without voice coil compensation, large gap experiment

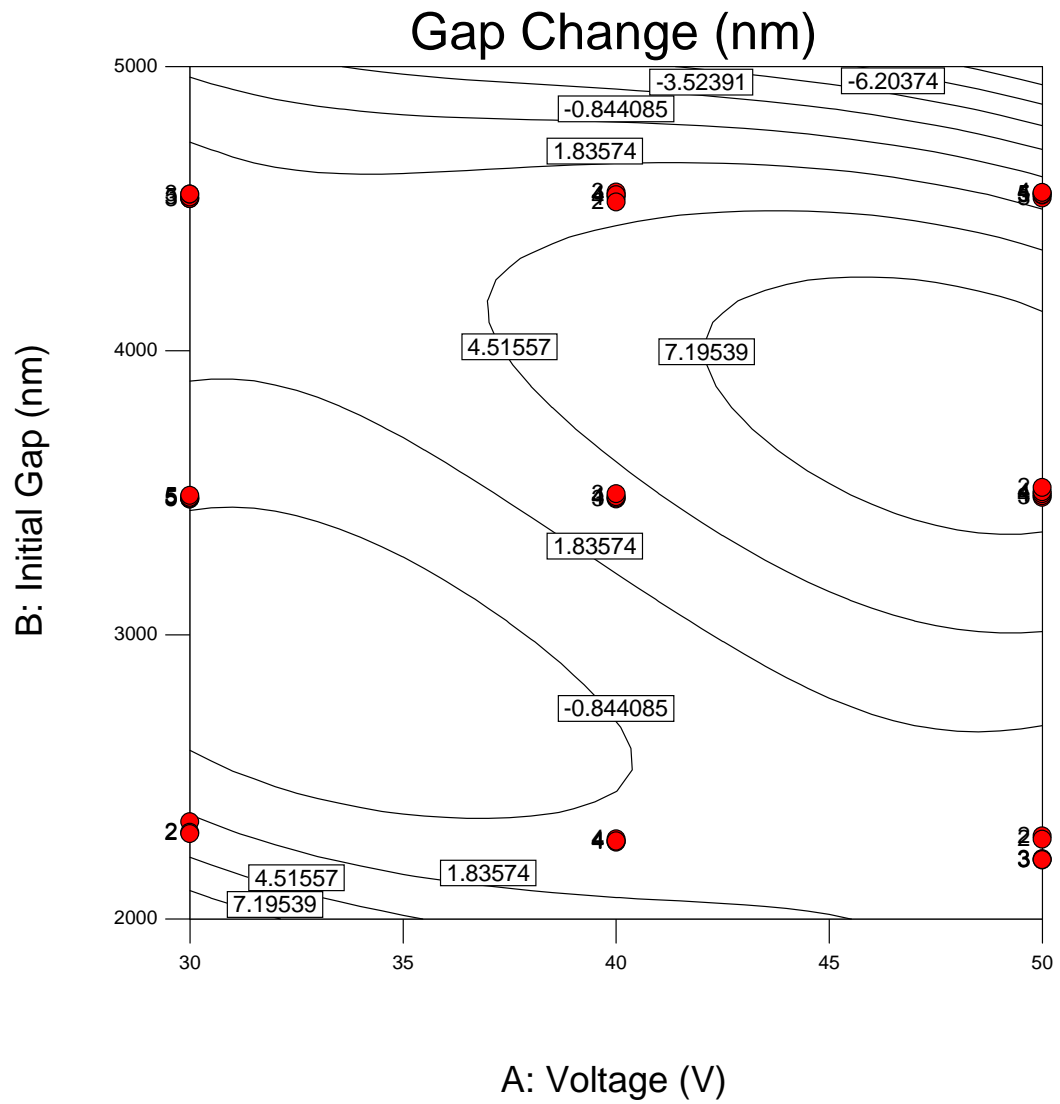


Figure A.6: Response surface for gap change with voice coil compensation, large gap experiment

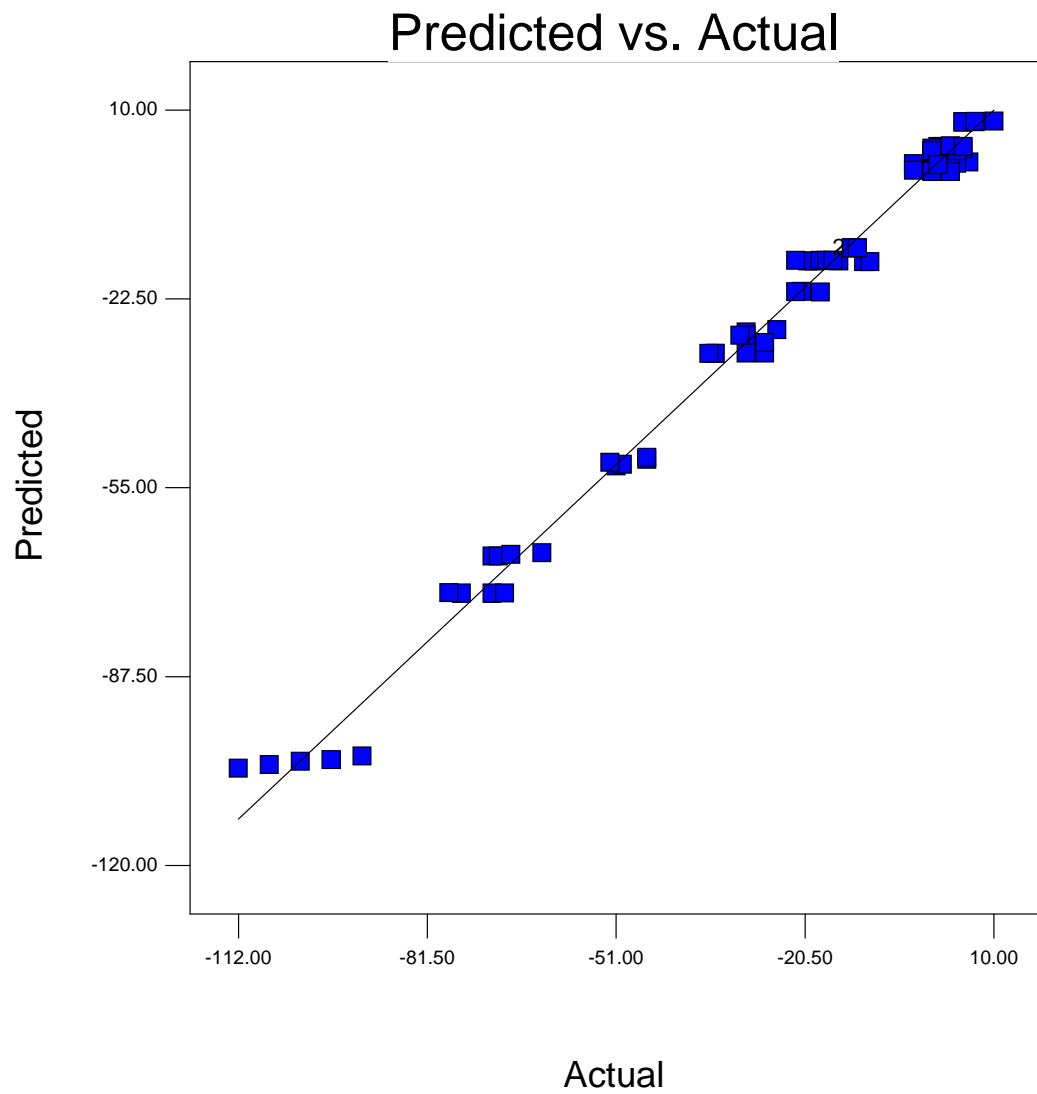


Figure A.7: Predicted response versus measured values for gap response, large gap experiment

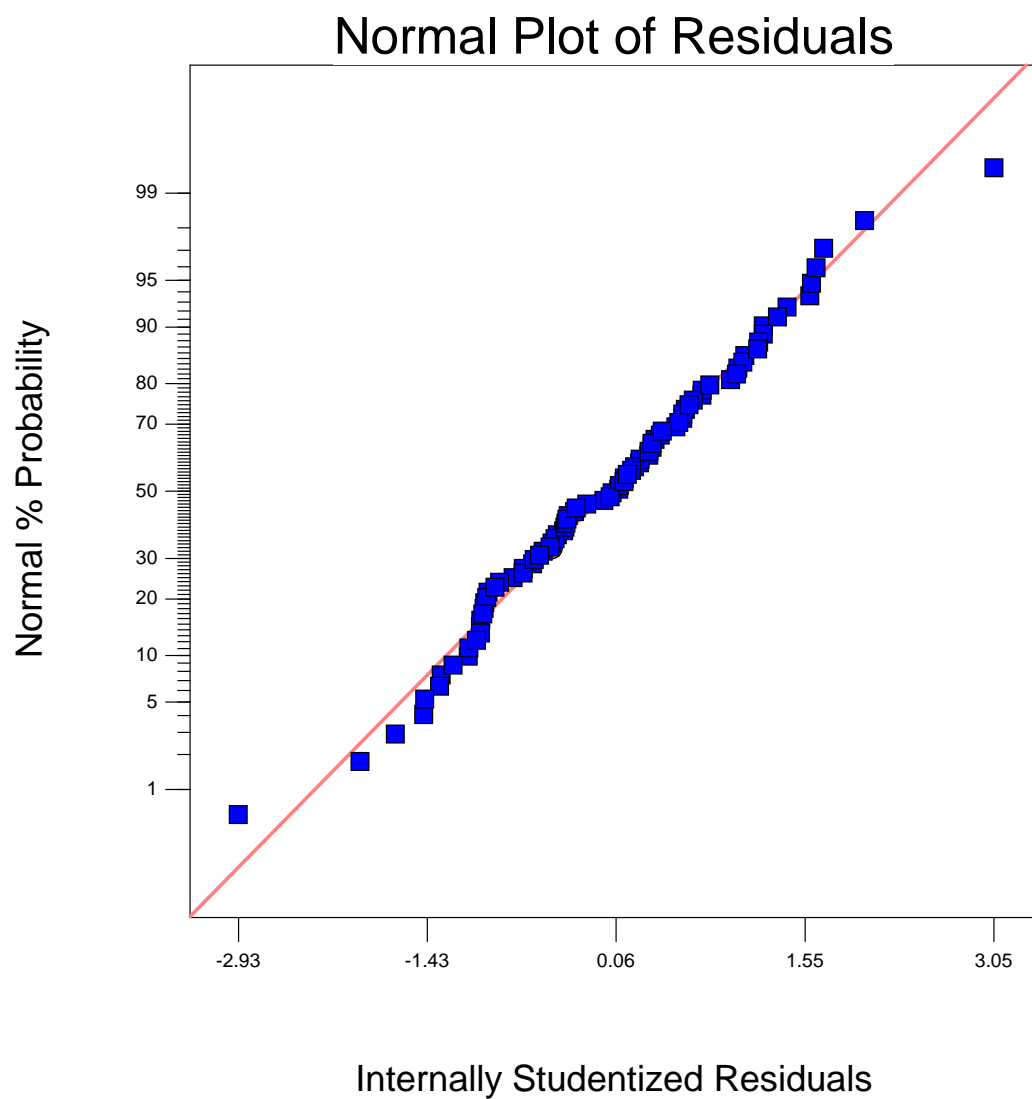


Figure A.8: Normalized residuals of gap response, large gap experiment

Voltage	Initial Gap (nm)	Voice Coil (On/off)	Gap Change (nm)	Force (N)
40	4675	-1	-21	-0.0863
40	4685	-1	-18	-0.0785
40	4678	-1	-22	-0.0908
60	4613	-1	-76	-0.2729
60	4612	-1	-71	-0.2296
60	4606	-1	-69	-0.2655
60	4595	-1	-78	-0.2238
30	4065	-1	-11	-0.0521
30	4060	-1	-10	-0.0571
30	4040	-1	-15	-0.0582
30	4033	-1	-19	-0.0518
30	4019	-1	-20	-0.0509
50	4543	-1	-35	-0.1689
50	4542	-1	-35	-0.1624
50	4543	-1	-36	-0.1753
50	4526	-1	-30	-0.174
50	4527	-1	-27	-0.1685
40	3509	-1	-25	-0.1092
40	3484	-1	-30	-0.1134
40	3452	-1	-30	-0.102
40	3454	-1	-31	-0.1121
60	3335	-1	-112	-0.2529
60	3349	-1	-107	-0.2628
60	3361	-1	-102	-0.2612
60	3367	-1	-97	-0.266
60	3382	-1	-92	-0.2487
50	3425	-1	-51	-0.1777
50	3434	-1	-50	-0.1862
50	3445	-1	-52	-0.1729
50	3461	-1	-46	-0.1726
50	3472	-1	-46	-0.1729
30	3497	-1	-18	-0.0431
30	3504	-1	-18	-0.0499
30	3515	-1	-17	-0.0485
30	3524	-1	-16	-0.066
30	3530	-1	-22	-0.0599
45	2367	-1	-71	-0.1697
45	2367	-1	-70	-0.1655
45	2379	-1	-68	-0.1601
45	2392	-1	-63	-0.1669
35	2495	-1	-27	-0.1105
30	2533	-1	-12	-0.1323
30	2532	-1	-13	-0.1351
30	2533	-1	-13	-0.1221
30	2533	-1	-12	-0.1367
30	2342	1	1	0.2476
40	2272	1	0	0.5523
50	2292	1	2	0.8815

Table A.7: Raw data from large gap experiment

30	3478	1	0	0.1464
40	3478	1	1	0.3473
50	3483	1	5	0.611
30	4534	1	4	0.1205
40	4547	1	2	0.2845
50	4537	1	6	0.4135
40	2270	1	2	0.5397
50	2280	1	-2	0.8585
30	3478	1	1	0.1738
40	3481	1	2	0.3788
50	3489	1	5	0.5862
30	4534	1	2	0.1004
40	4558	1	5	0.2811
50	4547	1	4	0.4106
40	2282	1	1	0.5639
50	2211	1	2	0.9075
30	3480	1	3	0.1657
40	3486	1	5	0.3511
50	3497	1	7	0.5977
30	4541	1	2	0.0954
40	4538	1	3	0.2406
50	4554	1	1	0.4112
30	2304	1	0	0.2477
40	2274	1	3	0.5966
50	2207	1	0	0.8927
30	3484	1	3	0.1733
50	3503	1	7	0.5919
30	4551	1	4	0.1294
40	4549	1	0	0.2615
50	4550	1	-3	0.4293
30	2300	1	0	0.2777
50	2208	1	-3	0.8836
30	3490	1	0	0.1726
40	3496	1	3	0.3622
50	3518	1	10	0.5935
30	4551	1	0	0.1106
40	4523	1	5	0.2615
50	4557	1	1	0.4363

Table A.8: Raw data from large gap experiment, cont.

Response	2 Force (N)					
ANOVA for Response Surface Quadratic Model						
Analysis of variance table [Partial sum of squares - Type III]						
	Sum of		Mean	F	p-value	
Source	Squares	df	Square	Value	Prob > F	
Model	8.612626	8	1.076578	75.12112	< 0.0001	
A-Voltage	0.791422	1	0.791422	55.22361	< 0.0001	
B-Initial G	0.472031	1	0.472031	32.93722	< 0.0001	
C-Voice Cr	4.781038	1	4.781038	333.6097	< 0.0001	
AB	0.172147	1	0.172147	12.01202	0.0009	
AC	2.012259	1	2.012259	140.4108	< 0.0001	
BC	0.873864	1	0.873864	60.97623	< 0.0001	
A^2	0.065148	1	0.065148	4.545862	0.0361	
B^2	0.08355	1	0.08355	5.829955	0.0181	
Residual	1.132167	79	0.014331			
Lack of Fit	1.128059	77	0.01465	7.132257	0.1306	
Pure Error	0.004108	2	0.002054			
Cor Total	9.744793	87				

The Model F-value of 75.12 implies the model is significant. There is only a 0.01% chance that a "Model F-Value" this large could occur due to noise.

Values of "Prob > F" less than 0.0500 indicate model terms are significant.
In this case A, B, C, AB, AC, BC, A ⁺⁺² +-, B ⁺⁺² +- are significant model terms.
Values greater than 0.1000 indicate the model terms are not significant.
If there are many insignificant model terms (not counting those required to support hierarchy), model reduction may improve your model.

The "Lack of Fit F-value" of 7.13 implies the Lack of Fit is not significant relative to the pure error. There is a 13.06% chance that a "Lack of Fit F-value" this large could occur due to noise. Non-significant lack of fit is good -- we want the model to fit.

Std. Dev.	0.119713	R-Squared	0.883818
Mean	0.13469	Adj R-Squa	0.872053
C.V. %	88.88024	Pred R-Squ	0.837797
PRESS	1.580631	Adeq Preci	33.09162

The "Pred R-Squared" of 0.8378 is in reasonable agreement with the "Adj R-Squared" of 0.8721.

"Adeq Precision" measures the signal to noise ratio. A ratio greater than 4 is desirable. Your ratio of 33.092 indicates an adequate signal. This model can be used to navigate the design space.

	Coefficient	Standard	95% CI	95% CI	
Factor	Estimate	Error	Low	High	VIF
Intercept	0.058514	1	0.027656	0.003466	0.113562
A-Voltage (0.124289	1	0.016725	0.090998	0.157579
					1.140747

Table A.9: ANOVA for force response of small gap experiment

B-Initial Ga	-0.09741	1	0.016973	-0.1312	-0.06363	1.187165
C-Voice Coi	0.250924	1	0.013738	0.22358	0.278269	1.149323
AB	-0.06544	1	0.018882	-0.10303	-0.02786	1.145989
AC	0.188283	1	0.015889	0.156655	0.21991	1.037613
BC	-0.12287	1	0.015735	-0.15419	-0.09155	1.14822
A^2	0.058675	1	0.02752	0.003898	0.113452	1.027485
B^2	0.062025	1	0.025688	0.010894	0.113157	1.212173

Final Equation in Terms of Coded Factors:

$$\begin{aligned} \text{Force (N)} = & 0.058514 \\ & 0.124289 * A \\ & -0.09741 * B \\ & 0.250924 * C \\ & -0.06544 * A * B \\ & 0.188283 * A * C \\ & -0.12287 * B * C \\ & 0.058675 * A^2 \\ & 0.062025 * B^2 \end{aligned}$$

Final Equation in Terms of Actual Factors:

$$\begin{aligned} \text{Voice Coil } -1 \\ \text{Force (N)} = & 0.105691 \\ & -0.01678 * \text{Voltage (V)} \\ & -0.00018 * \text{Initial Gap (nm)} \\ & -1.3\text{E-}05 * \text{Voltage (V)} * \text{Initial Gap (nm)} \\ & 0.000587 * \text{Voltage (V)}^2 \\ & 2.48\text{E-}07 * \text{Initial Gap (nm)}^2 \end{aligned}$$

$$\begin{aligned} \text{Voice Coil } 1 \\ \text{Force (N)} = & 0.345891 \\ & 0.020876 * \text{Voltage (V)} \\ & -0.00067 * \text{Initial Gap (nm)} \\ & -1.3\text{E-}05 * \text{Voltage (V)} * \text{Initial Gap (nm)} \\ & 0.000587 * \text{Voltage (V)}^2 \\ & 2.48\text{E-}07 * \text{Initial Gap (nm)}^2 \end{aligned}$$

Table A.10: ANOVA for force response of small gap experiment, cont.

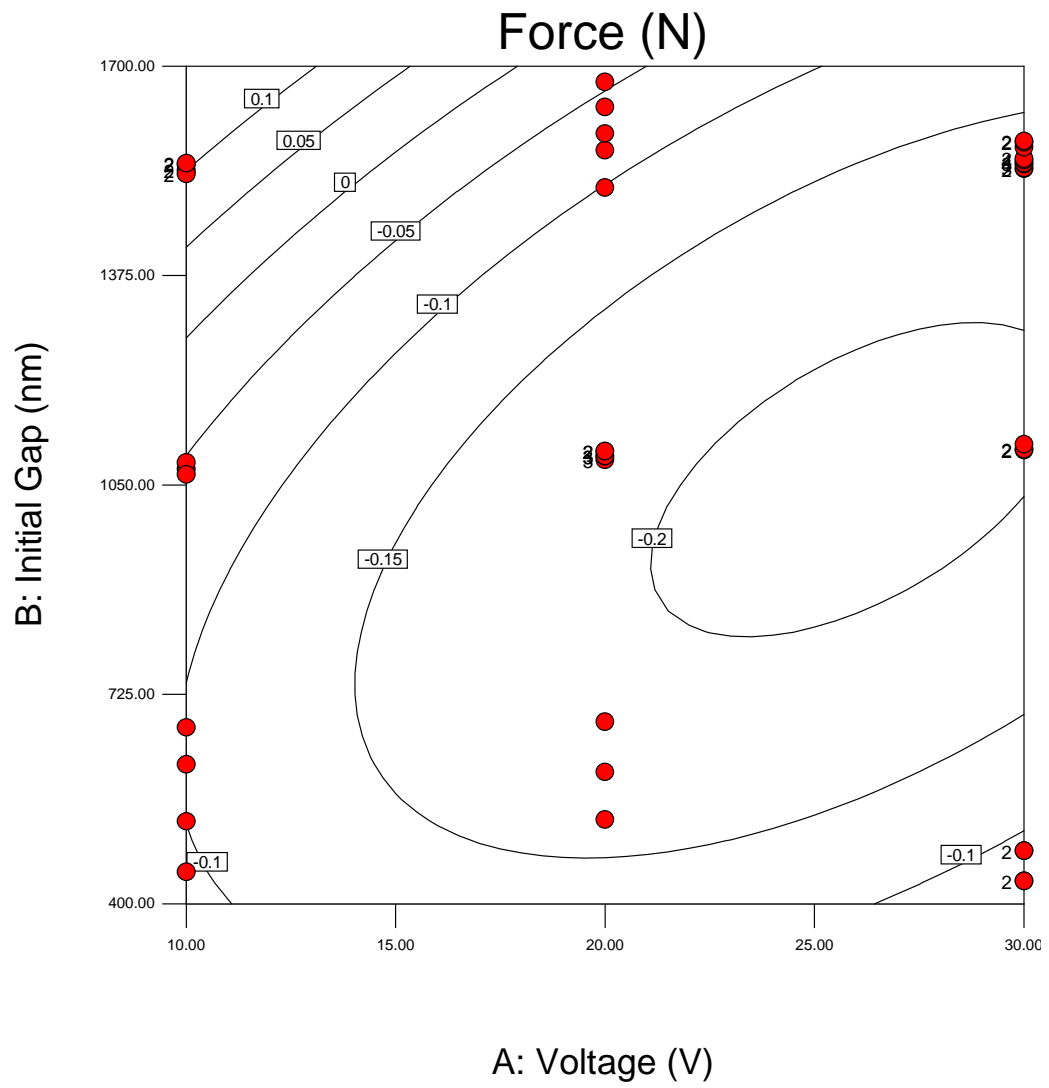


Figure A.9: Response surface for measured force without voice coil compensation, small gap experiment

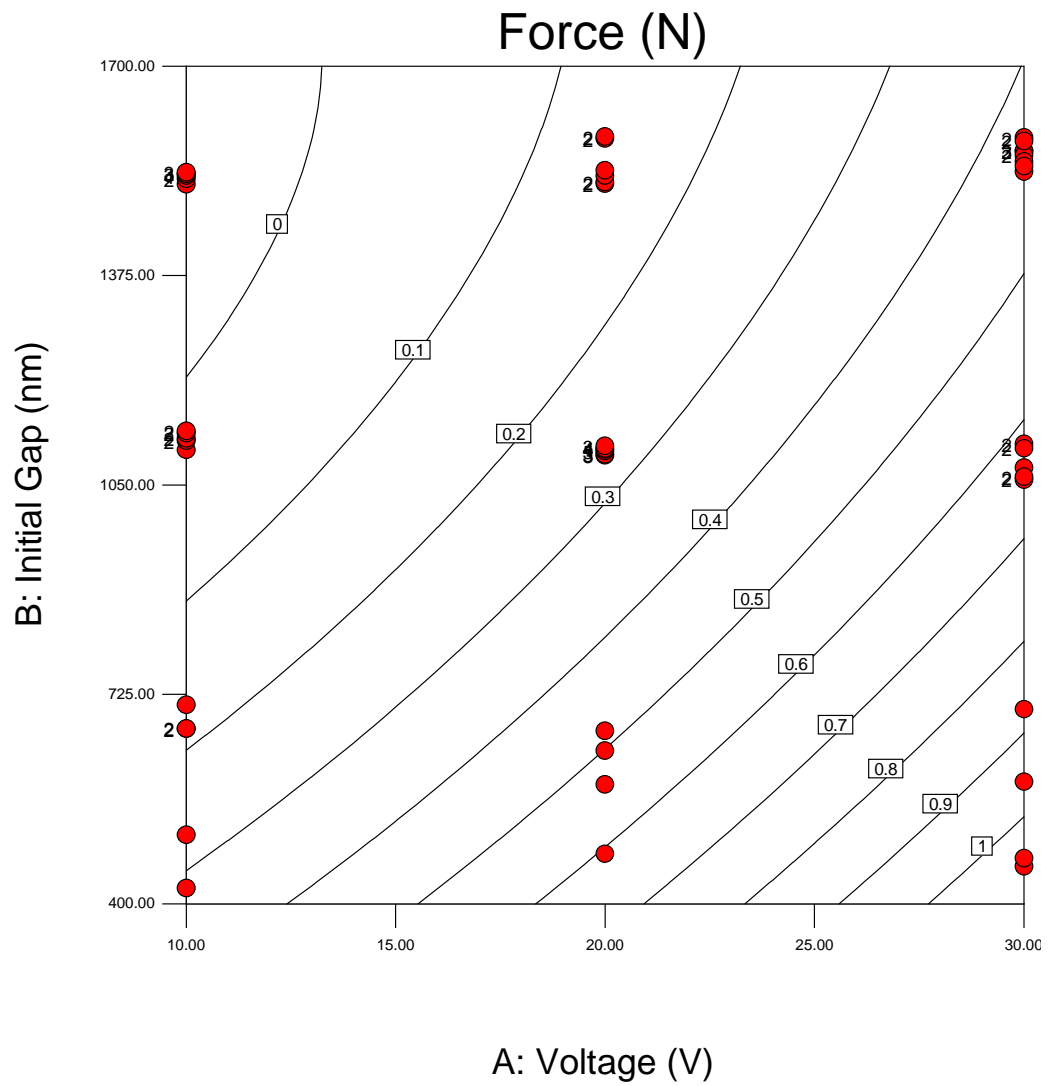


Figure A.10: Response surface for measured force with voice coil compensation, small gap experiment

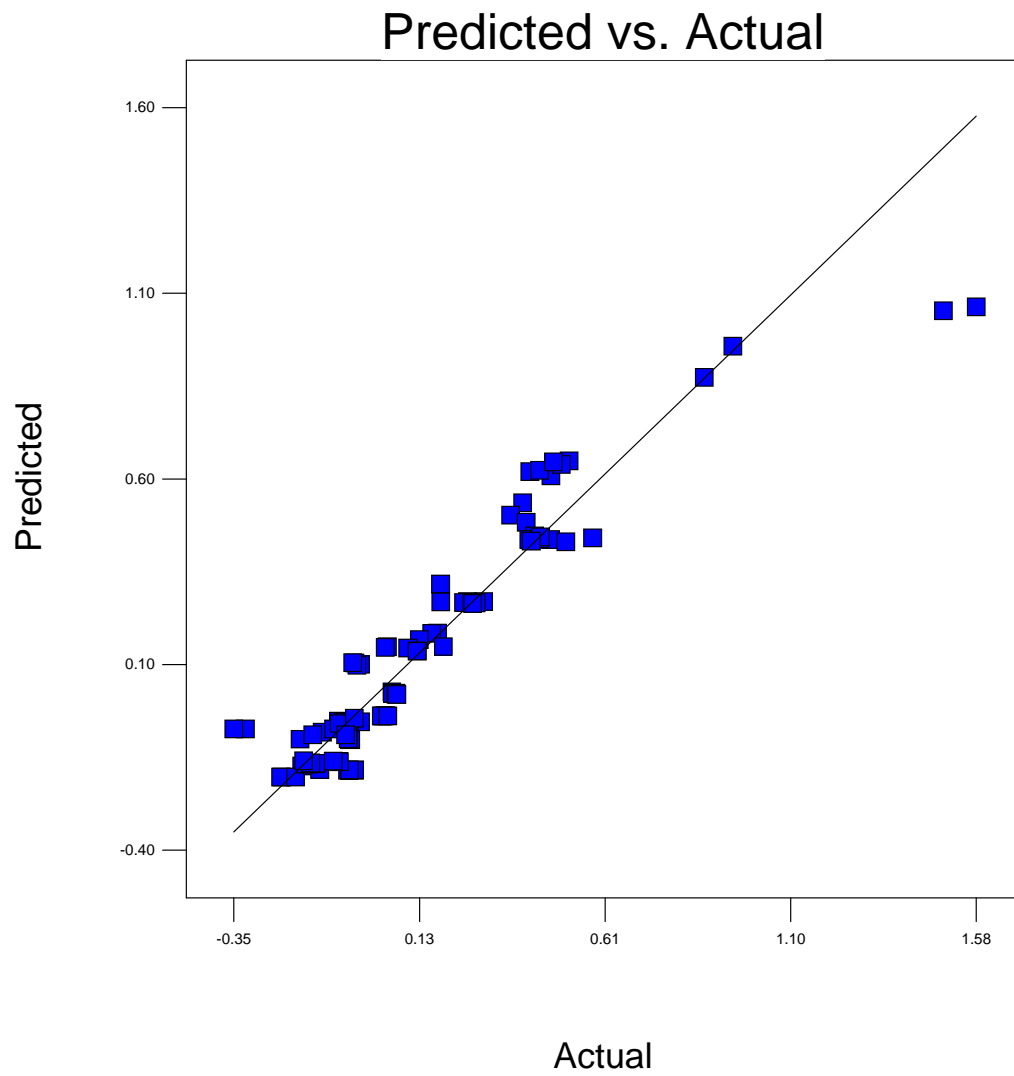


Figure A.11: Predicted versus actual values for force response, small gap experiment

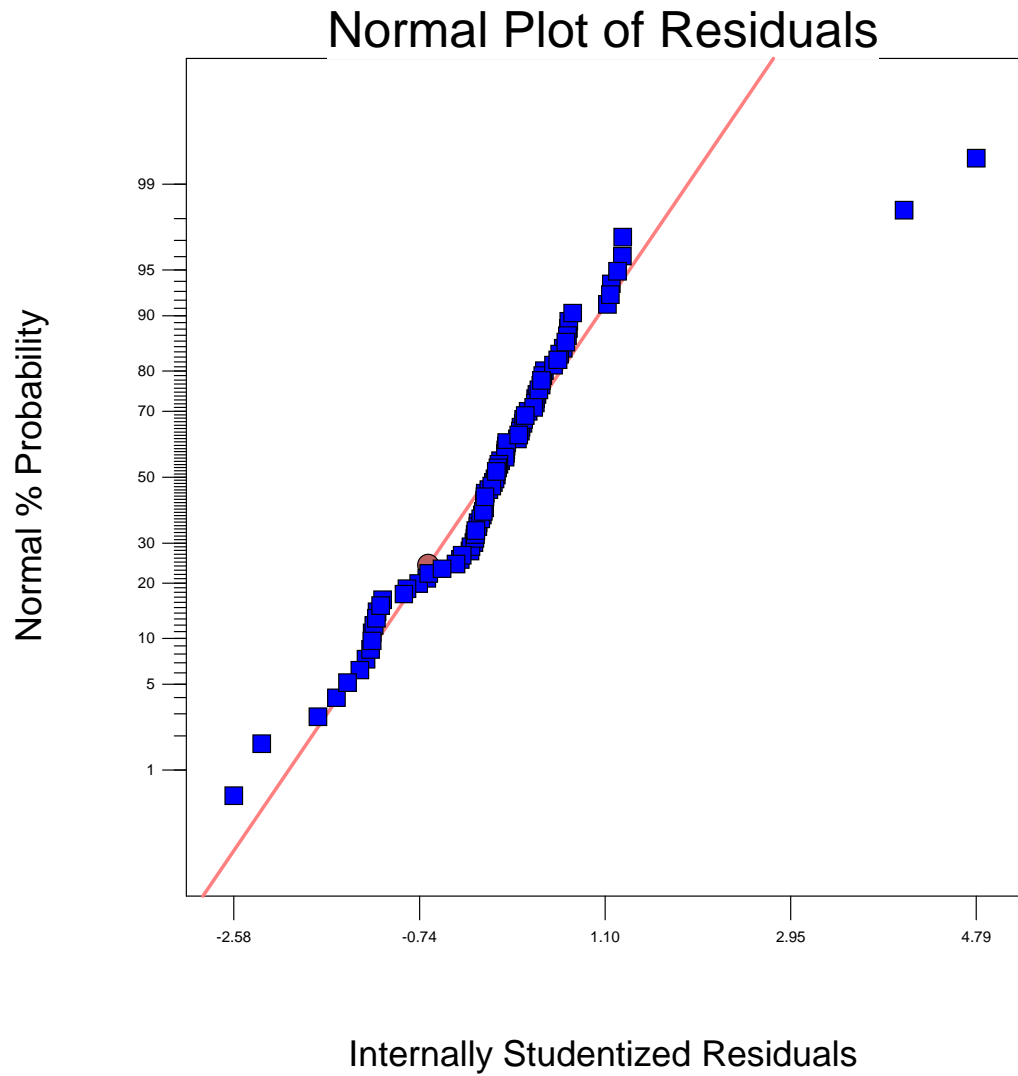


Figure A.12: Normalized residuals of force response, small gap experiment

Response 1 Gap Change (nm)					
ANOVA for Response Surface 2FI Model					
Analysis of variance table [Partial sum of squares - Type III]					
Source	Sum of Squares	df	Mean Square	F Value	p-value Prob > F
Model	7310.384	6	1218.397	33.08939	< 0.0001 significant
A-Voltage	293.847	1	293.847	7.980333	0.0060
B-Initial G	517.9501	1	517.9501	14.06656	0.0003
C-Voice Co	5113.766	1	5113.766	138.8803	< 0.0001
AB	151.3814	1	151.3814	4.111236	0.0459
AC	971.0955	1	971.0955	26.37314	< 0.0001
BC	636.5786	1	636.5786	17.28828	< 0.0001
Residual	2982.533	81	36.82139		
Lack of Fit	2981.355	79	37.73867	64.09149	0.0155 significant
Pure Error	1.17765	2	0.588825		
Cor Total	10292.92	87			

The Model F-value of 33.09 implies the model is significant. There is only a 0.01% chance that a "Model F-Value" this large could occur due to noise.

Values of "Prob > F" less than 0.0500 indicate model terms are significant. In this case A, B, C, AB, AC, BC are significant model terms. Values greater than 0.1000 indicate the model terms are not significant. If there are many insignificant model terms (not counting those required to support hierarchy), model reduction may improve your model.

The "Lack of Fit F-value" of 64.09 implies the Lack of Fit is significant. There is only a 1.55% chance that a "Lack of Fit F-value" this large could occur due to noise. Significant lack of fit is bad -- we want the model to fit.

Std. Dev.	6.068063	R-Squared	0.710234
Mean	-6.34806	Adj R-Squared	0.68877
C.V. %	95.58924	Pred R-Squared	0.661608
PRESS	3483.04	Adeq Precision	18.66157

The "Pred R-Squared" of 0.6616 is in reasonable agreement with the "Adj R-Squared" of 0.6888.

"Adeq Precision" measures the signal to noise ratio. A ratio greater than 4 is desirable. Your ratio of 18.662 indicates an adequate signal. This model can be used to navigate the design space.

Factor	Coefficient		Standard Error	95% CI		VIF
	Estimate	df		Low	High	
Intercept	-7.40403	1	0.692447	-8.78179	-6.02628	
A-Voltage (-2.36977	1	0.838872	-4.03886	-0.70068	1.116928
B-Initial Ga	3.022886	1	0.805987	1.419225	4.626547	1.041886
C-Voice Coi	8.147339	1	0.691346	6.771777	9.522901	1.132842

Table A.11: ANOVA for gap response of small gap experiment

AB	-1.93302	1	0.953347	-3.82988	-0.03616	1.137013
AC	4.129081	1	0.804031	2.529313	5.72885	1.034055
BC	-3.31443	1	0.797138	-4.90049	-1.72838	1.146941

Final Equation in Terms of Coded Factors:

$$\begin{aligned} \text{Gap Change} = & \\ & -7.40403 \\ & -2.36977 * A \\ & 3.022886 * B \\ & 8.147339 * C \\ & -1.93302 * A * B \\ & 4.129081 * A * C \\ & -3.31443 * B * C \end{aligned}$$

Final Equation in Terms of Actual Factors:

$$\begin{aligned} \text{Voice Coil } -1 \\ \text{Gap Change} = & \\ & -22.9604 \\ & -0.26328 * \text{Voltage (V)} \\ & 0.020407 * \text{Initial Gap (nm)} \\ & -0.00039 * \text{Voltage (V)} * \text{Initial Gap (nm)} \end{aligned}$$

$$\begin{aligned} \text{Voice Coil } 1 \\ \text{Gap Change} = & \\ & -9.92432 \\ & 0.562536 * \text{Voltage (V)} \\ & 0.007149 * \text{Initial Gap (nm)} \\ & -0.00039 * \text{Voltage (V)} * \text{Initial Gap (nm)} \end{aligned}$$

Table A.12: ANOVA for gap response of small gap experiment, cont.

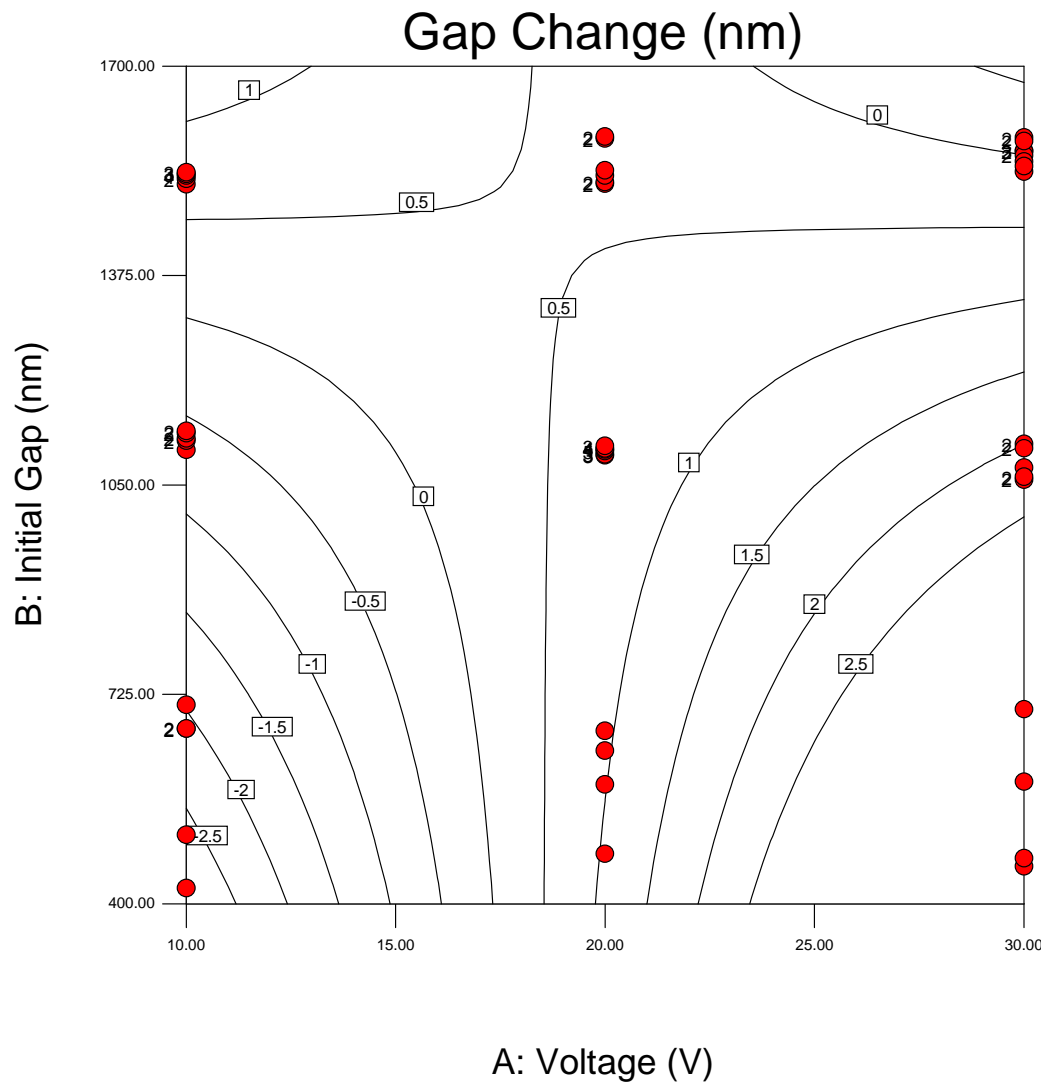


Figure A.14: Response surface for gap change with voice coil compensation, small gap experiment

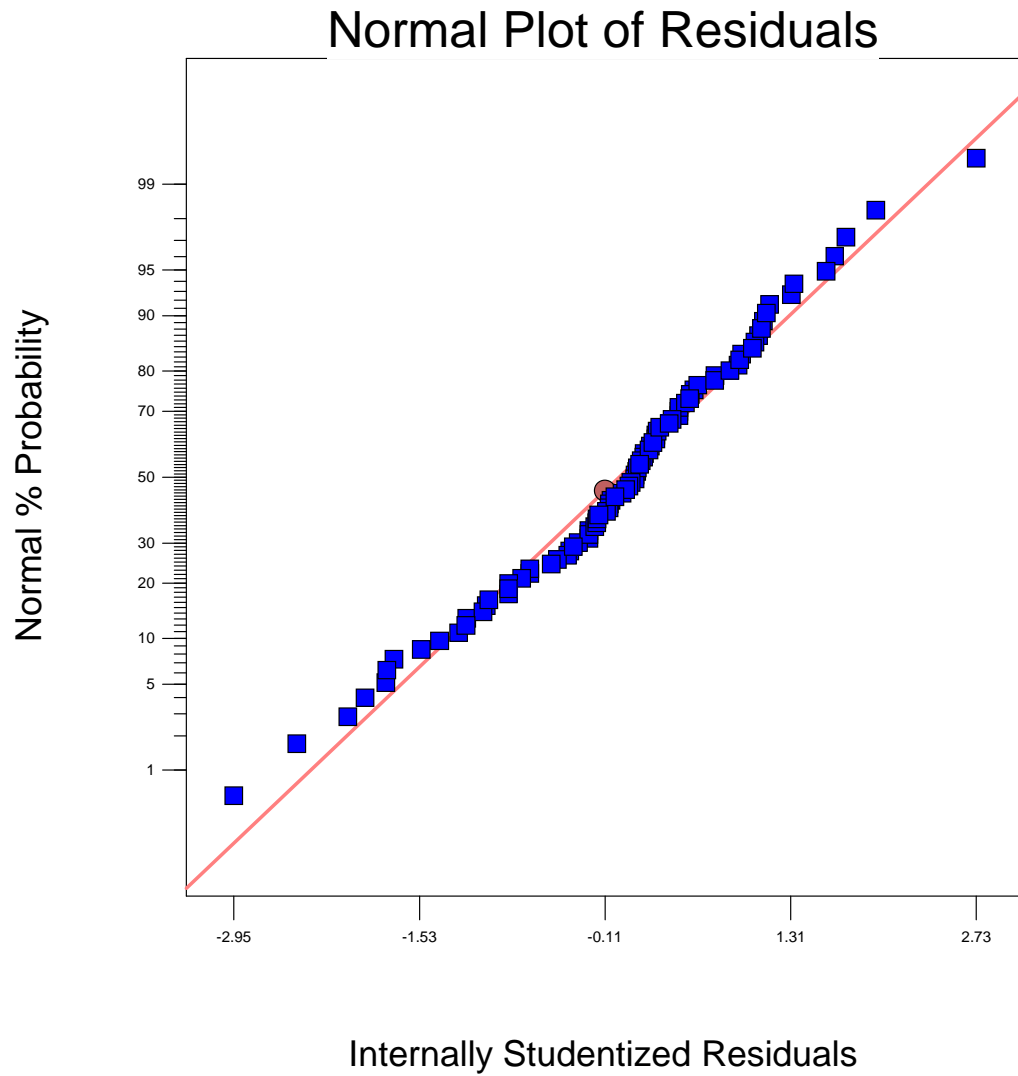


Figure A.16: Normalized residuals of gap response, small gap experiment

Voltage (V)	Initial Gap (nm)	Voice Coil (on/off)	Gap Change (nm)	Force (N)
10	449.64	-1	-15.04	-0.0506
10	527.96	-1	-25.3	-0.0537
10	616.09	-1	-22.36	-0.0473
10	673.57	-1	-16.63	-0.05035
10	1066.4	-1	-2.5	-0.067
10	1074.4	-1	-1.4	-0.022
10	1084.8	-1	-4.5	-0.0795
10	1532.36	-1	-2.95	-0.0311
10	1538.2	-1	-2.4	-0.022176
10	1547.24	-1	-9.75	-0.036139
10	1549.3	-1	-1.3	-0.041863
20	530.62	-1	-21.89	-0.0782
20	604.52	-1	-27.43	-0.1742
20	682.47	-1	-16.91	-0.128
20	1088.9	-1	-2.7	-0.0515
20	1094.4	-1	-4	-0.0379
20	1094.8	-1	-4.5	-0.0552
20	1102.2	-1	-6.4	-0.0374
20	1102.3	-1	-4.8	-0.0511
20	1511.4	-1	-8.3	-0.1785
20	1569.4	-1	-12.4	-0.1212
20	1595.3	-1	-6.9	-0.0921
20	1636.6	-1	-19.7	-0.0777
20	1675.2	-1	-6.3	-0.0377
30	435.37	-1	-24.53	-0.3211
30	435.4	-1	-23	-0.3512
30	482.3	-1	-32.3	-0.0605
30	1103.8	-1	-35.7	-0.2261
30	1105.3	-1	-32.6	-0.2294
30	1113.1	-1	-13.2	-0.1906
30	1540.4	-1	-11.1	-0.155
30	1541.4	-1	-10.6	-0.1657
30	1547.6	-1	-11.2	-0.1405
30	1549.3	-1	-10.9	-0.1367
30	1553.9	-1	-11.9	-0.1519
30	1556.5	-1	-22.1	-0.1507
30	1573.8	-1	-25	-0.077
30	1581.6	-1	-23	-0.0927
30	1583.7	-1	-20.9	-0.1696
10	424.29	1	-1.89	0.1862
10	507	1	-6.85	0.186522
10	671.48	1	0.51	0.1783
10	672	1	-0.5	0.1625
10	708.74	1	-3.8	0.131
10	1104.2	1	0.3	0.0597
10	1118.4	1	1	0.06957
10	1122	1	-2	0.060655
10	1130	1	-18	0.0706
10	1133.6	1	0.8	0.072986
10	1516.47	1	0.22	0.04419

Table A.13: Raw data from small gap experiment

10	1524.84	1	-0.65	0.038817
10	1529.94	1	16.39	0.0344
10	1532.7	1	1.4	0.0324
10	1535.11	1	0.28	0.0489
20	477.4	1	7.57	0.4729
20	585.03	1	-0.13	0.399
20	637.38	1	0.35	0.3678
20	668.26	1	2.26067	0.408209
20	1095.9	1	1.5	0.256
20	1097.3	1	0.8	0.2976
20	1102.4	1	1.2	0.2455
20	1105	1	1.1	0.2673
20	1106.2	1	2.4	0.2786
20	1110.5	1	1.6	0.2696
20	1517.3	1	-4.6	0.1935
20	1520	1	-0.6	0.0475
20	1530	1	-0.6	0.0425
20	1538.4	1	0.7	0.1007
20	1587.5	1	-1.7	0.1257
20	1590.6	1	1.9	0.1252
30	701.84	1	3.61	0.8708
30	1058.2	1	1.3	0.5195
30	1062.7	1	-8.3	0.4791
30	1076.7	1	-8.4	0.4995
30	1106.7	1	-3	0.4431
30	1113.5	1	-1.1	0.4183
30	1536.3	1	3.6	0.4306
30	1544.7	1	3.2	0.4457
30	1552	1	-6.8	0.5812
30	1561.4	1	4.9	0.4424
30	1568	1	2.9	0.4157
30	1568.5	1	4.2	0.4715
30	1583.3	1	2.1	0.4217
30	1589.1	1	2.2	0.5116
30	589.39	1	6.07	0.945331
30	458	1	10	1.5773
30	470.5	1	10.5	1.4922
30	482.29	-1	-32.18	-0.146

Table A.14: Raw data from small gap experiment, cont.

Bibliography

- [1] (2004, Jan.) International technology roadmap for semiconductors. [Online]. Available: [HTTP://public.itrs.net](http://public.itrs.net)
- [2] C. A. Mack, “The end of the semiconductor industry as we know it,” in *Emerging Lithographic Technologies VII, Proceedings of SPIE*, vol. 5037, 2003, pp. 1–11.
- [3] G. E. Moore, “Cramming more components onto integrated circuits,” *Electronics*, vol. 38, no. 8, pp. 114–117, Apr. 1965.
- [4] M. Switkes, M. Rothschild, R. Kunz, S.-Y. Baek, D. Cole, and M. Yeung, “Immersion lithography: Beyond the 65nm node with optics,” *Microlithography World*, pp. 4–7, May 2003.
- [5] C. A. Mack, “Resolution enhancement technologies,” *Microlithography World*, pp. 14–16, May 2003.
- [6] L. Choo, O. Park, M. Sack, and S. Tam, “Integration of attenuated phase shift mask to 0.13 μ m technology contact level masking process,” in *Optical Microlithography XIII, Proceedings of SPIE*, vol. 4000, 2000, pp. 1193–1202.

- [7] M. Mukherjee, Z. Baum, J. Nickel, and T. Dunham, “Optical rule checking for proximity corrected mask shapes,” in *Optical Microlithography XVI, Proceedings of SPIE*, vol. 5040, 2003, pp. 365–375.
- [8] L. S. Melvin, III, J. P. Shiely, M. L. Rieger, and B. Painter, “A methodology to calculate line-end correction feature performance as a function of reticle cost,” in *Optical Microlithography XVI, Proceedings of SPIE*, vol. 5040, 2003, pp. 386–394.
- [9] G. S. Chua, Q. Lin, C. J. Tay, and C. Quan, “Sub-0.10 μ m lithography technology with resolution enhancing technique,” in *Optical Microlithography XV, Proceedings of SPIE*, vol. 4691, 2002, pp. 1563–1574.
- [10] S. Owa and H. Nagasaka, “Immersion lithography; its potential performance and issues,” in *Optical Microlithography XVI, Proceedings of SPIE*, vol. 5040, 2003, pp. 724–733.
- [11] U. Behringer, “1x stencil masks fabrication and their use in low energy electron beam proximity lithography (leapl),” in *Proceedings of SPIE: 24th Annual BACUS Symposium on Photomask Technology*, vol. 5567, 2004, pp. 864–875.
- [12] N. Nakajima, T. Atarashi, H. Sakai, T. Fukui, and H. Takano, “Leapl (low energy electron beam proximity-projection lithography) over-lay status,” in *Proceedings of the SPIE: Emerging Lithographic Technologies VIII*, vol. 5374, 2004, pp. 529–536.

- [13] S. Omori, S. Nohdo, S. Nohama, K. Nakayama, K. Iwase, T. Motohashi, K. Amai, Y. Watanabe, K. Inoue, I. Ashida, H. Ohnuma, H. Nakano, S. Moriya, and T. Kitagawa, “Progress in proximity electron lithography: demonstration of print and overlay performance using the low-energy electron beam proximity-projection lithography β tool,” *Journal of Microlithography, Microfabrication, and Microsystems*, vol. 3, no. 3, pp. 404–412, 2004.
- [14] U. Palun, S. Tedesco, M. Heitzman, F. Martin, D. Frabouleta, B. Dal’zottoa, M. Nier, P. Mur, T. Charvolin, D. Mariolle, and F. Tardif, “Fabrication of single electron devices by hybrid (e-beam/duv) lithography,” *Micro-electronic Engineering*, vol. 53, pp. 167–170, 2000.
- [15] Y. Xia and G. Whitesides, “Soft lithography,” *Angewandte Chemie International Edition in English*, vol. 37, p. 550, 1998.
- [16] S. Chou, P. R. Knauss, and P. J. Renstrom, “Nanoimprint lithography,” *Journal of Vacuum Science and Technology B*, vol. 14, no. 6, p. 4129, 1996.
- [17] M. Colburn, M. S. S. Johnson and, S. Damle, T. Bailey, B. Choi, M. Wedlake, T. Michaelson, S. Sreenivasan, J. Ekerdt, and C. Willson, “Step and flash imprint lithography: A new approach to high-resolution patterning,” in *Proceedings of the SPIE’s 24th International Symposium on Microlithography: Emerging Lithographic Technologies III*, vol. 3676, 1999, pp. 379–389.

- [18] B. J. Choi, S. Johnson, S. Sreenivasan, and C. Willson, “Design of alignment stages for step & flash imprint lithography,” in *Proceedings of the Annual Meeting of the American Society of Precision Engineers*, 1999.
- [19] M. Melliar-Smith, “Lithography beyond 32nm: A role for imprint?” in *PROCEEDINGS OF SPIE: Emerging Lithographic Technologies XI*, vol. 6517, 2007, pp. xxi–xxxiv.
- [20] S. Y. Chou and L. Zhuang, “Lithographically induced self-assembly of periodic polymer micropillar arrays,” *Journal of Vacuum Science and Technology B.*, pp. 3197–3202, Nov. 1999.
- [21] E. Schäffer, T. Thurn-Albrecht, T. Russell, and U. Steiner, “Electrically induced structure formation and pattern transfer,” *Nature*, vol. 403, pp. 874–877, Feb. 2000.
- [22] Z. Lin, T. Kerle, T. P. Russell, Schaäffer, and U. Steiner, “Structure formation at the interface of liquid/liquid bilayer in electric field,” *Macromolecules*, vol. 35, pp. 3971–3976, 2002.
- [23] E. Schäffer, T. Thurn-Albrecht, T. Russell, and U. Steiner, “Electrohydrodynamic instabilities in polymer films,” *Europhysics Letters*, vol. 53, no. 4, pp. 518–524, Feb. 2001.
- [24] L. F. Pease and W. B. Russel, “Electrostatically induced submicron patterning of thin perfect and leaky dielectric films: A generalized linear

- stability analysis,” *Journal of Chemical Physics*, vol. 118, no. 8, pp. 3790–3803, Feb. 2003.
- [25] D. Stewart, “A platform with six degrees of freedom,” *UK Institution of Mechanical Engineers Proceedings*, vol. 180, no. 15, pp. 371–386, 1965.
- [26] J. A. Carretero, R. P. Podhorodeski, M. A. Nahon, and C. M. Gosselin, “Kinematic analysis and optimization of a new three degree of freedom spatial parallel manipulator,” *Journal of Mechanical Design*, vol. 122, pp. 17–24, Mar. 2000.
- [27] V. Gough, “Contribution to discussion of papers on research in automobile stability, control and tyre performance,” *Proceedings of the Automotive Division of the Institution of Mechanical Engineers*, pp. 392–394, 1956–57.
- [28] Wikipedia. [Online]. Available: en.wikipedia.org/stewart_platform
- [29] A. Q. Nguyen, “Asymmetric fluid-structure dynamics in nanoscale imprint lithography,” Master’s thesis, The University of Texas at Austin, 2001.
- [30] D. Daney and I. Z. Emiris, “Robust parallel robot calibration with partial information,” in *IEEE International Conference on Robotics and Automation*, 2001, pp. 3262–3267.
- [31] K.-M. Lee and S. Arjunan, “A three-degree-of-freedom micromotion in-parallel actuated manipulator,” *IEEE Transactions on Robotics and Automation*, vol. 7, no. 5, pp. 634–641, Oct. 1991.

- [32] K.-M. Lee and D. K. Shah, “Kinematic analysis of a three-degree-of-freedom in-parallel actuated manipulator,” *IEEE Journal of Robotics and Automation*, vol. 4, no. 3, pp. 354–360, June 1988.
- [33] —, “Dynamic analysis of a three-degree-of-freedom in-parallel actuated manipulator,” *IEEE Journal of Robotics and Automation*, vol. 4, no. 3, pp. 360–367, June 1988.
- [34] K.-M. Lee and S. Arjunan, “A three-degree-of-freedom micro-motion in-parallel actuated manipulator,” in *IEEE Intl. Conference on Robotics and Automation*, 1989, pp. 1698–1703.
- [35] A. Sokolov and P. Xirouchakis, “Kinematics of a 3-dof parallel manipulator with an r-p-s joint structure,” *Robotica*, vol. 23, pp. 207–217, 2005.
- [36] Z. Huang and J. Wang, “Identification of principal screws of 3-dof parallel manipulators by quadric degeneration,” *Mechanism and Machine Theory*, vol. 36, pp. 893–911, 2001.
- [37] Z. Huang, J. Wang, and Y. Fang, “Analysis of instantaneous motions of deficient-rank 3-rpd parallel manipulators,” *Mechanism and Machine Theory*, vol. 37, pp. 229–240, 2002.
- [38] H. Pendar, M. Vakil, and H. Zohoor, “Efficient dynamic equations of 3-rps parallel mechanism through lagrange method,” in *IEEE International Conference on Robotics, Automation, and Mechatronics*, 2004, pp. 1152–1157.

- [39] N. Wu, I. Leonard Pease, and W. B. Russel, "Toward large scale alignment of electrodynamic patterning of thin polymer films," *Advanced Functional Materials*, vol. 16, pp. 1992–1999, 2006.
- [40] M. Dickey, "Step and flash imprint lithography: A low-pressure, room-temperature nanoimprint lithography," Ph.D. dissertation, The University of Texas at Austin, 2006.
- [41] M. Colburn, "Step and flash imprint lithography: A low-pressure, room-temperature nanoimprint lithography," Ph.D. dissertation, The University of Texas at Austin, 2001.
- [42] Capacitive sensor operation and optimization (how capacitive sensors work and how to use them effectively). [Online]. Available: <http://www.lionprecision.com/tech-library/technotes/cap-0020-sensor-theory.html>
- [43] E. Hecht, *Optics*, 4th ed. Addison Wesley, 2002.
- [44] R. J. Thornhill and C. C. Smith, *Fourier, Spectral, and Wavelet Analysis in Dynamic Systems*, 1994.
- [45] B. M. Sadler and S. D. Casey, "Frequency estimation via sparse zero crossings," in *ICASSP, IEEE International Conference on Acoustics, Speech and Signal Processing - Proceedings*, vol. 5, 1996, pp. 2990–2993.
- [46] B. G. Quinn and E. J. Hannan, *The Estimation and Tracking of Frequency*. Cambridge University Press, 2001.

- [47] T.-H. Li and K.-S. Song, “Asymptotic analysis of a fast algorithm for efficient multiple frequency estimation,” *IEEE Transactions on Information Theory*, vol. 48, pp. 2709–2720, Oct. 2002.
- [48] *US Guide to the Expression of Uncertainty in Measurement, ANSI/NSCL Standard Z540-2-1997*. NSCL International, 1997.
- [49] [Online]. Available: www.madcitylabs.com
- [50] J. B. Calvert. Capacitors. [Online]. Available: <http://www.du.edu/~jcalvert/phys/caps.htm>
- [51] J.M.Paros and L. Weisbord, “How to design flexure hinges,” *Machine Design*, pp. 151–156, Nov. 1965.
- [52] [Online]. Available: www.statease.com

Vita

Allen Lee Raines was born in Provo, Utah on November 4, 1973, the son of Dr. James A. and Vicky Raines. He grew up and attended school in Conroe, Texas. He began undergraduate work in 1992 at Brigham Young University. From May 1993-1995, he served a mission for The Church of Jesus Christ of Latter Day Saints in Denmark. Following his misison, he returned to Brigham Young University and received the Bachelor of Science degree in Mechanical Engineering in April 1998. He received his Master of Science in Mechanical Engineering from Brigham Young University in December 2000 and proceeded to doctoral studies at the University of Texas. He completed his Ph.D. in mechanical engineering in December of 2007.

Permanent address: 609 Orangewood
Conroe, Texas 77302

This dissertation was typeset with L^AT_EX[†] by the author.

[†]L^AT_EX is a document preparation system developed by Leslie Lamport as a special version of Donald Knuth's T_EX Program.